OPEN ACCESS
IOP Publishing
Journal of Physics D: Applied Physics
J. Phys. D: Appl. Phys. **53** (2020) 443002 (41pp)
https://doi.org/10.1088/1361-6463/ab96e9

Topical Review

Plasmonic resonators: fundamental properties and applications

Manuel R Gonçalves[1], Hayk Minassian[2] and Armen Melikyan[3]

[1] Ulm University—Institute of Experimental Physics, Albert-Einstein-Allee 11, 89069 Ulm, Germany
[2] A. Alikhanian National Science Laboratory (Yerevan Physics Institute), 2 Alikhanian Br. Street, Yerevan, 0036 Armenia
[3] Russian-Armenian University, 123 Hovsep Emin Str., Yerevan, 0051 Armenia

E-mail: manuel.goncalves@uni-ulm.de

Received 20 December 2019, revised 21 April 2020
Accepted for publication 27 May 2020
Published 6 August 2020

Abstract

Resonators of surface plasmons are discussed in this review. Any material supporting the excitation of surface plasmons, either by light, or by electron beams can be used for designing a resonator. Despite the number of materials supporting surface plasmons being restricted to a small number, noble metals, some two-dimensional materials as graphene, transition metal oxides, and several highly doped semiconductors have been used in plasmonic applications. Isolated and coupled metal nanoparticles, arrays of particles on substrates, nanoparticle suspensions, alternated metal and dielectric thin films, dielectric cavities in surfaces of noble metals and sheets and stripes of two-dimensional materials are typical examples of systems used for excitation of plasmonic resonances. These resonances have been used in a fast increasing number of applications: transformation of light beam properties, selective optical induced heating, sensing of chemical or biological compounds, enhancement of non-linear optical excitation in nanomaterials, optical coherence applications in quantum optics. The operating spectral range, variety of sizes, shapes and geometrical configurations that can be tailored and the exceptional optical properties of surface plasmons promote their use in a wide variety of applications at the nanoscale, where other types of resonators cannot be used, or are too inefficient.

We review a large variety of plasmonic resonators and their most relevant properties. We first discuss the fundamental properties of the plasmonic resonances, using simple physical models. Then we present a retrospective of applications evidencing the most relevant aspects of interaction of surface plasmons with matter and radiation. Finally we focus the most recent applications covering metamaterials, plasmonic materials with topological properties and resonators supporting plasmon-electron interaction.

Keywords: surface plasmons, Fano resonance, Purcell effect, optical nanoantenna, strong coupling, hyperbolic metamaterial, topological insulator

(Some figures may appear in colour only in the online journal)

1. Introduction

Electronic charge-density oscillations coupled with retarded electromagnetic field modes in metal surfaces are called surface plasmon-polaritons. They constitute a fundamental type of electromagnetic oscillation at the nanoscale with major impact in several fields of modern physics. These oscillations can be excited in all materials presenting negative real part of the dielectric function in a broad band of the electromagnetic spectrum, when interfacing with a dielectric medium. Surface plasmons can be excited in structures with a geometry of 1D, 2D, and 3D space dimensions. These structures are generally called plasmonic resonators. The dimensionality, size and morphology determine the kind of resonances that can be produced for a certain material, or combination of materials.

Key features of the surface plasmons are their excitation by electromagnetic waves, either propagating or evanescent, electron beams, and by electric polarisation in nanoscale junctions. However, propagating waves and electron beams require a phase matching condition to be verified. By other side, the extreme surface confinement of the surface plasmons is associated with an exponential decay with the distance of the near-fields [1].

Surface plasmons are distinct from other quasi-particle oscillations as bulk plasmons, phonons, magnons and excitons, as they are excited at the surface of metals. The wide range of resonators that can be conceived always relies on the strong confinement of the electromagnetic field, on the energy of the optical resonance and on the resulting scattering angular spectrum. The confinement of plasmons has other relevant implications, namely in the geometrical properties of several light quantities as spin, linear and angular momentum of near-fields, quite different than those of propagating fields.

Resonances on individual or coupled particles can be analysed using the equations of motion of classical mechanical or electrical resonators. Although this seems to be an oversimplification it provides a good qualitative and in some cases quantitative description of the interaction. However, a rigorous description of the far- and near-fields and derived quantities requires solving the Maxwell's equations. Almost all physical quantities related to plasmonic resonators can be described in the framework of classical or semi-classical physics. Only for very small particles, thin junctions and some matter-radiation interaction cases full quantum mechanical treatment is required.

Current investigations of plasmonic resonators do not focus only on the interaction between electromagnetic radiation, or electrons and plasmons, but make use of the already well known resonators to explore other physical effects as topological properties of materials, quantum states of light, metamaterials and transport phenomena.

In this review, after this introduction and a short historical note, we firstly give an overview of the fundamental properties of simple and coupled plasmonic resonators, describing their resonance properties using classical oscillators models. In some cases we compare the properties with the results obtained from rigorous calculations of the Maxwell's equations. We continue with a survey of already well known applications of plasmonic resonators in several levels of matter-radiation interaction, both classical and quantum. Simultaneouly we briefly discuss recent advances related to these applications. We finish with a bunch of the most recent research progresses relying on plasmonic resonators, including topological materials, metamaterials, and the revival of electron-plasmon interaction.

2. Historical note on plasmonic resonators

The discovery of surface waves called surface plasmon polaritons (SPP), is due to Ritchie [2]. SPPs are responsible for the angular dependent losses of fast electron beams crossing thin metal sheets. These surface excitations of the conduction electrons have lower energy than the bulk plasmons of the metal. Later, it was found that light could also excite surface plasmons, provided the phase matching condition between the wave vector of the incoming light and wave vector of the surface plasmon would be achieved [3, 4]. It became then possible to relate the surface plasmons with the Mie resonances of metal colloids, well known since the beginning of the 20th century [5], but already experimentally investigated by Faraday [6]. These resonant modes arise by spatial confinement of the surface plasmons at the surface of a noble metal sphere, unlike the propagating modes in infinitely extended metal-dielectric interface.

Despite the fact that plasmons have been treated as an example of excitons of solid state physics, the progress of research on all phenomena related to surface plasmons, globally called plasmonics, evolved autonomously, often approaching classical optics and electrical engineering rather than other branches of solid state physics. This was mainly due to the fact that the number of materials suitable for plasmonic applications remained very small and new materials are difficult to engineer. Surface plasmons require materials with free electrons and low optical losses at the optical bandwidth, which restricts us to a few available in nature including gold, silver, and aluminium [7–10]. An easy way to check if a material has potential to be used in plasmonics is by analysing its dielectric function. Good plasmonic materials in the visible and near-IR must have a negative real part of the dielectric function and simultaneously a small imaginary part. More recently, other materials synthesised by different techniques extended the number of materials presenting plasmonic properties. This includes 2D materials as graphene, molybdenum disulphide, the so called MXenes [11], compound 3D materials as metal nitrides, highly doped semiconductors and transparent conducting oxides [12, 13]. Limitation are the spectral region where these materials present adequate values of the dielectric function, which is mostly in mid-IR to far-IR and optical losses. However, in 2D materials as graphene surface plasmons are tunable.

As surface plasmons are electromagnetic surface waves, we can consider several ways to propagate and confine them. The most elementary geometrical structure, beyond the trivial metal-dielectric interface, supporting surface plasmon modes is the thin metal film surrounded by two dielectric

semi-infinite media. This is usually called DMD (dielectric-metal-dielectric), also called IMI (insulator-metal-insulator) structure. Its counterpart forming a planar gap between semi-infinite metal regions is the MDM, or MIM. The properties of the plasmonic modes supported by these structures were extensively investigated elsewhere [14–18]. Planar structures supporting plasmon guided modes were among the first noble metal structures investigated. However, it became evident that surface corrugations, grooves and other geometrical shapes on a planar film would modify the propagation and confinement of surface plasmons, leading to localised resonances and modifying the dispersion relation [17, 19–21]. The first observation of an effect arising by plasmon confinement in metal gratings was reported by Wood in 1902, the so called Wood's anomaly [22]. Despite successive approaches, the first theoretical models provided only phenomenological explanations [23–25]. The nature of the surface waves leading to the Wood's anomaly remained not well understood. The discovery of the surface plasmons furnished the physical basis for a consistent explanation of the spectral anomaly observed.

In 1998, Ebbesen and collaborators found an intriguing large value of the zero-order optical transmission of white light through an array of sub-wavelength holes drilled on a silver film of 0.2 μm thickness [26]. The transmission was only remarkable for some spectral bands and not in the full visible spectrum. The transmission was considered extraordinary by comparing its maxima with the prediction of the Bethe theory of diffraction for a single sub-wavelength aperture on a perfectly absorbing screen [27]. The transmission value was also highly dependent on the angle of incidence. A satisfactory explanation was given in terms of the coupling of light with the plasmonic modes excited at the surface of the hole array. By other side, it was already known that 2D gratings on silver could present bandgaps [28]. This coupling between surface modes was already analysed by Fano in 1938, to explain the Wood's anomalies in 1D gratings [24]. Interestingly, Fano obtained a similar mathematical expression to describe the asymmetrical lineshapes arising in the ionisation spectra of noble gases, in the context of atom physics [29–31]. Since then these quite universal resonances are called Fano resonances.

Curved surfaces, or corrugations in metallic films where surface plasmons propagate, lead to reflections and eventually to localised plasmon modes. The curvature of the surface leading to reflections can be understood as a geometrical potential [32, 33]. In metal films structured with deep grooves plasmons can easily couple to external light, unlike thin flats films. Deep grooves strongly confine plasmons and simultaneously produce narrow absorption resonances. Because of that, grooves of different shapes have been fabricated to produce structural colours [34–36].

Other way to increase the number of surface plasmon modes propagating along the metal-dielectric interfaces is by stacking alternating layers metal and dielectric media. The mode dispersion arising in such stacks was already investigated by Economou in 1969 [14]. In the last two decades, these stacks regained attention due to the discovery of the hyperbolic metamaterials [37–39]. The plasmonic modes become guided in volume of the stack. Some of the guided modes can have very large wavenumbers, which is required in sub-wavelength imaging. The stack itself does not form a cavity in the strict sense, but as some modes may have very large wavenumbers allows for radiative decay engineering [40–43].

Although the work of Mie established a milestone in the history of electromagnetics of metal colloidal particles, Mie resonances remained long time disconnected from other effects due to the excitation of surface plasmons. The intensive calculations required to solve the Maxwell's equations of arbitrary geometry and complex dielectric function only become possible with the advent of computational electromagnetics, after the 1960s. By the other side, a large amount of theoretical calculations based on approximations of the classical electromagnetic theory, over the full past century, permitted to achieve an increasingly detailed knowledge of the properties of small metal particles of various shapes, arrangements, and environments [44–48]. In the last decades new techniques of nanoscale fabrication [49–52], experimental and theoretical investigation of the optical properties of nanoparticles [47, 53, 54], and new microscopy and spectroscopy techniques [55–60] boosted a fast development of plasmonics extending the applications range.

The interaction of plasmonic nanostructures with matter in their immediate neighbourhood has been a subject of increasing attention, both in the classical and the quantum world. The incomparable near-field enhancement and confinement provides the basis for a large number of applications. Fundamentally, the plasmonic structure acts as a resonator with optical response in the near- and far-field. For a specific nanoparticle, the optical response of the resonator is mainly determined by the wavelength and polarisation state of the illuminating light. The near-field distribution of particles arranged in close proximity is also strongly modified, due to near-field coupling. The propagating far-fields present radiation patterns that depend on the polarisation direction and plasmonic mode excited. Particles of the size of the wavelength and larger have radiation patterns not only dependent on the polarisation direction of the incoming field but also on the number of multipoles excited. Single nanoparticles, or arrays of coupled nanoparticles can operate as optical antennas. On the other hand, when the excitation is done by an electron beam in vacuum, the polarisation state is not defined, but the point at which the electrons hit the metal determines the near-field pattern and the angular spectrum of radiation emitted. In most of applications light is used for the excitation of surface plasmons and many modern applications rely on hierarchical arrangements of optical nanoantennas.

Before we discuss applications of plasmonic resonators and the underlying morphology and materials, it is convenient to describe the fundamental characteristics of the plasmonic resonances using classical oscillators, as they furnish the basic elements to understand the physical mechanisms of the resonances.

3. General properties of plasmonic resonances

In this section the origin of plasmonic resonances is reviewed. Firstly, we address briefly the dielectric function of plasmonic

materials. Then, we present a phenomenological treatment of plasmonic resonances in isolated and coupled systems of particles, as they form the basis for many effects based on plasmonic excitation. We give examples for the most relevant resonant effects.

3.1. Dielectric function of plasmonic materials

Plasmons are low energy excitations in an electron gas. In metallic solids where electrons are free and can be easily driven by external electric fields, oscillations of charge density arise due to the application of the external field and the restoring force of the positively charged material remaining. In a periodic potential the model describing the dynamics of electrons determines the effective mass m^*, which depends on the band structure of the materials and is different than the mass of a free electron. The bulk plasma frequency is determined by the mean density of electrons n_e, related to the Fermi energy of the material, and its effective mass. It reads $\omega_p = (4\pi e^2 n_e/m^*)^{1/2}$ in cgs units, or $\omega_p = [e^2 n_e/(\epsilon_0 m^*)]^{1/2}$ in SI units. This quantity is obtained from the equation of motion of an infinitesimal volume of electrons under an external electric field. Plasma frequencies range from 15 eV for aluminium down to THz frequencies for graphene.

The dielectric function of bulk plasmonic materials as noble metals according to the Drude–Sommerfeld electron model is given by

$$\epsilon(\omega) = \epsilon_1 + i\epsilon_2 = \epsilon_\infty - \frac{\omega_p^2}{\omega^2 + i\omega\gamma}. \tag{1}$$

$\epsilon_\infty \geq 1$ accounts for the contribution of the positive ionic cores to the dielectric function. For a perfect electron gas it takes the value of 1. The refractive index is also a complex quantity and related to the dielectric function by $\tilde{n} = n + ik = \sqrt{\epsilon}$. The Drude–Sommerfeld model cannot describe the band structure of the metal and therefore, in calculations is often substituted by the experimental values of the dielectric function or refractive index [7]. More accurate models of the dielectric function include non-local response, which is dependent on the particle size, and other parameters [61–63].

Graphene is a 2D material with a more complicated optical response [64–70]. The optical conductivity of graphene is described by $\sigma = \sigma_\mathrm{I} + \sigma_\mathrm{D}$. The first term is a interband contribution expressed by $\sigma_\mathrm{I} = \sigma' + i\sigma''$. The second is the Drude contribution, which dominates for heavily doped graphene and frequencies much below the Fermi level E_F. Graphene is one of the most investigated materials today and new properties and applications in many fields beyond plasmonics have appeared.

In contrast to Drude metals graphene presents an extraordinary advantage: the optical response can be tuned by a chemical potential, or by applying an external voltage. The electrical tunability is not an exclusive property of graphene, in contrast with other bulk plasmonic materials, characterised by the Drude–Sommerfeld model. The dielectric properties of other 2D materials as the monolayered transition metal dichalcogenides (MoS2, WS2, WSe2) can also be tuned [71]. Graphene plasmons present as well very large wavenumbers and exhibit the strongest field confinement of any surface plasmons [68, 72]. The only limitation is the frequency band where the tunability and field confinement are so large: the mid-IR to THz frequency range [73]. At visible wavelengths the optical absorption reaches 2.3%.

The search for better plasmonic materials in several directions as, lower loss, application at high temperature, wide bandwidth, tunability, low chemical reactivity, transparency, non-linear response and near-zero refractive index has been subject of intensive research and has been already addressed in many research articles and reviews [12, 13, 74–79].

3.2. The driven damped oscillator and the plasmonic particle

The optical response of an isolated plasmonic particle where a plasmon is excited can be characterised by the phenomenological model of a driven damped oscillator. The spectrum of the harmonic oscillator with low damping ($2\omega_0 \gg \gamma$) is approximated by the Lorentzian lineshape [80]. We summarise the properties of such oscillator in order to analyse afterwards several examples of coupling between oscillators. The equation of motion of the harmonic damped oscillator of charge q and mass m, driven by an external harmonic force $f(t) = f_0 \exp(i\omega t)$, is given by

$$m\ddot{x} + m\gamma\dot{x} + m\omega_0^2 x = f_0 \exp(i\omega t). \tag{2}$$

We can normalise by the mass and obtain

$$\ddot{x} + \gamma\dot{x} + \omega_0^2 x = a_0 \exp(i\omega t), \tag{3}$$

where $a_0 = f_0/m$ is the acceleration. A more general excitation in the Equation of motion includes the Abraham-Lorentz force term, $F_\mathrm{AL} = (2q^2/3c^3)\, d^3x/dt^3$ in cgs units, or $F_\mathrm{AL} = (q^2/6\pi\epsilon_0 c^3)\, d^3x/dt^3$ in SI units [81]. When the oscillator is driven the general solution in the steady-state is

$$x(t) = A \exp[i(\omega t) + \phi], \tag{4}$$

with

$$A = \frac{A_0}{\sqrt{\omega^2\gamma^2 + \left(\omega_0^2 - \omega^2\right)^2}} \quad \text{and}$$
$$\phi = \arctan\left(\frac{\gamma\omega}{\omega_0^2 - \omega^2}\right) + n\pi. \tag{5}$$

The frequency-dependent amplitude A determines the shape of the resonance. γ turns out to be the half-width of the resonance at the half maximum (HWHM). The quality factor relating the amount of energy stored in the oscillator comparing to the excitation power is given by $Q = \omega/\gamma$. When the external excitation is interrupted the oscillations decays with constant γ. The way the oscillations decays depends on the ratio $r = \gamma/(2\omega_0)$, which can be overdamped ($r > 1$), critically damped ($r = 1$), or underdamped ($r < 1$). Using this simplified model we can describe the time constant of damping $\tau = 1/\gamma$. Estimations of the decay time from measurements of the extinction spectra of plasmonic nanoparticles indicate

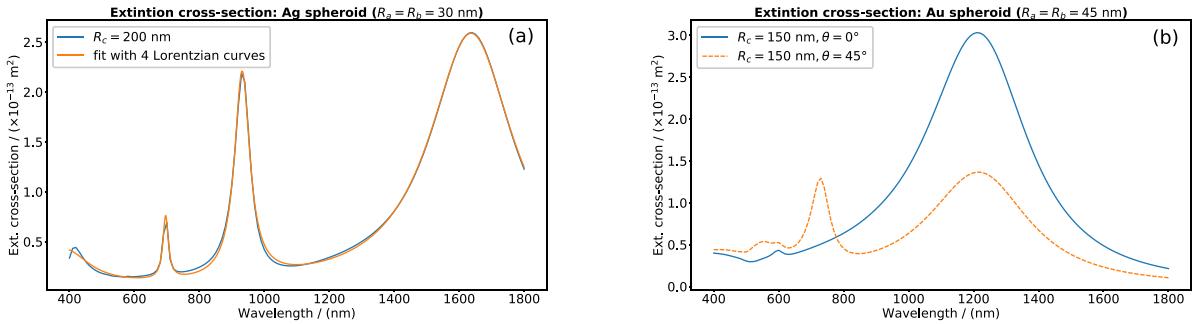

Figure 1. Extinction cross-section of silver (a) and gold (b) spheroids in homogeneous medium of refractive index $n = 1.45$. The symmetry axis of the spheroids is tilted comparing the incident electric field vector of the plane wave by 45°. For comparison, the extinction cross-section of a gold spheroid parallel to the electric field is also presented. Due to the symmetry conditions the plane wave cannot excite the quadrupole mode of a spheroid when its longest symmetry axis is parallel to the electric field. The dielectric functions used in the calculation were based on experimental values of the optical constants [7].

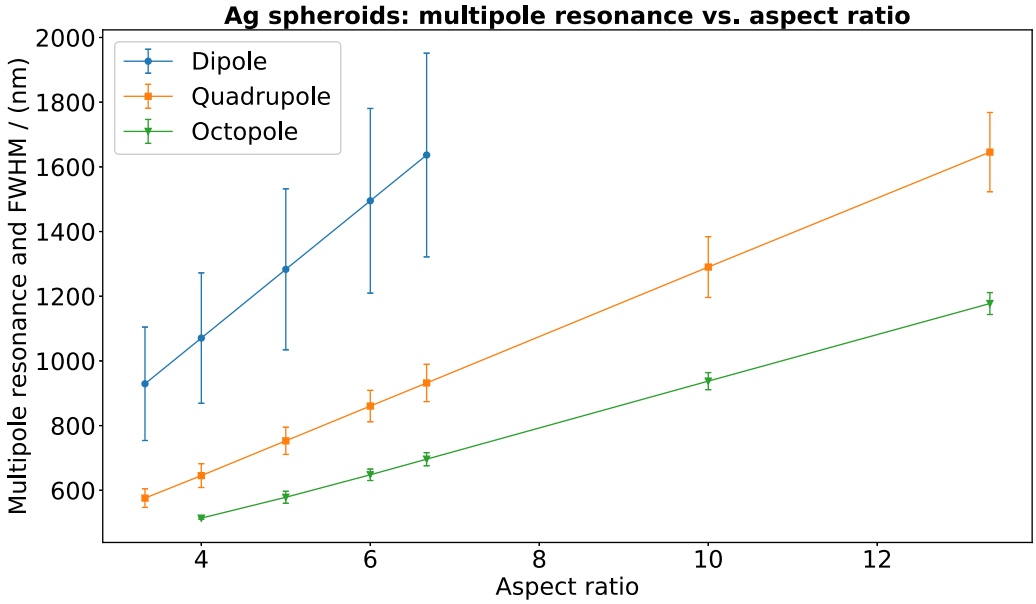

Figure 2. Extinction cross-sections and respective full-width at half-maximum (FWHM) of silver spheroids as function of their aspect ratio. The shortest semi-axis are $a = b = 30$ nm and the longest $c = 200$ nm. In all cases the refractive index of the surrounding medium is $n = 1.45$. The central wavelength of the multipolar resonances depends linearly on the aspect ratio of the spheroid. In order to excite, dipole, quadrupole and octopole resonances the symmetry axis of the spheroids is tilted to the incident electric field vector by 45°.

values of few to 10 fs [82]. However, the particle size and high pumping power in experiments leads to much longer relaxation times involving hot electron and lattice relaxations, in the order of ps [83].

The classical oscillator model is particularly useful to apply in spheroidal particles illuminated by plane wave fields in homogeneous environment. Metal nanoparticles as Mie spheres present multipolar excitations. Each multipole can be calculated individually, but the superposition of the modes leads to overlapping of the resonances in the optical extinction spectrum. Spheroidal particles and rods, by contrast, have well separated multipole resonances and thus, the extinction spectrum can be described as a sum of resonances with Lorentzian lineshape. The extinction spectra of elongated particles is dependent on the polarisation direction of the plane wave and the incoming field direction. Thus, some multipoles may be not excited for certain polarisation and illumination direction. In the left column of figure 1 is illustrated the multipolar extinction spectrum of a silver spheroid and its fitted spectrum with Lorentzian curves. In the right column are presented the extinction spectra of a gold spheroid for two distinct illumination directions.

Elongated particles as rods present narrower resonances than spherical particles of comparable volume and surface size. This is due to the different radiation damping rates [84–89] exhibited by the particles. In figure 2 the first multipoles of silver spheroids and their respective FWHM are shown, indicated by the error bars, as function of the particle aspect ratio. The shortest semi-axis is 30 nm and the longest 200 nm.

The spectral position of the longitudinal resonances scales up linearly with the aspect ratio of the particles. This has been found for elongated particles much smaller than the

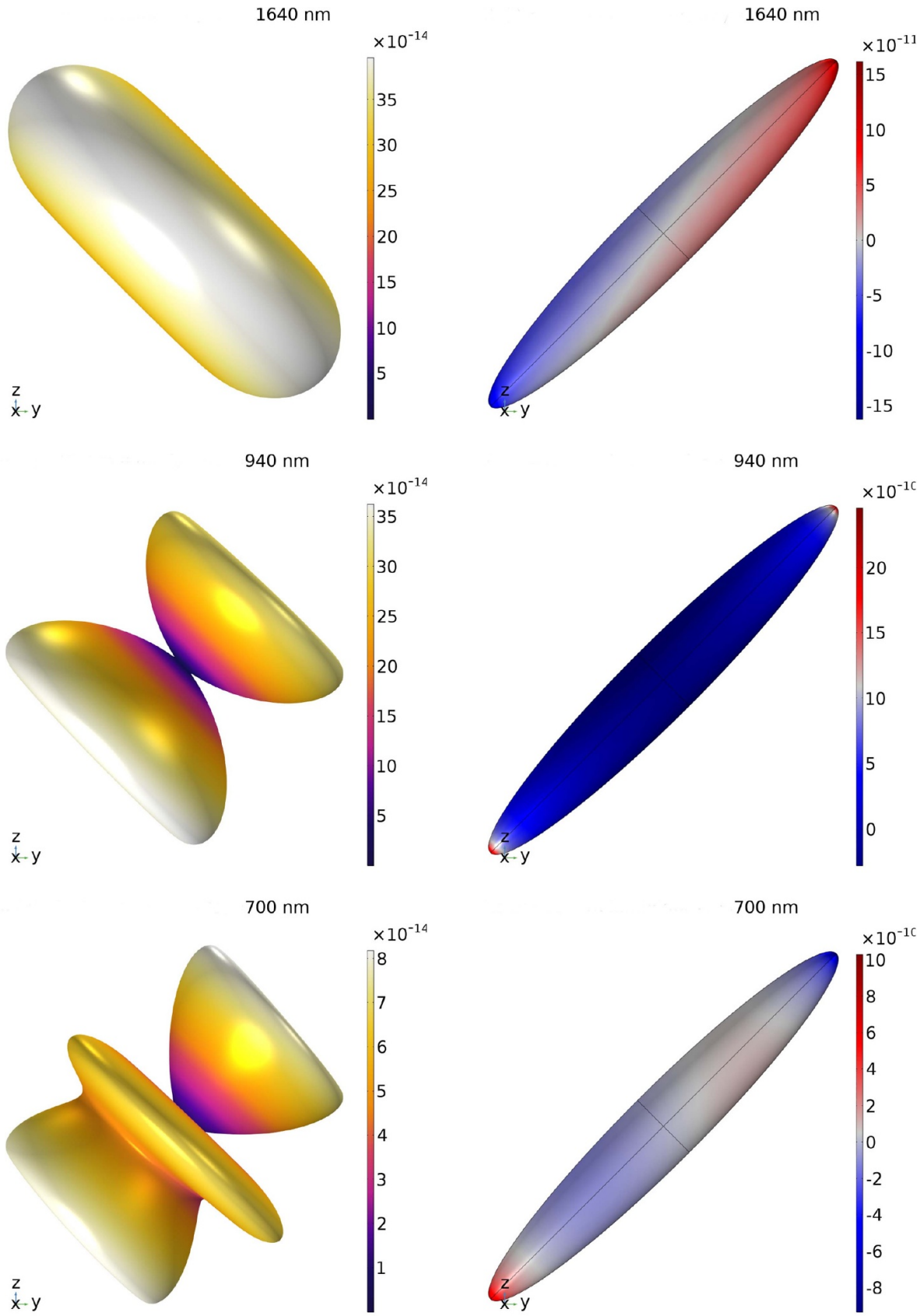

Figure 3. Radiation patterns (left) and respective surface charge distribution of a Ag spheroid of semi-axis $a = b = 30$ nm, $c = 200$ nm, for the first three resonances: dipole, quadrupole and octopole. The radiation patterns were calculated using the far-field electric strength E_{far}, by $p(\theta, \phi) = 4\pi(E_{\text{far}}/E_0)^2$.

wavelength, but also for particles of the size of the wavelength. The scaling factors also depend on the particle shape, material, refractive index of environment and multipole order [71, 90–93]. This property is particularly useful for tailoring particles, or arrays of particles to be applied as optical antennas. Like in electrostatic charge distributions surface plasmons multipoles excited in single particles are associated with distributions of surface charge. These corresponding angular spectra of these plasmon modes are as well distinct. For instance, a dipolar resonance in a spheroid has an angular spectrum of scattering of toroidal shape. In figure 3 the radiation patterns associated with the first multipoles of a silver spheroid at an angle of 45° to the incoming field direction are presented. The asymmetry of the radiation pattern is do to the particle inclination. However, for a plane wave illumination where the electric field is parallel to the particle long symmetry axis, no quadrupole is excited.

The highly localised surface charge density leads to strong near-field which is fundamental element in radiative decay engineering, non-linear optics, quantum optics and optomechanics and other levels of matter-radiation interaction. Several applications rely on enhanced near-fields, including optical nanoantennas, surface enhanced Raman scattering, plasmonic tweezers and photothermal heating and enhanced radiative decay of emitters.

3.3. Coupled oscillators

The interaction models and the discussion of the optical properties of single plasmonic particles of the previous section can extended to coupled particles. The most simple way to describe two interacting plasmonic particles is by using coupled equations of motion equations of two coupled oscillators. This elementary model is very powerful to explain a wide range of interactions, as we will see in the next sections. This model is mostly used to describe the far-field spectral features resulting from near-field interaction. The near-field patterns and corresponding surface charge distributions need a full electromagnetic calculation.

The equations of motion of two classical oscillators of free eigenfrequency $\omega_1 = \sqrt{k_1/m}$, and $\omega_2 = \sqrt{k_2/m}$ with damping constants γ_1 and γ_2 respectively, read

$$\ddot{x}_1 + \gamma_1\dot{x}_1 + \omega_1^2 x_1 + \Omega_{12}^2(x_1 - x_2) = a_0\exp(i\omega t) \tag{6a}$$

$$\ddot{x}_2 + \gamma_2\dot{x}_2 + \omega_2^2 x_2 + \Omega_{12}^2(x_2 - x_1) = 0. \tag{6b}$$

Only one oscillator is driven by an external harmonic force and the coupling strength is given by the $\Omega_{12} = \sqrt{k_{12}/m}$. The steady-state solutions, assuming the ansatz $x_i = c_i\exp(i\omega t)$ read [94–96]

$$c_1 = \frac{\omega_2^2 - \omega^2 + i\gamma_2\omega}{(\omega_1^2 - \omega^2 + i\gamma_1\omega)(\omega_2^2 - \omega^2 + i\gamma_2\omega) - \Omega_{12}^4}\,a_0 \tag{7a}$$

$$c_2 = -\frac{\Omega_{12}^2}{(\omega_1^2 - \omega^2 + i\gamma_1\omega)(\omega_2^2 - \omega^2 + i\gamma_2\omega) - \Omega_{12}^4}\,a_0. \tag{7b}$$

The complex amplitudes expressed by

$$c_1 = |c_1|\exp(i\phi_1) \qquad \text{and} \qquad c_2 = |c_2|\exp(i\phi_2) \tag{8}$$

are related the phase difference $\phi_1 - \phi_2 = \theta - \pi$, with $\theta = \arctan\left[(\gamma_2\omega)/(\omega_2^2 - \omega^2)\right]$.

This model can be used to describe coupling effects resulting in Fano resonances, classical analogue of strong coupling and the classical analogue of the electromagnetic induced transparency. All these effects have been investigated in many plasmonic resonators and form the building blocks of many applications. Notable is the fact that all these phenomena have been discovered in the context of quantum physics and have found many analogues in the classical world.

3.4. Fano resonance in plasmonic resonators

Fano found in 1961 a formula to describe quantitatively the asymmetric lineshape found in the ionisation spectra of helium [31]. It reads

$$\sigma(\varepsilon) = \frac{(q+\varepsilon)^2}{1+\varepsilon^2}, \tag{9}$$

where q is the Fano asymmetric parameter and $\varepsilon = (E - E_\phi)/(\Gamma/2)$ expresses the reduced energy at the ϕ discrete state of width Γ. σ represents the total cross-section due to the interference between the scattering amplitude in the continuum states with scattering amplitude in discrete states. The energy levels of the both continuum and discrete states have to be close to each other in order to produce interference. For $q\,\mathrm{lim}\,\infty$ the lineshape approaches the Breit–Wigner or Lorentzian symmetric resonance lineshape. For $q = 0$ the lineshape has dip at $\varepsilon = 0$. Resonances presenting lineshapes of this kind arising from destructive interference between coupled resonant systems are called Fano resonances. These resonances occur in nature in all kind of physical systems either quantum, or classical. Plasmonic coupled resonators are no exception. Systems that can be described as classical oscillators benefit from the mathematical simplifications without loosing the physical insight.

The Fano resonance in coupled classical oscillators was analysed by Joe *et al* [94]. This model has been very often applied to analyse the optical response in coupled plasmonic systems. Fano resonances have been extensively investigated for plasmonic systems in the last decades [95, 97–111]. Gallinet and Martin found a generalisation of the Fano formula for vectorial fields and lossy materials from first principles and more adequate to treat plasmonic systems [95].

$$\sigma(\kappa) = a\frac{(q+\kappa)^2 + b}{1+\kappa^2}. \tag{10}$$

Considering a non-radiative mode of frequency ω_d and intrinsic damping γ_d, the reduced frequency κ is defined by $\kappa = (\omega^2 - \omega_d^2 - \Delta\omega_d)/\Gamma$. The constants $a = (1 - \Gamma_i)^{-2}$ and $b = \kappa^2\Gamma_i^2 q^2 a$ depend on the with Γ_i of each resonance. For a non-radiative mode without losses $\Gamma_i = 0$ and the classical Fano formula is obtained.

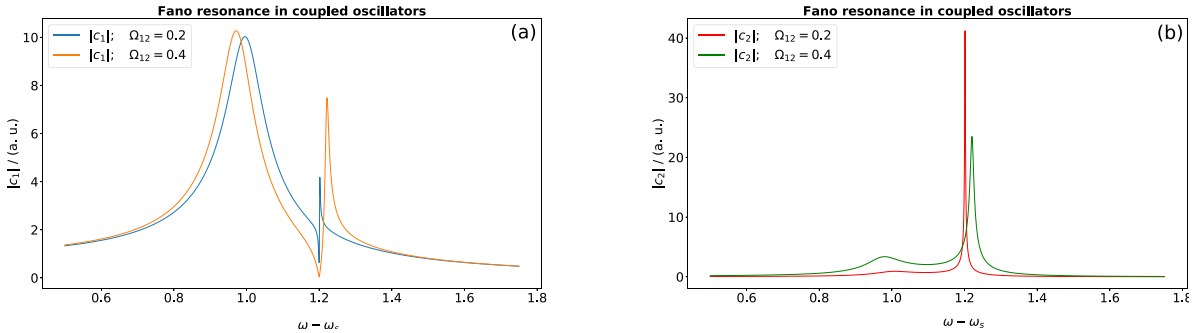

Figure 4. Amplitude of the coupled oscillators for two values of the coupling constant. A Fano lineshape arises in the amplitude spectrum of the first oscillator (a), whereas the amplitude of the second non-driven oscillator (b) becomes very large near its natural resonance. The numerical values used are: $\omega_1 = 1.0$, $\gamma_1 = 0.1$, $\omega_2 = 1.2$ and $\gamma_2 = 0.001$.

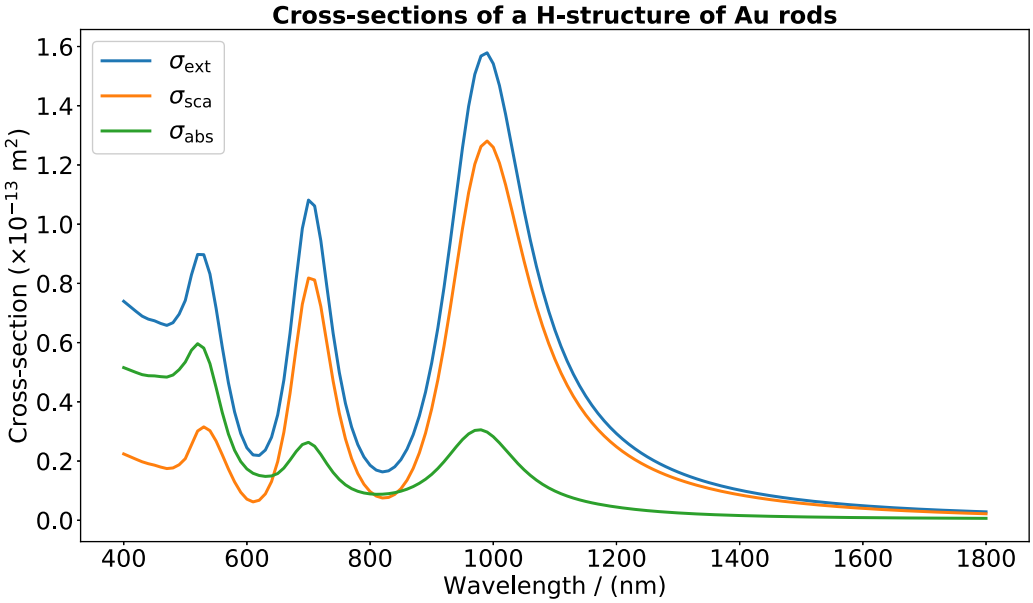

Figure 5. Cross-sections of coupled rods mounted in a H-like structure. The lengths are 300 nm for the longer rods and 120 nm for the middle rod and their separation is 10 nm. The excitation field is a plane wave with electric field oscillating parallel to the small rod. The refractive index of the medium surrounding the rods is $n = 1.45$.

In order to underline how a Fano resonance arises we use the oscillation amplitudes for the coupled oscillators found in the previous section. We assume one of the oscillators having a narrow resonance (low damping) and the other with a wide (high damping) and a low coupling constant k_{12} such that $\Omega_{12}^2 \ll (\omega_1^2 - \omega_2^2)$. The spectral position of the resonances should be proximate, but do not need to overlap. If we drive the first oscillator with an harmonic force, its amplitude presents at the resonance of the second oscillator an asymmetric lineshape 4. Simultaneously, the amplitude of second oscillator has a symmetric peak at the same resonance. This means that the excitation energy of the first oscillator is transferred to the second oscillator, resulting in a destructive interference in the motion of the driven oscillator. The corresponding phase also suffers a sudden shift of $\sim\pi$.

The same kind of interference occurs between bright (radiant) and dark (non-radiant) modes in coupled modes of plasmonic nanostructures. The Fano resonances are assessed from the extinction spectra. One of the first experimental systems evidencing a Fano resonance in the dark-field spectrum was the dolmen structure formed the three gold rods [99]. When the polarisation of the excitation field is parallel to the top rod and the rod lengths match in a way that the longitudinal dipole resonance of the top rod overlaps with the quadrupole resonance of the side rods a Fano resonance arises. Under these conditions the quadrupole resonance cannot be directly excited by the external field (dark mode), but it arises by near-field coupling. Thus, the dipolar resonance suffers a destructive interference from the quadrupole mode and presents a Fano dip.

Other example of plasmonic structure presenting Fano resonance are gold rods in H-like arrangement. The polarisation of the plane wave field in parallel to the middle rod and the lateral longer rods are not directly excited. However, due to the near-field coupling the quadrupole mode of each longer rod is excited absorbing energy from the dipole mode. The total cross-sections of the H-like structure are presented in figure 5. The corresponding radiation patterns and surface charge distribution for three different wavelengths are shown in figure 6. At the Fano dip the far-field radiation pattern is not the typical of a dipole excitation. Due to the near-field

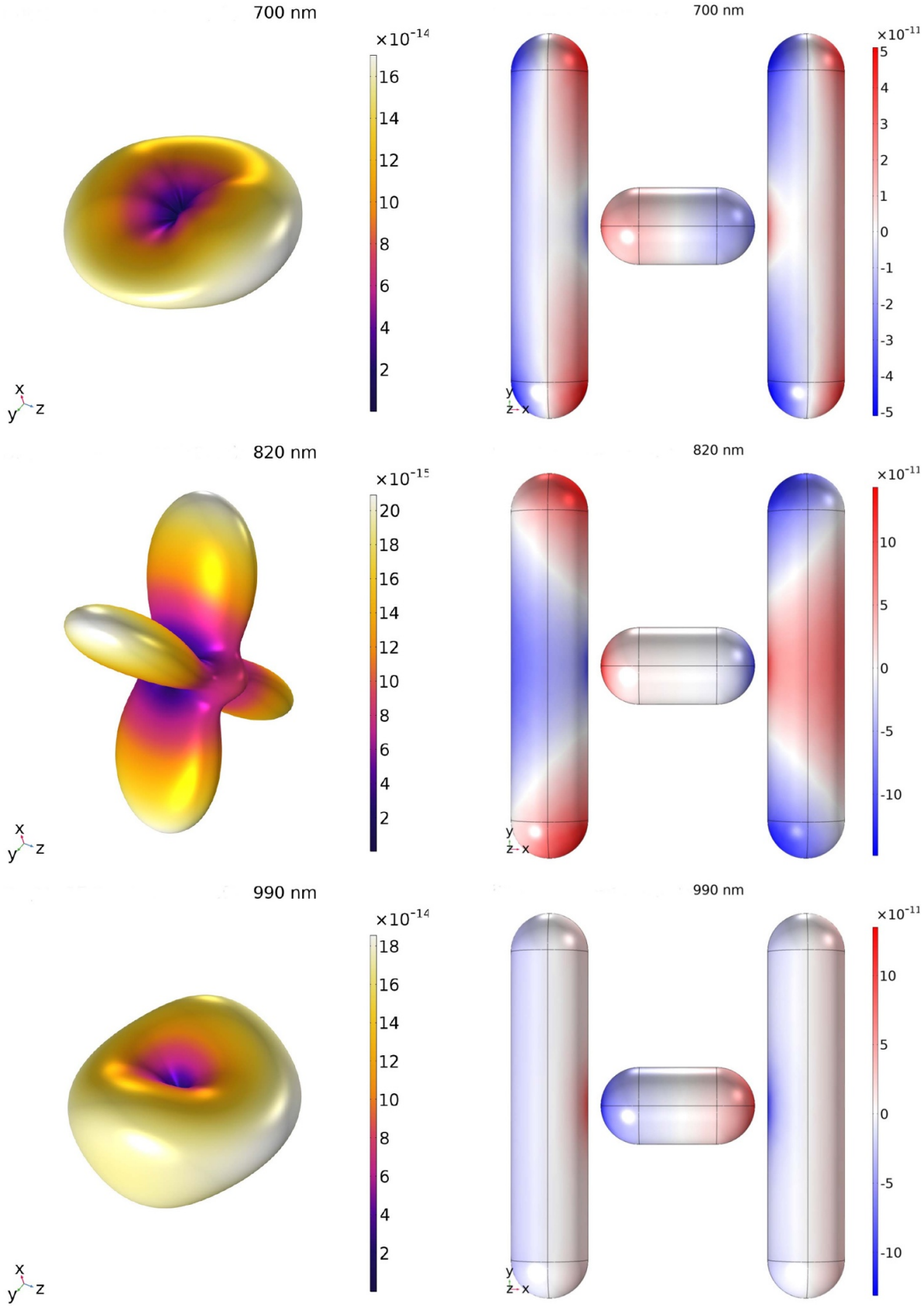

Figure 6. Radiation patterns (left) and surface charge densities (right) of coupled Au rods in medium of refractive index $n = 1.45$. The total lengths are 300 nm for the longer rods and 120 nm for the middle rod. Their separation is 10 nm. The excitation field is a plane wave with electric field oscillating parallel to the small rod.

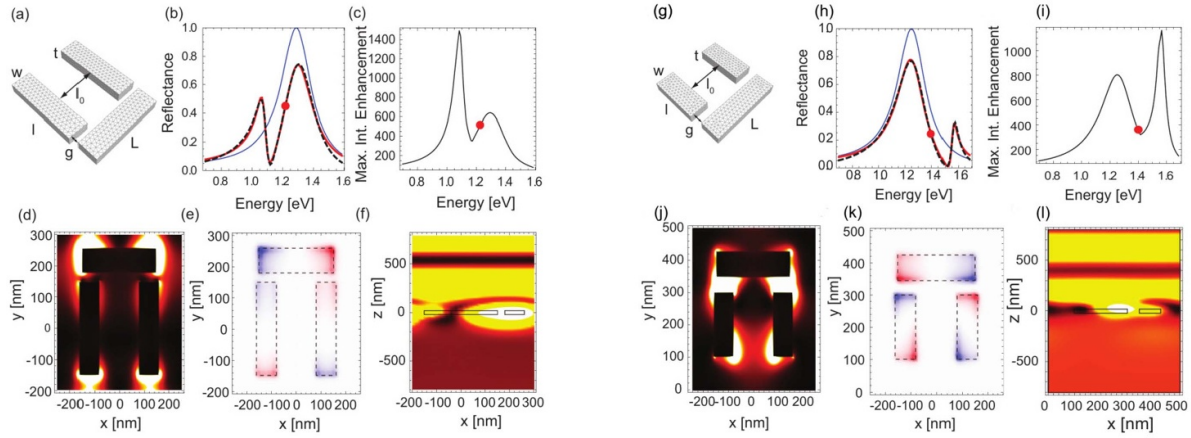

Figure 7. Fano resonance in dolmen structures. (Left) (a)–(f) Dimensions of the structures: $w = 40$ nm, $l_0 = 160$ nm, $t = 80$ nm, $g = 30$ nm, $l = 300$ nm and $L = 300$ nm. (Right) (g)–(l) Dimensions of the structures: $w = 40$ nm, $l_0 = 160$ nm, $t = 80$ nm, $g = 45$ nm, $l = 200$ nm and $L = 300$ nm. (a), (g) The figures present the geometry and dimension parameters (b), (h) reflectance spectrum at normal incidence, with polarisation along the X-axis, where the black dashed line is a numerical simulation and the thick red and thin blue lines are calculated from equations (c), (i) maximum intensity enhancement (d), (j) normalised intensity distribution for the middle plane of the structure, parallel to the XY-plane (e), (k) normalised Z-component of the electric field, 5 nm above the structure (f), (l) normalised amplitude of the Z-component of the electric field at $x = 200$ nm, for the XZ-plane. Reproduced from [102]. CC BY 4.0.

interaction with the longer rods, it presents four lobes and simultaneously decreases the intensity. At the extinction spectrum peaks surrounding the Fano dip the corresponding radiation patterns resemble those of a dipole.

Figure 7 presents the calculated reflectance, near-field maximum and near-field distribution of two dolmen structures made by rectangular rods of different sizes. The position of the Fano dip and the near-field maximum are not only sensitive to the inter-particle gap, but also on the particles dimensions. In contract with the H-like structure, the quadrupole is excited in both longer rods and not in each longer rod in a symmetric way. Thus, the near-field distributions of the Z-component of the electric field are antisymmetric (see figure 7(e)).

3.5. Strong coupling in plasmonic systems

When an emitter is in an excited state it decays spontaneously due to two pathways: a radiative and a non-radiative. Inside a cavity the radiative pathway can be strongly enhanced, due to the large increase of optical modes, and the decay rate becomes much faster than in free space. This is what happens when the lifetime of the optical mode is much shorter then the lifetime of the excited state of the emitter. This is the regime of weak coupling, arising between the emitters and cavity modes giving rise to the Purcell effect [112] for the spontaneous emission. However, if the optical mode lifetime in the cavity is longer than the lifetime of the excited state an interaction regime starts to arise between the optical mode and the emitter, resulting in an oscillatory decaying emission. This phenomenon is called Rabi oscillation. It was found by Rabi in the context of nuclear spin resonance [113]. The interaction regime is called strong-coupling, to distinguish it from the more common exponential decay of emission characteristic of the weak coupling. The Rabi oscillation in the time-dependent emitted light is associated with a spectral splitting in the emitter resonance. The spectral splitting is an attribute of the strong coupling.

The strong coupling regime of radiation-matter interaction can be described at three levels [114]: (a) quantum optical, describing the interaction of a two-level quantum system interacting with a quantised electromagnetic field; (b) semi-classical, where the field electromagnetic field is treated classically; (c) classical Lorentzian oscillator and classical electromagnetic field. The classical case has been already introduced by Novotny [115] and more recently discussed by Törmä and Barnes [114]. The fully quantised case has been subject of thorough studies in cavity quantum electrodynamics [116–118].

In order to appreciate the importance of the strong coupling in plasmonic systems we analyse strong coupling using classical oscillators, as in the case of the Fano resonance. Following the method of Novotny [115], we first write the equations of the undriven coupled oscillators of equal mass

$$\ddot{x}_1 + \gamma_1\dot{x}_1 + (k_1/m_1)x_1 + (k_{12}/m_1)(x_1 - x_2) \quad = 0 \quad (11a)$$

$$\ddot{x}_2 + \gamma_2\dot{x}_2 + (k_2/m_2)x_2 + (k_{12}/m_2)(x_2 - x_1) \quad = 0. \quad (11b)$$

To simplify the solution we set $\gamma_i = 0$,

$$\ddot{x}_1 + [(k_1 + k_{12})/m_1]x_1 - (k_{12}/m_1)x_2 \quad = 0 \qquad (12a)$$

$$\ddot{x}_2 + [(k_2 + k_{12})/m_2]x_2 - (k_{12}/m_2)x_1 \quad = 0. \qquad (12b)$$

Without coupling ($k_{12} = 0$) the eigenmodes have frequencies $\omega_{0,1} = \sqrt{k_1/m}$ and $\omega_{0,2} = \sqrt{k_2/m}$. Using the ansatz $x_i = A_i \exp(-i\omega_{\pm}t)$, we find the eigenfrequencies arising for non-zero coupling [115]

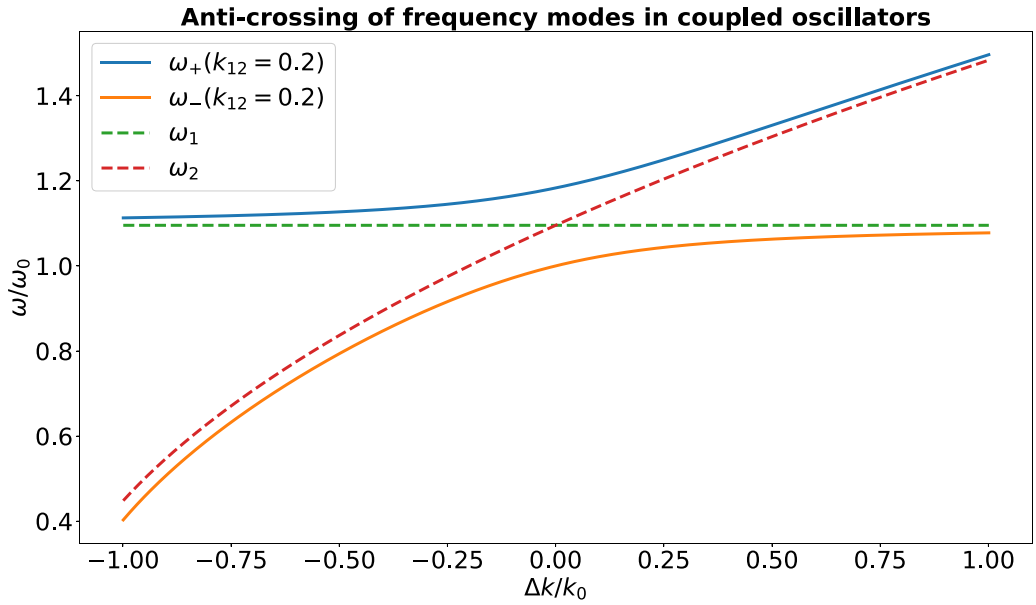

Figure 8. Strong coupling in classical oscillators. In the absence of coupling the eigenfrequencies cross. When the resonators are coupled, an anti-crossing arises, and the separation between the eigenfrequencies Γ is proportional to k_{12}. The numerical values used are $k_1 = k_0 = 1.0$, $m_1 = m_2 = 1.0$, $k_2 = k_0 + \Delta k$, $k_{12} = 0.2k_0$.

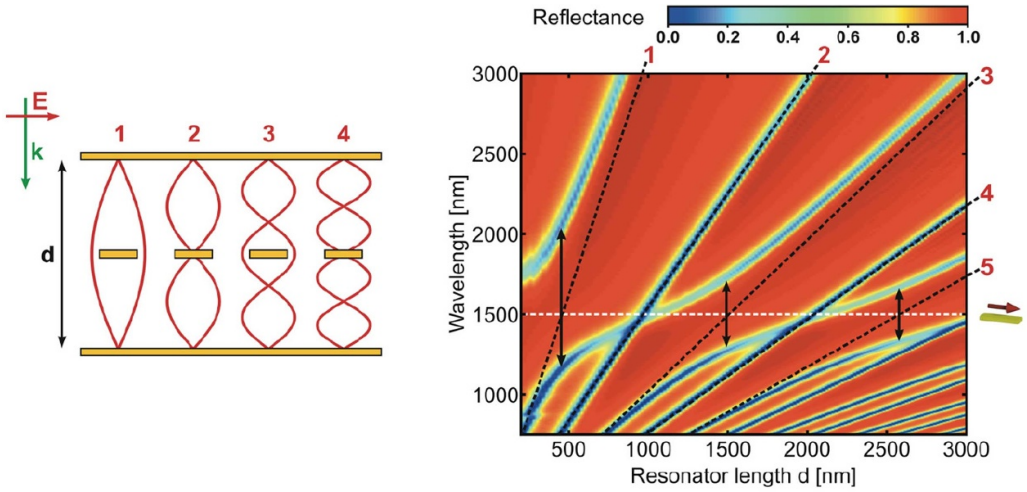

Figure 9. Reflectance presenting strong coupling between photonic cavity modes and plasmonic resonance modes of a intra-cavity rod particle. The dashed white and black lines correspond to the unperturbed plasmon and optical cavity modes, respectively. The black arrows indicate the anti-crossing. [120] John Wiley & Sons. © 2013 WILEY-VCH Verlag GmbH & Co. KGaA, Weinheim.

$$\omega_+ = \tfrac{1}{2}\left[\omega_1^2+\omega_2^2+\sqrt{(\omega_1^2-\omega_2^2)^2+4\Gamma^2\omega_1\omega_2}\right] \quad (13a)$$

$$\omega_- = \tfrac{1}{2}\left[\omega_1^2+\omega_2^2-\sqrt{(\omega_1^2-\omega_2^2)^2+4\Gamma^2\omega_1\omega_2}\right] \quad (13b)$$

with $\omega_1 = \sqrt{(k_1+k_{12})/m_1}$, $\omega_2 = \sqrt{(k_2+k_{12})/m_2}$ and $\Gamma = \sqrt{k_{12}/m_1}\sqrt{k_{12}/m_2}/\sqrt{\omega_1\omega_2}$. We can make k_2 dependent on a parameter k and $k_1 = k_0$ having a fixed value. We have then $k_2 = k_0 + \Delta k$. Thus, when $k_2 = k_0$, both eigenfrequencies have the same value. We can now vary Δk between $-k_0$ and k_0 and obtain the respective ω_+ and ω_-. Assuming that both masses are identical $m_1 = m_2 = m$, it easy to see that the eigenfrequencies cross for $k_{12} = 0$. However, for non-zero k_{12} an anti-crossing arises in the values of ω_+ and ω_-. The way we change the value of k_2 was purely arbitrary. It was chosen with the only purpose to make the eigenfrequencies dependent on a parameter that leads to crossing, in the absence of coupling. Figure 8 illustrates the anti-crossing of modes in coupled oscillators as function of the parameter Δk.

Following the approach of Novotny [115], we first write the equations of the undriven coupled oscillators

$$\ddot{x}_1 + \gamma_1\dot{x}_1 + (k_1/m_1)x_1 + (k_{12}/m_1)(x_1 - x_2) = 0 \quad (14a)$$

$$\ddot{x}_2 + \gamma_2\dot{x}_2 + (k_2/m_2)x_2 + (k_{12}/m_2)(x_2 - x_1) = 0. \quad (14b)$$

To simplify the solution we set $\gamma_i = 0$,

$$\ddot{x}_1 + [(k_1 + k_{12})/m_1]x_1 - (k_{12}/m_1)x_2 \quad = 0 \qquad (15a)$$

$$\ddot{x}_2 + [(k_2 + k_{12})/m_2]x_2 - (k_{12}/m_2)x_1 \quad = 0. \qquad (15b)$$

Without coupling ($k_{12} = 0$) the eigenmodes have frequencies $\omega_{0,1} = \sqrt{k_1/m}$ and $\omega_{0,2} = \sqrt{k_2/m}$. Using the ansatz $x_i = A_i \exp(-i\omega_{\pm}t)$, we find the eigenfrequencies arising for non-zero coupling [115]

$$\omega_+ \quad = \tfrac{1}{2}\left[\omega_1^2 + \omega_2^2 + \sqrt{(\omega_1^2 - \omega_2^2)^2 + 4\Gamma^2\omega_1\omega_2}\right] \qquad (16a)$$

$$\omega_- \quad = \tfrac{1}{2}\left[\omega_1^2 + \omega_2^2 - \sqrt{(\omega_1^2 - \omega_2^2)^2 + 4\Gamma^2\omega_1\omega_2}\right] \qquad (16b)$$

with $\omega_1 = \sqrt{(k_1 + k_{12})/m_1}$, $\omega_2 = \sqrt{(k_2 + k_{12})/m_2}$ and $\Gamma = \sqrt{k_{12}/m_1}\sqrt{k_{12}/m_2}/\sqrt{\omega_1\omega_2}$. We make k_2 dependent on a parameter k and set $k_1 = k_0$ to a fixed value. The dependence of k_2 on the parameter k is arbitrary, but must allow a matching point between k_1 and k_2. Thus, we set $k_2 = k_0 + \Delta k$. When $k_2 = k_0$, both eigenfrequencies have the same value. We can now vary Δk between $-k_0$ and k_0 and obtain the respective ω_+ and ω_-. Assuming that both masses are identical $m_1 = m_2 = m$, it easy to see that the eigenfrequencies cross for $k_{12} = 0$. However, for non-zero k_{12} an anti-crossing arises between ω_+ and ω_- as function of Δk. Figure 8 illustrates the anti-crossing of modes in coupled oscillators as function of the parameter Δk.

We point out that the anti-crossing observed in the dispersion relation characteristic of strong coupling also arises for other coupled oscillators, for instance in photonic resonators, cavity quantum electrodynamics with single emitters and in many solid state systems. The first requirement is that their dispersion relations can cross at some point in the (k, ω) space, if considered uncoupled. The second is the requirement that the coupling must be stronger than the decay rates of the resonators, or the decay rate of the excited state of an emitter coupled with the resonator. Thus, the term 'strong coupling' applied in the present context should be distinguished from other contexts of physical theories.

A very useful and intuitive way to analyse the strong coupling regime in plasmonics was developed by Novotny and Törmä and Barnes [114, 115]. The spectrum of a nanoscale emitter of frequency ω_e and damping rate γ_e is represented by a Lorentzian curve [80]. The Lorentzian expression can be found from the motion equation of the undriven damped oscillator model of a point dipole. As the emitter size is much smaller than the wavelength of light, we can assume that its dispersion is independent of the k-vector. It is represented by a horizontal line in the dispersion relation map (ω, k). A surface plasmon-polariton (SPP) by the other side is dispersive. The dispersion relation reads

$$k_{\mathrm{SPP}} = \frac{\omega}{c}\sqrt{\frac{\epsilon_m\epsilon_d}{\epsilon_m + \epsilon_d}} \qquad (17)$$

where ε_m is the dielectric function of the metal and ε_d is the dielectric function of the dielectric. We can assume for the sake of simplicity that the metal is a Drude metal. The dispersion curve of the SPP is always localised at the right of the light line. When the central frequency ω_0 of the emitter overlaps the SPP dispersion both lines would cross. Under certain conditions, however, there no crossing in the dispersion curves of the emitter-SPP system rather an anti-crossing. The condition is the following: the coupling constant between the emitter and the SPP must be larger than the sum of the decays rates of both [114, 115]. More recently, other conditions for the strong coupling and the anti-crossing were discussed by Rodriguez [119]. When the coupling constant is smaller than the damping, only weak coupling occurs and leads to the Purcel effect. Strong coupling has been predicted and observed experimentally in many different optical systems. The classical strong coupling between an optical cavity and a plasmonic particle is illustrated in figure 9.

The strong coupling between a plasmonic resonator and a single emitter is difficult to achieve experimentally. In general only weak coupling is achieved. However, quantum emitters in small gap cavities can lead to strong coupling at room temperatures. Despite the low Q-factor of these cavities, the mode volumes are much smaller than for photonic resonators and thus, strong coupling based on a single molecule was measured (see figures 10 and 11).

3.6. Plasmonic analogy of the electromagnetic induced transparency

Electromagnetic induced transparency (EIT) is a term coined by Harris and coworkers to describe how an opaque medium may transmit radiation at its resonance [122–125]. It occurs in vapour cells of three level atoms. The description of the mechanism leading to EIT is based on transition between quantum states of three different energy levels. One of the schemes is based on a laser source tuned between the upper level $|3>$ and the lowest level $|1>$ (probe field of frequency ω_p) and a second laser is tuned around the middle level $|2>$ and the state $|3>$ (coupling laser field of frequency ω_c). The dipole-transition between the states $|1>$ and $|2>$ is forbidden. The coupling laser interacts with the upper state and is responsible for bringing large amount of atoms to the a steady state $|2>$. This results in a sudden drop of intensity in the absorption spectrum at its resonance peak. This phenomenon has been extensively investigated for many quantum systems [125]. A related effect is the strong reduction of the speed of light propagating in cold atoms supporting EIT [126].

A classical analogy of the EIT based on two coupled oscillators was developed by Alzar *et al* [96]. It is similar to the Fano resonance, but the resonances of both oscillators overlap. In order to observe a narrow dip in the absorption spectrum of the driven oscillator the non driven oscillator must have a much smaller damping constant. The central dip in the absorption spectrum of the driven oscillator mimics the EIT observed in atomic vapours. Moreover, this simple model of EIT has been also applied in the analysis of coupled plasmonic resonators

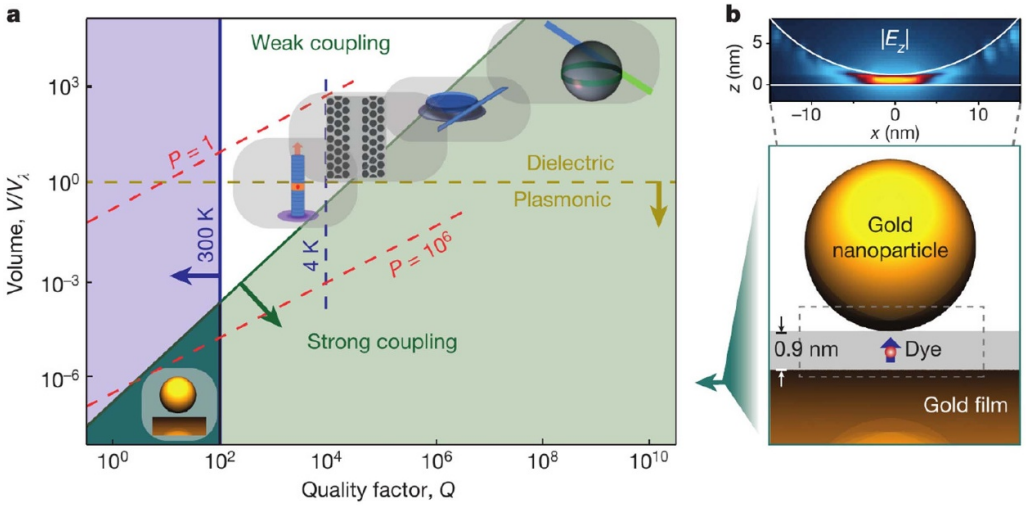

Figure 10. Strong and weak coupling of single emitter with a cavity. (a) Quality factor Q, effective mode volume $V/(\lambda/n)^3$ and Purcell factor P (dashed red lines) distinguishing the strong and weak coupling regimes and temperature ranges. The position of the several resonators indicate their approximate quality factor and mode volume. (b) Single dye molecule between a gold film and a gold sphere. The maximum electric field enhancement reaches 400. At very small mode volumes and low quality factors is possible to achieve room temperature strong coupling with single emitters. Reprinted by permission from Springer Nature Customer Service Centre GmbH: Nature [121] (2016).

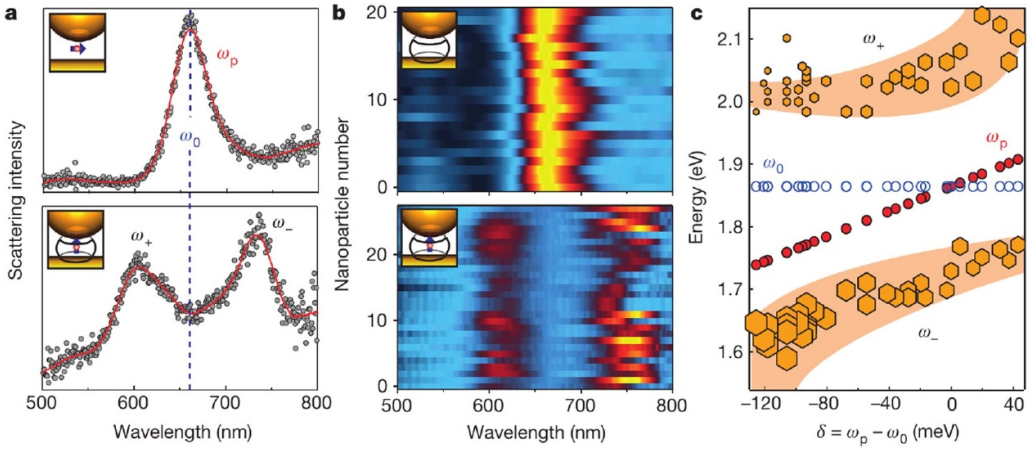

Figure 11. Strong coupling of a single methylene blue molecule with a plasmonic cavity formed by a mirror and a gold sphere. (a) When the molecule dipole is oriented parallel to the mirror, the scattering spectrum is the same of a plasmonic system without molecule. When the molecule dipole is oriented perpendicular to the mirror a splitting arises in the scattering spectrum, characteristic of the anti-crossing in the strong coupling regime. (b) Scattering spectra for multiple individual cavities for (top) empty cavity and (bottom) cavity filled width a monolayer of cucurbit[7]uril (CB[7]) molecules. (c) Resonant positions of methylene blue molecules, plasmonic cavity and the hybrid modes of the strong coupling, as function of the detuning from the central frequency ω_0. Reprinted by permission from Springer Nature Customer Service Centre GmbH: Nature [121] (2016).

leading to induced transparency by near-field coupling [127–129].

Figure 12 presents the power absorbed in the first oscillator (driven) and the corresponding dispersion, obtained by the real part of the oscillator amplitude c_1, as function of the detuning frequency. Although the resonances arising in plasmonic resonators by coupling radiative dipole modes with dark quadrupole modes is usually classified as a Fano resonance, it can be seen as a plasmonic variant of the electromagnetic induced transparency. This is particularly true when the bright and dark modes overlap and the transmission increases at the Fano dip, because the destructive interaction strongly reduces the extinction. Figure 13 presents the transmittance and reflectance of arrays of stacked plasmonic rods fabricated by electron beam lithography, where the upper rod is progressively dislocated from he centre in each array. When the central rod is located above the ends of the lower parallel rods a maximum in the transmittance is reached. When it is in the middle position the transmittance drops to a minimum.

3.7. Parametric resonances

A parametric oscillator can be defined as an oscillator with a harmonic time-dependent oscillation frequency. Harmonic oscillators have constant frequency of oscillation ω_0. In the parametric case the oscillation frequency is externally driven.

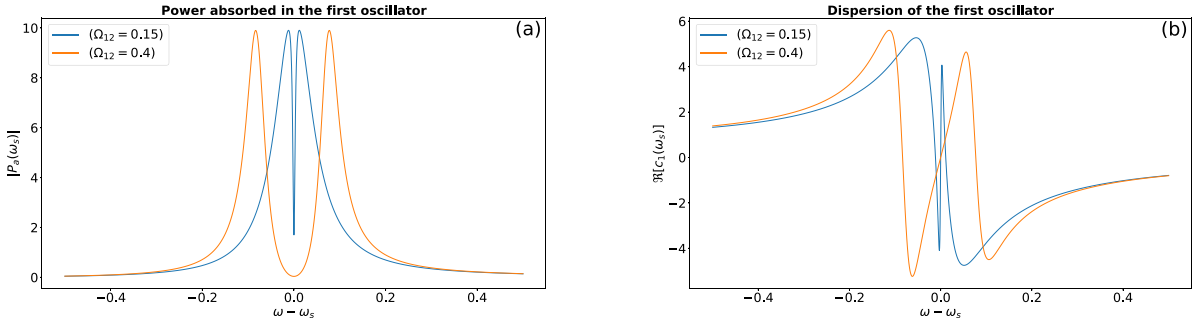

Figure 12. Classical analogy of electromagnetic induced transparency. When two classical oscillators are coupled and one of them is externally driven and their eigenmodes overlap the driven oscillator presents a deep in its absorption spectrum (a). The pronounced deep corresponds to the classical analogy of the electromagnetic induced transparency, arising in some three level quantum systems. The real part of its amplitude contains the dispersion (b). The numerical values used in the calculation of the absorbed power are $\omega_1 = 1.0$, $\gamma_1 = 0.1$, $\omega_2 = 1.0$, $\gamma_2 = 0.001$. When the coupling constant Ω_{12} increases the width of the transparency increases.

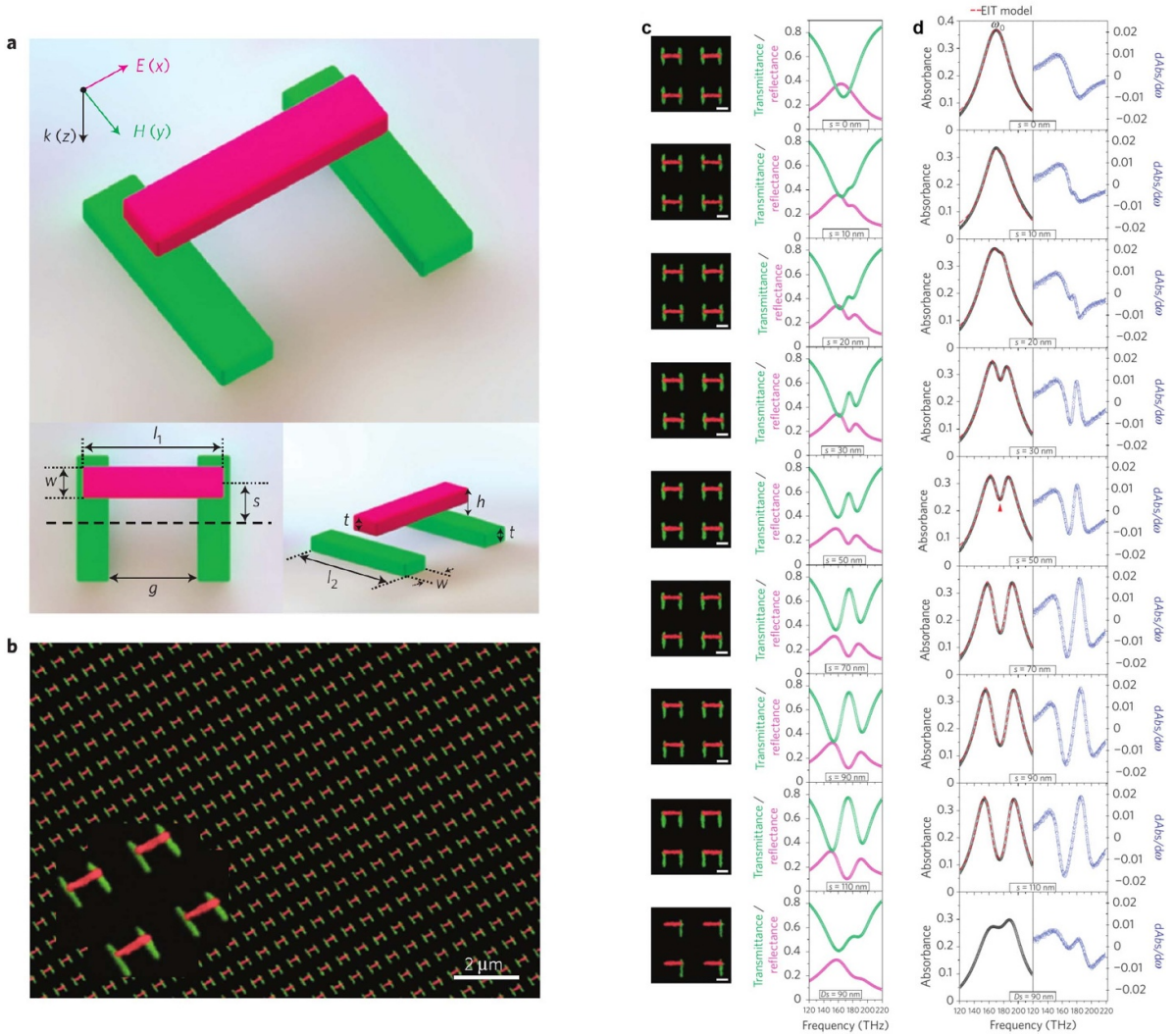

Figure 13. (Left) (a) Schematics of the stacked structure used for the plasmonic analogue of electromagnetic induced transparency. Sizes of the geometrical parameters: $l_1 = 355$ nm, $l_2 = 315$ nm, $w = 80$ nm, $g = 220$ nm, $t = 40$ nm and $h = 70$ nm. The periods of the lattice in both directions is 700 nm. (b) Oblique view of the sample with the lateral displacement $s = 10$ nm. The structures consists of gold rods embedded in a photopolymer (PC403), used as a spacer. (Right) (c) SEM micrographs of the fabricated structures and corresponding measurements of the transmittance and reflectance spectra. (d) Black circles represent the experimental absorbance ($A = 1 - T - R$). The red dashed curves are fittings based on two coupled oscillators model. The blue circles represent the derivatives of the experimental $dA/d\omega$. Large transmittance occurs when the central rod is displaced to the edge. Reprinted by permission from Springer Nature Customer Service Centre GmbH: Nature Materials [127] (2009).

One of the most simple examples of parametric oscillators is the pumping of a swing [130–132]. A person sitting, or standing in a swing can pump the motion by changing the position of the centre of mass of the body. If this is done periodically, the oscillation amplitude can increase. Rayleigh was the first to present a general theory of the parametric oscillator [133]. An example of parametric oscillator based on a mechanical oscillators and two coupled RLC electric circuits is presented in [134]. The mechanical oscillator is coupled to the first electrical circuit by a capacitor which capacity changes periodically in time, and thus driving the first RLC circuit.

The equation of motion of a driven parametric oscillator reads

$$\ddot{x} + \gamma\dot{x} + f(t)x = a_0 \exp(i\omega t), \tag{18}$$

where we substitute the constant ω_0^2 by $f(t) = f(t+T)$, a periodic function of time. The resulting equation for the period in time $T = \pi$ is called Hill equation [135]. The specific case where $f(t) = \omega_0^2[1 + \eta\cos(2\omega t)]$ corresponds to the Mathieu equation, with applications in dynamic problems as inverted pendulum, quadrupole mass spectrometers, quadrupole ion trap, and also in quantum physics. The amplitude η should be small, i.e. $\eta \ll 1$ to achieve stability. Although the Equation is linear, the time-dependent coefficient hinders to find easily stable solutions [136].

The theory of the optical parametric amplifier (OPA) was developed just few years after the invention of the laser [137–139] accompanied by the first experimental demonstration [139]. Though, it took a long time until the first commercial OPAs were available. The main drawback was the quality necessary for the non-linear medium (beta barium borate, or BBO) required to operate the OPAs. Nowadays there are many applications in laser physics based on OPAs. The interaction of a strong laser field (pump laser of frequency ω_p) with the non-linear medium leads to the generation of two coherent laser fields by a process called wave mixing. The idler of frequency $\omega_i < \omega_2/2$ and the signal of frequency $\omega_s > \omega_p/2$, such that $\omega_p = \omega_i + \omega_s$, dictated by the conservation of energy. As well, the phase matching requires that the wavevectors verify $k_p = k_i + k_s$. The interaction of the laser with the BBO results in a non-linear amplification process with tunable output frequencies.

Only few publications appeared so far dedicated to parametric oscillations in plasmonic systems [141–143]. However, the coupling between plasmonic systems and other kind of oscillators seems very promising to this end. For instance, the coupling between a plasmonic excitation on parallel thin gold stripes and the underlying silicon nitride film supporting acoustic vibrations can lead to a parametric resonance [144].

4. Survey of applications of plasmonic resonators

In this section we present several applications of plasmonic resonators and discuss their main characteristics. One of the earliest applications was in the detection of molecules by surface enhanced Raman scattering [145]. This effect has been subject of intensive research and there are numerous reviews available [56, 146–152]. Therefore, it is not treated in this article. Although not exhaustive, this section gives an overview of the major applications relying on plasmonic resonators interacting with electromagnetic radiation and electron beams, and covers several types of effects on the matter in the neighbourhood of the resonator.

4.1. Purcell effect

Purcell published a short abstract in the Proceedings of the American Physical Society, in 1946, showing how the spontaneous emission of nuclear magnetic moment transitions could be changed inside a resonant cavity [112]. The formula reads

$$F_P = \frac{3Q}{4\pi^2}\frac{\lambda^3}{V_m} \tag{19}$$

where Q is the quality factor of the cavity and V the volume of the resonator. An intrinsically related effect is the inhibition of the spontaneous emission [153]. Because no restrictions are made in the kind of spontaneous emission this result can be generalised for any spontaneous emission system inside a resonator. In optical systems a correction has to be done by introducing the refractive index of the cavity n, $\lambda \to \lambda/n$. The mode volume V_m deserves special attention. In non-dissipative resonators of very large Q-factor the normal modes are strongly confined inside the cavity and thus, the mode volume can be evaluated by

$$V_m = \frac{\int \epsilon|E|^2 d^3r}{\max(\epsilon|E|^2)}, \tag{20}$$

where E is the electric field strength and ε the dielectric function. However, for dissipative and dispersive media and plasmonic materials the integrand would be negative, leading to an incorrect result for the mode volume. Maier and Koenderink proposed a redefinition of the electric energy stored in the cavity, using a former theory of the energy density in a dispersive and absorptive material by Ruppin, in order to evaluate the mode volume [154–156]. The relative electrical energy density reads then

$$W_e = [\Re(\epsilon) + 2\omega\Im(\epsilon)/\Gamma_e]|E|^2, \tag{21}$$

where ω is the angular frequency and Γ_e the damping constant of the oscillator. $\Re(\epsilon)$ and $\Im(\epsilon)$ denote the real and imaginary part of the permittivity. Kristensen and Hughes proposed other method to evaluate the mode volume by calculation the density of quasi-normal modes [157, 158].

Plasmonic resonators have small Q factors (range of 1 to tens), due to the intrinsic losses of the metal. Despite that, due to the much larger confinement of the modes than in photonic cavities, the mode volumes can be very small and Purcell factors of 100 s, or even larger then 1000 can be achieved [159–163]. Thus, the Purcell factor remains a measure of the efficiency of a resonator in terms of decay rate, which is fundamental in radiative decay engineering. Plasmonic resonators offer an relevant advantage over photonic

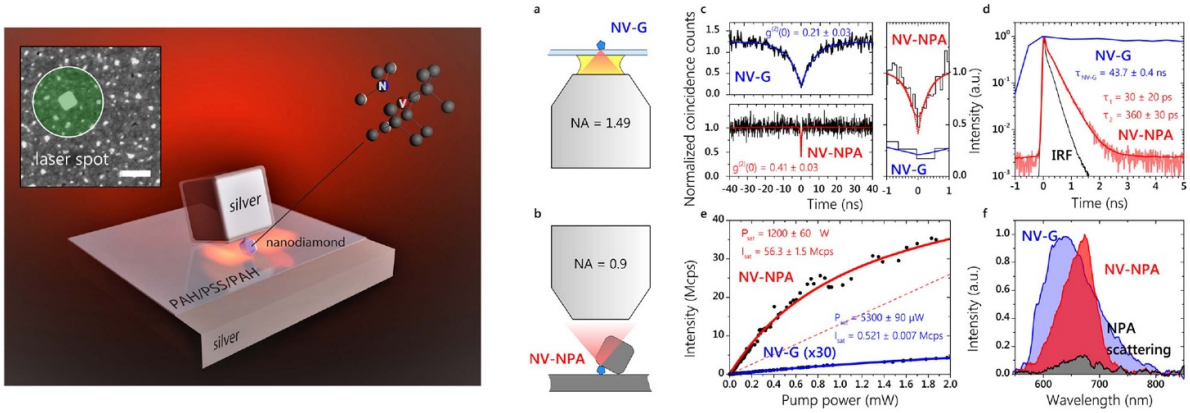

Figure 14. (Left) Purcell effect on a nitrogen vacancy (NV) in a nanodiamond between a silver cube and a flat silver surface. (Left) Schematics of the NV emitter near the antenna. The inset shows a top view SEM micrograph of the cubic antenna of 100 nm and a random dispersion of nanodiamonds on the surface. (Right) Schematic illustrations of the illumination setup for a single nanodiamond on a cover slip (NV-G) (a) and attached to the nanoantenna (NV-NPA) (b). Characterisation of NV-G (blue) and NV-NPA (red) by autocorrelation based on coincidence measurement (c), fluorescence decay (d) and saturation of fluorescence (e). (f) NV-G and NV-NPA emission and nanoparticle scattering spectra. Reprinted with permission from [164]. Copyright (2018) American Chemical Society.

cavities: their modes confinement is much larger than the diffraction limit of light and, therefore, can be integrated in devices using much smaller space.

In figure 14 experimental results recently achieved based on the Purcell effect of a nanosized emitter are presented. A nitrogen-vacancy (NV) in a nanodiamond is located under a cubic silver antenna, on top of silver surface coated by a poly-electrolyte. The presence of strong near-field due to the plasmonic nanoantenna on the NV leads to a much emission rate and a reduction of its fluorescence lifetime.

4.2. *Extraordinary optical transmission*

The enhanced optical transmission through sub-wavelength holes drilled in a thin metal film was reported by Ebbesen and collaborators in 1998 [26]. The term extraordinary was used to stress the enhanced transmission at some wavelengths in the visible and NIR, comparing to the theoretical prediction obtained from the theory of Bethe–Bouwkamp [27, 165] (see figure 15). The Bethe theory of diffraction together with the improvements of Bouwkamp were taken as reference for a circular aperture in a perfectly electric conductor screen. Therefore, it was expected a reduced transmission in a real material with nonzero absorption and not larger. More recently, Yi and collaborators compared theoretically and experimentally the different regimes of diffraction arising for a single aperture in a real metallic screen of thickness several times larger than the skin depth of metal [166]. They have shown that the Bethe–Bouwkamp theory cannot account for surface plasmons and thus, cannot explain the enhanced transmission. Already in 2001, the importance of the contribution of plasmon tunnelling for the optical transmission was pointed out [167].

Generalising the coupling condition with light for one-dimensional gratings [17, 19, 21], plasmons in periodic two-dimensional gratings or arrays of holes observe the following phase matching condition

$$\mathbf{k}_{\mathrm{SPP}} = \mathbf{k}_0 \sin\theta \pm n\mathbf{G}_x + \pm m\mathbf{G}_y, \tag{22}$$

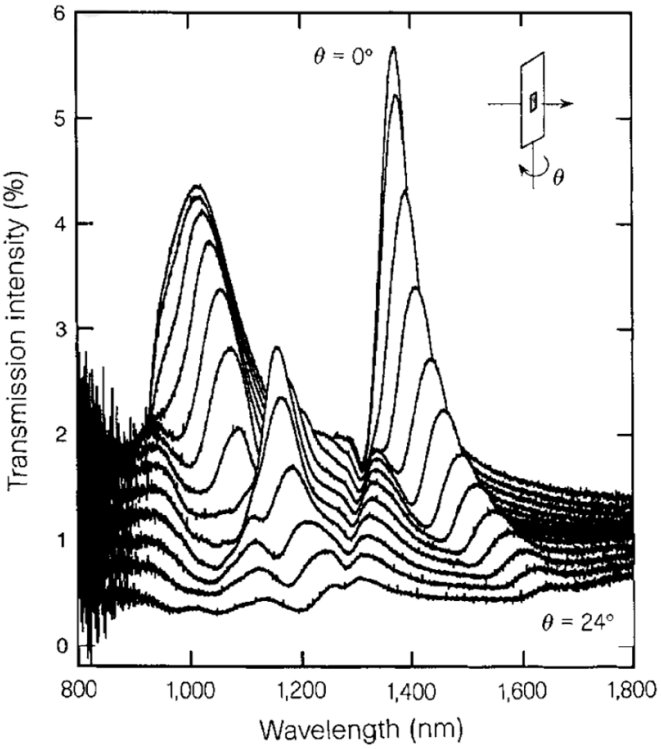

Figure 15. Transmitted spectra acquired for angles between 0 and 24 degrees, in steps of 2 degrees, of a square array of circular apertures in a silver film. Film thickness: $t = 200$ nm, lattice constant: $a_0 = 900$ nm, hole diameter: $d = 150$ nm. The individual spectra were shifted vertically by 1% for clarity. The surface plasmons dispersion relation for the square lattice can be found from $k_{spp} = k_{\|} \pm nG_x \pm mG_y$, where $k_{\|} = (2\pi/\lambda)\sin\theta$ is the in-plane k-vector of the incident light and $G_x = G_y = 2\pi/a_0$ are the reciprocal lattice constants. Reprinted by permission from Springer Nature Customer Service Centre GmbH: Nature [26] (1998).

with n, m being integers. We assume for sake of simplicity that $\mathbf{k}_0$ is the free space k-vector and the reciprocal lattice constants are $|\mathbf{G}_x| = 2\pi/\Lambda_x$ and $|\mathbf{G}_y| = 2\pi/\Lambda_y$, respectively. Contrarily

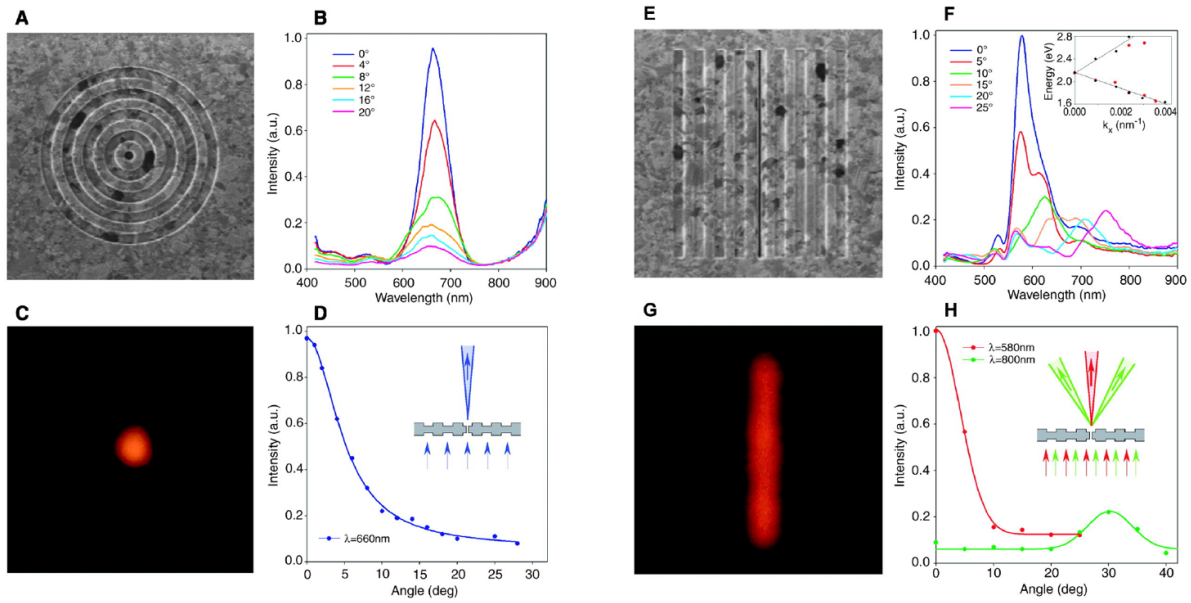

Figure 16. (Left) Optical beaming obtained from a circular aperture surrounded by a Bull's eye structure, formed by concentric circular grooves in a silver film. (A) FIB micrograph of the structure. (B) Spectra collected for various angles. (C) Red light optical image. (D) Schematics of the structure and illumination and angular dependent intensity for a single wavelength. (Right) Optical beaming from a linear slit surrounded by parallel grooves. (E) FIB micrograph of the structure. (F) Spectra collected for different angles. (G) Optical image of beamed line of light. (H) Schematics and angular dependence of the transmitted intensity for two wavelengths. From [171]. Reprinted with permission from AAAS.

to flat surfaces, plane waves with any degree of polarisation can excite surface plasmons for values of the θ matching the phase.

The connection between the optical transmission in arrays of apertures and the Fano resonance was discussed by Genet *et al* [168]. The fact that plasmon can tunnel light in periodic metal-dielectric structures lead to the development of metamaterials supporting both electric and magnetic resonant modes (fishnet structure) [169, 170], light beaming [171], optical imaging [39]. Some holes surrounded by nanostructured surfaces present optical beaming, This is a kind of light focusing in the perpendicular direction to the plane of the aperture. Examples of optical beaming are presented in figure 16.

Several reviews on the optical transmission by arrays of apertures have given a perspective of the importance of the topic in plasmonics [172, 173]. The optical resonances in free-standing arrays of wires are also related those supported on arrays of holes in compact films. The comparative analysis was given by Collin [174].

4.3. Optical antennas

The anisotropic scattering of light by plasmonic nanoparticles has been intensively investigated over the last few decades. The dielectric function of the material of the particle, its size, shape, relative orientation comparing to the illumination field and the surrounding medium determine the angular spectrum of the scattered light. A simple dipole antenna based on sub-wavelength metal rod in homogeneous dielectric medium scatters light with toroidal angular dependence. This is the underlying mechanism of the optical antenna. If the supporting medium changes, or more particles of other size are placed close to the radiating dipole, the radiation pattern can be made more directional. One example of such antenna is the optical analogy of the classical Yagi-Uda antenna for radio waves. On the other hand, also the near-field is affected by the orientation of the electric field of the incoming light.

However, the sizes of the optical antenna cannot be tailored by scaling down the dimensions of the radio frequency antennas. Whereas metals for radio frequency antennas are almost perfect conducting, in the optical regime the surface plasmons matter and scaling laws are different. Novotny found a scaling law for small optical antenna and pointed out its differences comparing to the classical radio frequency antenna [91].

$$\lambda_{\text{eff}} = n_1 + n_2\lambda, \tag{23}$$

where n_1 and n_2 are constants dependent on the geometrical shape and material. The linear dependence of the optical resonances on the particle aspect ratio was verified for particles of spheroidal and rod shapes [93]. If a spheroidal particle has a diameter d and length L the multipolar resonance of order n reads [92, 93]

$$\lambda_n \simeq A_0 + A\frac{e}{n} \tag{24}$$

with $e = L/d$ and the constants A_0 and A being independent of the resonance number. We could confirm the scaling for silver spheroids embedded in a medium of refractive index $n = 1.45$ (see figure 2). The importance of the geometrical factor, the environment and the shape on the optical resonances has been intensively investigated and modelled using different calculation methods [47, 48, 71, 90, 175–178].

Some of first optical antennas were based on the radio frequency classical examples the dipole antenna and the Yagi-Uda antenna [179–186]. Yet, other shapes also proved to be efficient [187–190]. The main function of an optical antenna is to redirect the radiation pattern of an emitter located in its immediate neighbourhood. Hence, due to the near-field enhancement generated by the optical response of plasmonic material, the spontaneous emission decay rate is also modified by the Purcell effect. Thus, some optical antennas serve as cavities for radiative decay engineering as well [156, 164, 187, 188]. In order to quantify the Purcell effect of an antenna on an emitter it turns out very important to evaluate accurately its quality factor, but also the mode volume. Due to the open nature of plasmonic cavity the mode volume is difficult to calculate [156, 162, 191, 192]. Indeed, the quality factor of the plasmonic resonators is not very large and the main contribution to the Purcell enhancement comes from the tiny mode volume of the plasmons modes. More advanced designs of nanoantennas to enhance the Purcell factor, or to couple light to mechanical resonators include optical antenna-cavity coupling [190, 193, 194].

From the experimental point of view, the quality of plasmonic material used in a nanoantenna is of critical importance. The best optical antennas, but also the longest surface plasmon propagation length and the near-field confinement, are achieved with crystalline silver and gold particles [52, 195–199]. Nanoantennas and other nanostructures fabricated by lithography techniques usually have higher losses due to surface roughness, polycrystallinity [49, 51, 200] and additional absorption losses of the adhesion Cr, or Ti layers, required to hold the noble metal particles on the surface of dielectric substrates and commonly used in e-beam lithography [201].

Dark-field microscopy and spectroscopy can provide some information about the scattering properties of plasmonic particles [57, 84]. However, due to the illumination conditions the directivity cannot be measured. Since 2004, a new experimental imaging method has been used to characterise the angular distribution of the scattered light of an optical antenna: the back focal plane imaging [184, 186, 202–208]. The method consists in the introduction of additional lenses, in order to use the optical Fourier transform of the light at the back focal plane. The collected image in a CCD camera is that of the angular distribution of light scattered by the antenna. The collected light cannot have a larger in-plane k-vector than that allowed by the imaging objective. Several experimental setup for measuring the angular spectrum were proposed. Kurvits *et al* compared the different optical arrangements and their performance [208]. A related technique for the measurement of the orientation of fluorescent molecules using wide-field epifluorescence was demonstrated some years earlier [209].

The Fourier imaging using the back focal plane can be combined with spectroscopy in order to obtain a wavelength dependent angular spectrum of the scattered or emitted light. Thus, radiative modes associated with electric multipoles, or magnetic modes can be characterised by measuring the energy and momentum of light [186, 210]. Moreover, radiation patterns can also be measured using cathodeluminescence [182, 211–213]. In figure 17 radiation patterns generated by optical antennas of various shapes are presented. In figure 18 the radiation pattern of a gold ridge antenna, measured using cathodeluminescence, is presented.

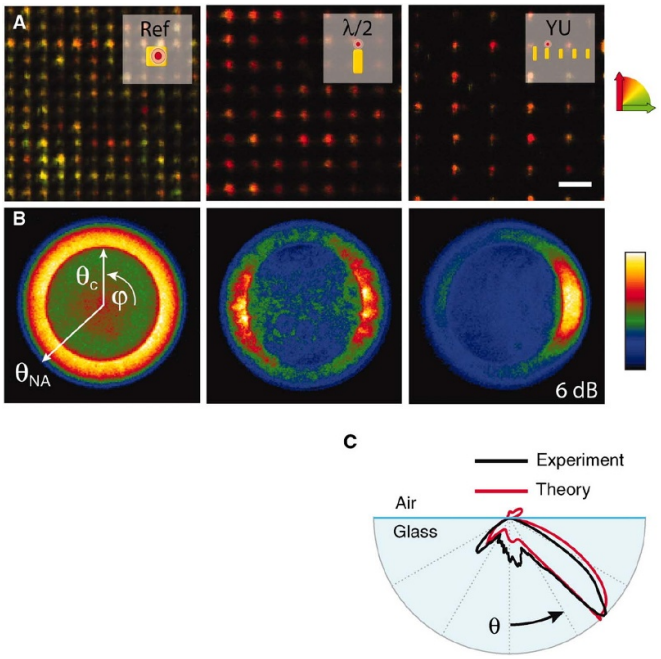

Figure 17. Unidirection emission of a quantum dot (QD) coupled with plasmonic nanostructures. (A) Confocal luminescence of a QD on top of a 60 nm gold square (top left image), $\lambda/2$ nanoantenna (middle) and Yagi-Uda antenna (right). (B) Respective angular distribution of the radiation intensity of the corresponding individual structures of (A). (C) Angular distribution of intensity in the polar angle of the Yagi-Uda antenna. From [179]. Reprinted with permission from AAAS.

Plasmonic antennas have been used not only in the manipulation of the angular spectrum of radiation, but also in fluorescence enhancement by Purcell effect and as transducers of electromagnetic radiation to mechanical vibration in optomechanical systems. This is illustrated in figure 19. The plasmonic dipolar antenna mounted on top of two silicon nitride nanobeams is responsible for the optical coupling with incoming radiation. It increases the scattering for adequate polarisation and due to its small gap induces optical forces and photothermal heat to the underlying beams. The result is a mechanical oscillation of the nanobeams. Optomechanics is fast evolving research field connecting the macroscopic classical world with the quantum mechanical [214–217]. Plasmonic nanoantennas can be used to improve the coupling of light beams with the acoustic vibrations of micro- and nanomechanical systems [144, 218–220].

4.4. Magnetic response and chirality in plasmonics

According to Landau and Lifshitz, the magnetic susceptibility of matter at optical wavelengths is negligible [221]. This contradicts experimental results of split-ring resonators and other micro- and nanostructures used in engineered metamaterials. The argument of Landau and Lifshitz does not apply for metamaterials where the characteristic length is of the order of

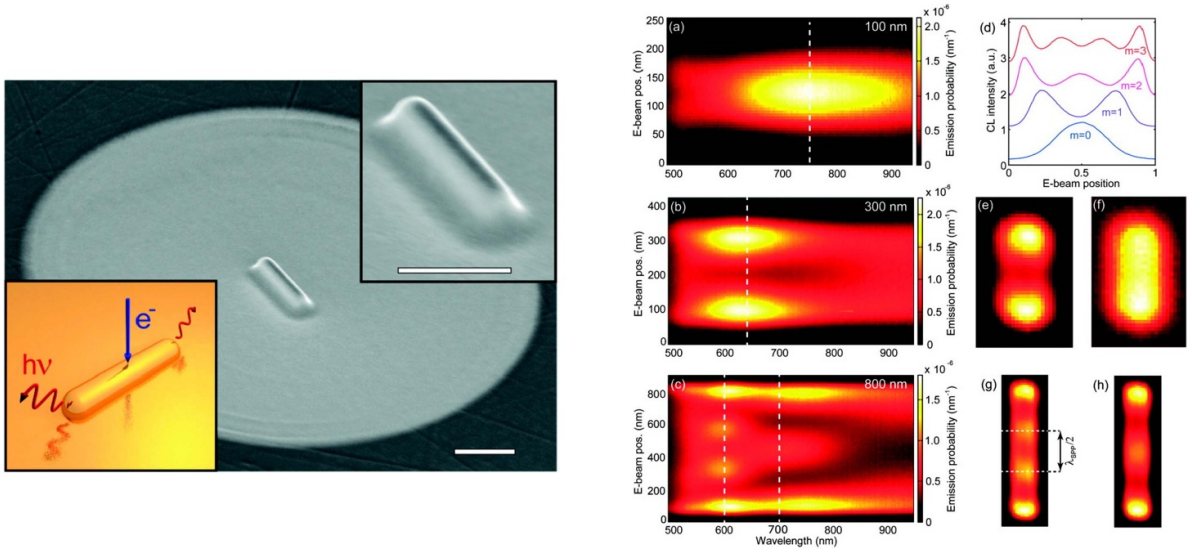

Figure 18. (Left) Scanning electron micrograph of a 700 nm long, 130 nm high, and 120 nm wide ridge antenna and schematic representation of the cathodeluminescence excitation. (Right) Experimental collected CL spectra as function of the electron beam excitation position for (a) 100 nm, (b) 300 nm and (c) 800 nm Au ridge antenna length. (d) Profiles of the intensity indicated by the dashed lines in (a)–(c). 2D excitation map of a 300 nm long antenna at (e) $\lambda = 650$ nm and (f) $\lambda = 950$ nm integrated over a bandwidth of 10 nm. 2D excitation maps of a 800 nm long antenna at (g) $\lambda = 600$ nm and (h) $\lambda = 700$ nm. Reprinted with permission from [212]. Copyright (2012) American Chemical Society.

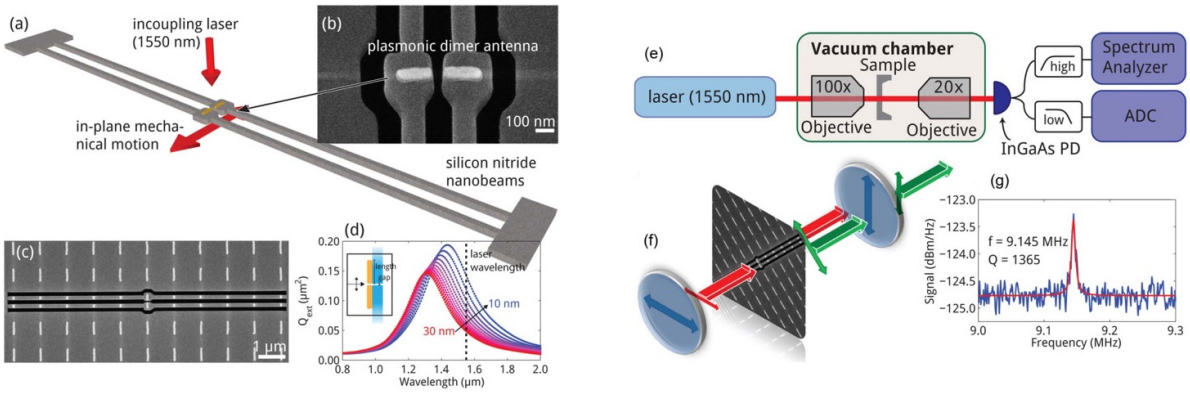

Figure 19. (Left) (a) Schematics of the experimental geometry. (b) SEM micrograph of the gold dipole antenna (225 nm× 50 nm× 40 nm) mounted in two nanobeam of silicon nitride (10.5 μm × 120 nm × 100 nm) with a gap of 30 nm. The nanoantennas were fabricated by electron beam, lithography as single rods and then tailored using focused ion beam. (c) SEM micrograph of the top view of tailored antenna. (d) Extinction spectra of a dipole antenna with two elements of 225 nm length as a function of the gap. The resonance of the antenna is centred approximately at the wavelength of the incident laser beam 1550 nm. Due to near-field coupling the antenna transmits a force and heat to the underlying silicon nitride nanobeams. (Right) (e) Schematics of the experimental setup. The vacuum system reaches 10^{-3} mbar. (f) Two polarisers in a crossed mount were used to reduce background signal of the transmitted light. The second polariser transmits the half of the scattered light by the antenna. (g) Spectrum of the thermal vibration of the plasmom antenna coupled with the mechanical system. Reprinted with permission from [190]. Copyright (2015) American Chemical Society.

the wavelength and are characterised by a plasmonic dielectric function [222]. Indeed, there have been found many examples of materials where the magnetic resonance is associated with a relevant magnetic moment. This includes the split-ring resonators [223–227] and arrays of near-field coupled spherical particles, or lithography designed nanostructures [228–230].

The discovery of negative effective magnetic permeability at optical wavelengths in split-ring resonators, extending the well known properties at radio frequencies, led to the development of metamaterials with negative refraction index. The negative refraction index and its effect in optics was an idea worked out by Veselago already in 1968 [231]. For that, both the electric permittivity and magnetic permeability should be negative. Pure plasmonic materials have a real part of the dielectric function that is negative at optical frequencies, but its magnetic permeability is close to unity. Thus, an effective negative permeability must be engineered. The demonstration of the first basic building unit showing both negative electric permittivity and magnetic permeability at microwave frequencies, was presented by Smith and collaborators in 2000 [232].

In the following year, the negative refraction was experimentally verified, using an engineered material based on arrays of resonant elements [233].

The extension of the negative refraction to optical wavelengths followed in more recent years [169, 170, 234–236]. The calculation of the effective permittivity ϵ_{eff} and permeability μ_{eff} of a metamaterial is usually based on the effective refractive index n and impedance Z. And these are obtained from measurement, or calculation of the S-parameters S_{11} (reflectance) and S_{21} (transmittance). Chen and collaborators developed a more general and robust method to obtain ϵ_{eff} and μ_{eff} [237]. The condition to achieve negative refraction is not so strict as before stated [238, 239]. The refractive index n is more generally defined by

$$n = n_1 + in_2 = \sqrt{(\epsilon_1\mu_1 - \epsilon_2\mu_2) + i(\epsilon_1\mu_2 + \epsilon_2\mu_1)} \qquad (25)$$

where $\tilde{\epsilon} = \epsilon_1 + i\epsilon_2$ and $\tilde{\mu} = \mu_1 + i\mu_2$. The real part of the refractive index n_1 is negative if $(\epsilon_1\mu_2 + \epsilon_2\mu_1) < 0$.

One concept related to the negative refraction is the perfect lens [240]. According to Pendry, a perfect image of an object could be achieved if a slab of a material of refractive index $n = -1$ would approach that object in near-field. This perfect lensing effect has been investigated by many researchers. It was demonstrated experimentally for a silver film in 2005 [241, 242]. However, the perfect lensing by a slab has been subject of some controversy [243].

The magnetic response of plasmonic materials has been engineered for other purposes as circular dichroism [244–246] and chiral response [223, 247–257]. Thorough theoretical analysis of the optical helicity, optical spin and other electromagnetic phenomena was published by Cameron *et al* [258] and by Nieto-Vesperinas [259].

The excitation of a magnetic resonance in slot antennas and its effect on the optical reflectance is depicted in figures 20 and 21. Plasmonic nanostructures made of small colloidal gold spheres connected by DNA strands (DNA origami) is presented in figure 22. The geometrical configuration of the gold particles forming an helix leads to circular dichroism.

Although the real part of the dielectric function of silicon and other dielectric materials of large refractive index is not plasmonic at optical wavelengths, spheres, cylinders and other particle shapes present very bright Mie resonances. Characteristic are magnetic and electric resonant modes presenting strong scattering [46, 261–264]. This is in contrast with the plasmonic Mie modes, which are predominantly electric. This fact has been used for the generation of light based on multipolar excitation [265, 266].

Many of the electric and magnetic resonances and their corresponding fields generated in sub-wavelength nanostructures have been incorporated in the fabrication of metasurfaces. An excellent review on plasmonic and photonic metasurfaces is given by Chen *et al* [267].

4.5. Toroidal electromagnetic modes in plasmonic materials

Textbooks on electrodynamics rarely treat other electromagnetic modes than electric and magnetic However, there is another class of multipoles, the toroidal multipoles [268, 269], discovered by Zel'dovich in the context of the parity violation in the electroweak interaction [270]. The interest of such electromagnetic modes of toroidal topology by the plasmonics community started around 2007 [271]. Since then, several structures supporting toroidal modes have been investigated [272–276]. One of the properties of such structures is the generation of the anapole (the term was coined by Zel'dovich for the static case). The anapole is the resulting electromagnetic modes where no radiation is emitted in a narrow bandwidth [275, 276]. It corresponds to the destructive interference by the superposition of a electric dipole and a toroidal dipole, both sharing the same radiation pattern [277–279]. The first experimental demonstration of a metamaterial presenting a dynamical anapole in the microwave regime, was in 2013, by Fedotov *et al* [280]. Anapoles have been investigated in in solid state physics, plasmonic and in dielectric particles [264, 272, 275, 281].

The toroidal dipole is characterised by a toroidal magnetic field or equivalently, poloidal current density flowing at the surface of a torus. The toroidal dipole moment points out perpendicular to the plane containing the torus and it is defined by [277]

$$\mathbf{T} = \frac{i\omega}{10}\int \left\{2\mathbf{r}^2\mathbf{P}(\mathbf{r}) - [\mathbf{r}\cdot\mathbf{P}(\mathbf{r})]\mathbf{r}\right\} d^3r, \qquad (26)$$

where $\mathbf{P}(\mathbf{r})$ is the induced polarisation. The induced polarisation current is given by $\mathbf{j} = -i\omega\mathbf{P}$. By other side the electric dipole and magnetic dipole moments are defined by

$$\mathbf{p} = \int \mathbf{P}(\mathbf{r})\, d^3r, \qquad \text{and} \qquad \mathbf{m} = -\frac{i\omega}{2}\int [\mathbf{r}\times\mathbf{P}(\mathbf{r})]\, d^3r \qquad (27)$$

respectively. When only an electric dipole and toroidal dipole are excited the far-field of the scattered radiation, expressed in Cartesian coordinates reads [264]

$$\mathbf{E}_{sca} \propto \frac{k^2}{4\pi\epsilon_0}\left[\mathbf{n}\times\mathbf{P}_{car}\times\mathbf{n} + ik\mathbf{n}\times\mathbf{T}_{car}\times\mathbf{n}\right]. \qquad (28)$$

Thus, for some wavelength when the magnitudes of both components equal in magnitude and are out of phase the far-field vanishes. Using the Mie theory the effect of the mode destructive interference was theoretically analysed. Anapoles were experimentally demonstrated for small particles of large refractive index (silicon) [264].

Figure 23 presents the excitation of an anapole in an array of circular cavities in a gold film. The COMSOL Multiphysics calculations show the spectral resonances of the cavities under plane wave p-polarisation at the vertical and an angle of 30°. At $\lambda = 715$ nm and incidence of 30° a narrow dip in the 0-order reflectance arises. This resonance is different from other resonances as for $\lambda = 650$ nm at vertical incident illumination. The reason for this resonance is not a light confinement in the cavity, but the excitation of a toroidal dipole combined with a electric dipole. The typical topology of the electric (radial) and magnetic (toroidal) fields are shown in figures 23(c) and (d) respectively. Similar results were found for circular cavities of smaller size in silver [273].

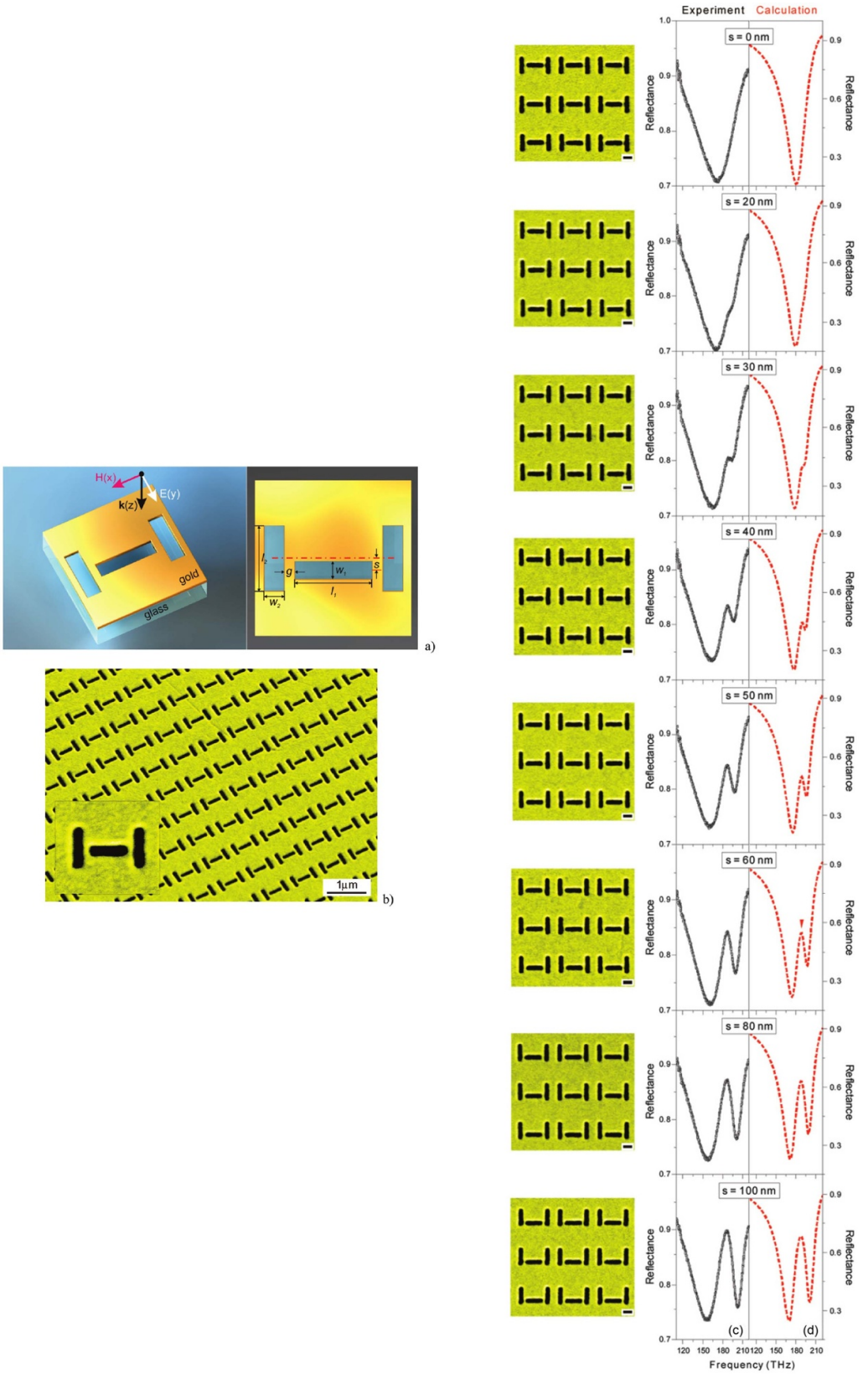

Figure 20. (Left) (a) Schematics of the structure fabricated in the gold film. Sizes of the geometrical parameters: $l_1 = 400$ nm, $w_1 = 80$ nm, $l_2 = 340$ nm, $w_2 = 90$ nm, $g = 45$ nm. Thickness of the gold film is 30 nm, on a glass substrate. The periods of the lattice in both the x- and y-direction are 800 nm. (b) Oblique view of the samples with a lateral displacement of $s = 20$ nm. (Right) (c) Experimental (black solid lines) and (d) calculated (red dashed lines) reflectance spectra as function of the lateral displacement s. The SEM images of the corresponding structure are shown at left. Reprinted with permission from [260]. Copyright (2010) American Chemical Society.

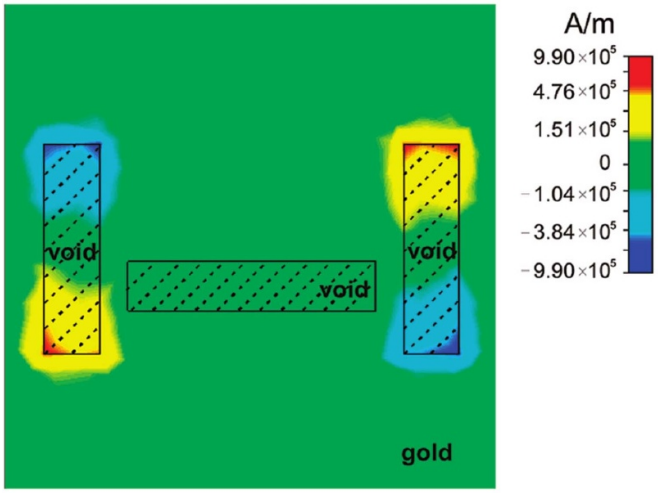

Figure 21. Distribution of the calculated magnetic field at the resonance (indicated by the red triangle for $s = 60$ nm in figure 20. The quadrupole antenna shows antisymmetric magnetic field distribution in the two slots. The magnetic field near the dipole antenna (middle slot) is very weak. Reprinted with permission from [260]. Copyright (2010) American Chemical Society.

4.6. Optical forces and thermal plasmonics

Plasmonic structures produce near-field gradients at the particle boundaries and between particles, which lead to mechanical effects on their neighbourhood. The mechanical effects due to the field gradients can be analysed using the Maxwell stress tensor. This tensor is the stress tensor of the electromagnetic field and is related to the Poynting vector and the momentum flux density [282]. The mechanical force exerted by the electromagnetic field on an object with finite boundary is given by the time-averaged surface integral of Maxwell stress tensor [80, 283].

$$\langle \mathbf{F}_{\text{mech}} \rangle_T = \oint_S \langle \overleftrightarrow{\mathbf{T}}(\mathbf{r},t) \rangle \cdot \mathbf{n}(\mathbf{r}) ds, \tag{29}$$

where $\langle \ldots \rangle_T$ denotes time averaging and $\mathbf{n}$ is a unit vector perpendicular to a closed surface S. Light can also carry angular momentum. In that case a torque is exerted on the particle [80, 284].

$$\langle \mathbf{N} \rangle_T = -\oint_S \langle \overleftrightarrow{\mathbf{T}}(\mathbf{r},t) \times \mathbf{n} \rangle \cdot \mathbf{n}(\mathbf{r}) ds. \tag{30}$$

The momentum contribution of the electromagnetic field disappears in the equation due to the time averaging. Thus, if the fields $\mathbf{E}$ and $\mathbf{B}$ are known in all points of space where a particle is located the time averaged mechanical force exerted on the particle by the fields. For a particle much smaller then the wavelength the Rayleigh approximation applies and the mechanical force on the particle exerted by a monochromatic field of angular frequency ω can be divided into a scattering component and the gradient force of the field [80, 285, 286]

$$\langle \mathbf{F}_{\text{mech}} \rangle_T = \frac{\alpha'}{2} \nabla \langle |\mathbf{E}|^2 \rangle + \omega \alpha'' \langle \mathbf{E} \times \mathbf{B} \rangle, \tag{31}$$

where $\alpha = \alpha' + i\alpha''$ is the polarisability of the particle. The first measurement of the mechanical force exerted by light, namely its radiation pressure, were done by Lebedev [287] and Nichols and Hull [288]. Ashkin showed how small suspension particles could be accelerated or trapped using focused laser light beams [289]. This is the fundamental mechanism of the later developed optical tweezers [286].

However, trapping of particles using plasmonics is not based on a strongly focused light beam, like in optical tweezers, but relies on the strong gradient fields near the plasmonic surfaces. Novotny estimated the trapping force on a small particle by a sharp tip under polarised light illumination [290]. Nieto-Vesperinas also studied theoretically optical forces and torques involving dielectric and plasmonic particles near surfaces [259, 291, 292]. More recently, the motion of dielectric particles trapped by an evanescent wave in dielectric materials was studied experimentally [293]. Volpe *et al* demonstrated experimentally how surface plasmons can trap polystyrene beads in water [294]. These results lead to experiments using nanostructured surfaces, instead of flat thin films [295–297]. The alignment and rotation of nanoparticles and nanowires on a surface was also achieved using polarised laser beams [293, 298]. The optical trapping and binding of plasmonic particles in a fluid is possible as for dielectric particles in optical tweezers, but the dielectric function of material is negative and the material has non-zero absorption, which leads to heat generation [290, 299, 300].

The heat generation by plasmonic particles in liquid environment under intense light fields was investigated by several groups [301–304]. The fact that plasmonic particles can be heated by laser light lead to their application in sensing, diagnostic and therapy of cancer cells [301, 305–307]. An example of photothermal heating by excitation of a plasmonic resonance in spherical gold particle in water is presented in figure 24. Small particles of gold are more adequate for photothermal heating than silver particles, due to their larger optical absorption at wavelengths shorter than 550 nm, and in some applications due to the biocompatibility of gold. The equation governing the heat diffusion generated by a source in a medium without phase transformation reads [308, 309]

$$\rho(\mathbf{r})\, c_p(\mathbf{r}) \frac{\partial T(\mathbf{r},t)}{\partial t} = \nabla \cdot [k(\mathbf{r}) \nabla T(\mathbf{r},t)] + q(\mathbf{r},t), \tag{32}$$

where $T(\mathbf{r},t)$ is the time-dependent spatial distribution of temperature, $\rho(\mathbf{r})$, $c(\mathbf{r})$ and $k(\mathbf{r})$ are the density, specific heat and thermal conductivity, respectively. The local heat source generated by light absorption is denoted by $q(\mathbf{r},t)$. Thus, for time-harmonic plane wave external light field $\mathbf{E}(\mathbf{r},t) = \Re\left[\tilde{\mathbf{E}}(\mathbf{r}) \exp(-i\omega t)\right]$ we obtain the photothermal heat by

$$q = \sigma_{abs} \frac{1}{2} n \epsilon_0 c |\mathbf{E}|^2. \tag{33}$$

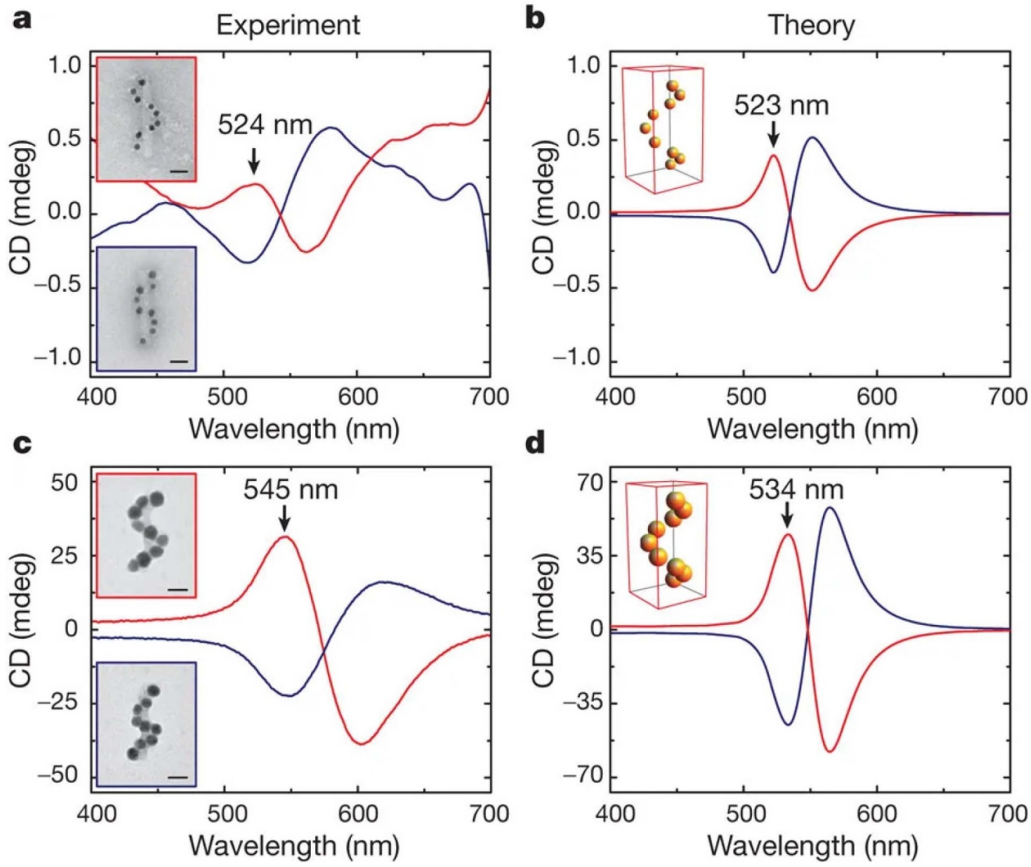

Figure 22. Chiral response of plasmonic DNA origami of gold nanoparticles arranged in helix. (a), (c) Experimental circular dichroism spectra (red for left-handed and blue for right-handed) of DNA origami helices with nine gold particles of 10 nm (a) and 16 nm (c). (b), (d) The calculated spectra of the circular dichroism for the particles sizes: 10 nm in (b) and 16 nm in (d). Reprinted by permission from Springer Nature Customer Service Centre GmbH: Nature [252] (2012).

More generally we can also evaluate the heat power using the induced current and the electric field inside the particle [304]

$$q = \frac{1}{2}\Re\left[\mathbf{J}^*(\mathbf{r})\cdot\mathbf{E}(\mathbf{r})\right] = \frac{\omega}{2}\Im[\epsilon(\omega)]\epsilon_0|\mathbf{E}|^2. \tag{34}$$

In the steady-state the maximum temperature increase in water surrounding a sphere of radius R is given by [303]

$$\Delta T = \frac{P}{4\pi k_w R}, \tag{35}$$

where P is the absorbed power by the sphere and k_w is the thermal conductivity of water. For non-spherical particles a geometry dependent effective radius substitutes R in the expression [303].

Under strong laser pulses, not only fast temperature rising, but also acoustic vibrations can be induced in plasmonic particles [310, 311]. Depending on the normal modes of the particles, the spectral range of resonances lies between GHz and THz [312].

4.7. Quantum nature and quantum effects of plasmons

When in some extreme cases the classical theory fails quantum treatment of plasmons is recommended. However, the majority of phenomena related to the light interaction to plasmonic particles can be understood using classical electrodynamics. The optical properties of very small noble metal particles, or particle pairs of very small gaps, cannot be described reliably by the interaction of light with a local dielectric function and a semi-classical or pure quantum description of the interaction is required [61, 313–315]. In other cases a modification of the dielectric function from local to non-local is necessary for accounting the interaction effects [62, 63, 316–318].

The interaction of plasmonic particles with single emitters requires often a quantum treatment, either for light scattering [219, 315, 319, 320], involving absorption and emission [114, 162, 163, 321, 322], or tunnelling [323]. The quantum nature of surface plasmons has also investigated experimentally [320, 324–326] and theoretically [161, 327, 328].

4.8. Nonlinear plasmonics

At low field intensities all effects involving plasmonic excitations are linear. This is due to the small value of the second order electrical susceptibility $\xi^{(2)}$. The generalised polarisation reads [329]

$$\mathbf{P}(\mathbf{r},t) = \epsilon_0[\xi^{(1)}\mathbf{E}(\mathbf{r},t) + \xi^{(2)}\mathbf{E}(\mathbf{r},t)\mathbf{E}(\mathbf{r},t) + \xi^{(3)}\mathbf{E}(\mathbf{r},t)\mathbf{E}(\mathbf{r},t)\mathbf{E}(\mathbf{r},t) + \ldots] \tag{36}$$

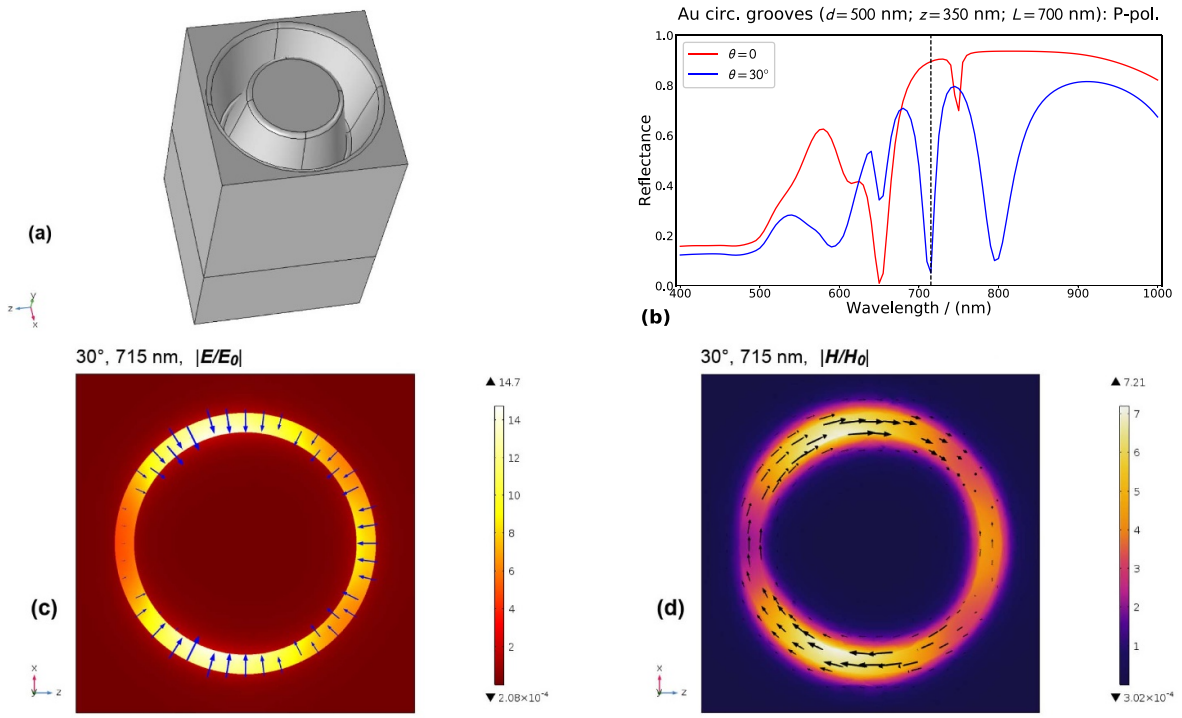

Figure 23. Excitation of a toroidal dipole in an array of circular cavities with V-shape profile in gold. (a) Geometrical representation of the unit cell containing a single ring cavity for simulation using COMSOL Multiphysics. The lattice constant in both directions is 700 nm. The mean cavity diameter is 500 nm. The depth of the groove 350 nm and the width at the surface 140 nm. The excitation plane wave is either incident from top to bottom (normal), or at 30° to the normal. (b) Reflectance spectra for vertical and 30° incidence and p-polarisation. The vertical black dashed line indicates the position of the anapole. (c) Normalised electric field ($\lambda = 715$ nm) and field direction at the plane $z = -250$ nm below the metal surface. (d) Normalised magnetic field ($\lambda = 715$ nm) and its direction at the same plane. The radial distribution of electric field and the toroidal distribution of the magnetic field in the cavity for $\theta = 30^{\circ}$ and $\lambda = 715$ nm are associated with an anapole and provoking a pronounced reduction of reflectance.

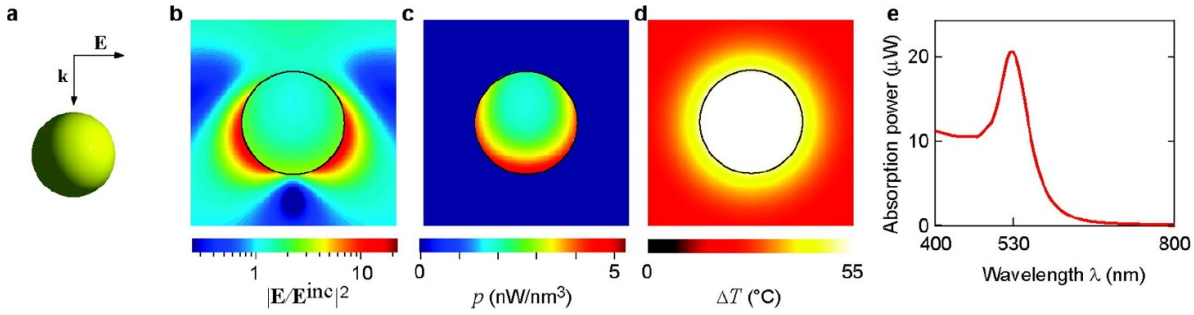

Figure 24. Photothermal heating of a plasmonic 100 nm gold sphere in water. (a) Direction of the illumination and field polarisation. (b) Electric field enhancement map. (d) Distribution of the thermal power in the plasmonic particle. (d) Distribution of increase of temperature at thermal equilibrium, for $\lambda = 530$ nm. (d) Absorption power as function of the wavelength. The incident power intensity is 1 $\mu W/\mu m^2$. Reprinted with permission from [303]. Copyright (2010) American Chemical Society.

or expressing each component of the polarisation

$$P_i = \epsilon_0 \left(\sum_j \xi_{ij}^{(1)} E_j + \sum_{j,k} \xi_{ijk}^{(2)} E_j E_k + \sum_{j,k,l} \xi_{ijkl}^{(3)} E_j E_k E_m + \ldots \right). \tag{37}$$

$\xi^{(i)}$ is the non-linear susceptibility tensor or order i. For example the wave mixing (WM), including the sum and difference of frequencies and the optical parametric oscillation processes, depend on the second harmonic generation are associated with $\xi^{(2)}$, the Kerr effect and third harmonic generation depend on $\xi^{(3)}$.

However, non-linear effects in plasmonic materials have been predicted and measured for both metal surfaces and metal nanostructures of several geometrical configurations. A short list includes, bare metal surfaces and films [330, 331], sharp tips [332], tapered plasmonic waveguides [333], optical rods and nanoantennas [334–336], in graphene plasmons [327, 337, 338], in gratings [339, 340] and in other geometrical arrangements of plasmonic particles [78, 341–343], including metamaterials and metasurfaces [344–347]. The main limitations of non-linear optical generation using plasmonic nanostructures are the small bulk non-linear susceptibilities of the metals, which are compensated by the strong near-field at

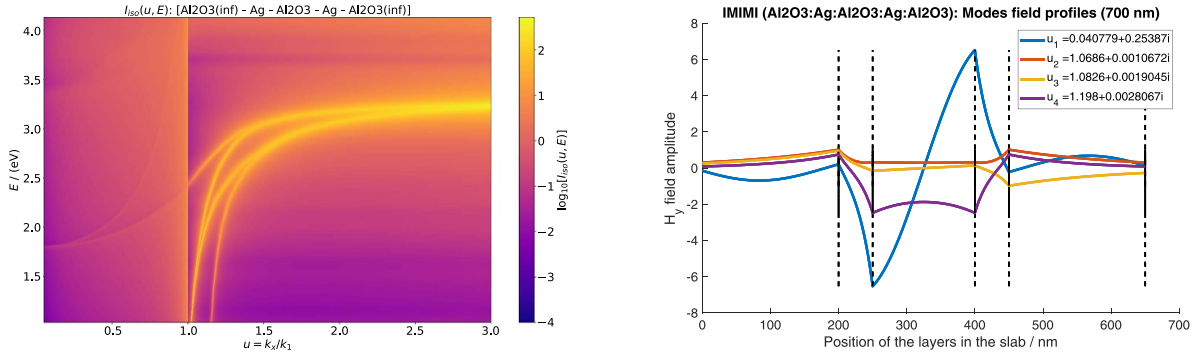

Figure 25. (Left) Dispersion relation for a IMIMI structure made of two 50 nm silver films separated by a 150 nm thick aluminium oxide layer. The structure in embedded in aluminium oxide. The map presents the power density dissipated by an isotropic point dipole located 10 nm distant from the first silver layer. The bright yellow regions correspond to the guided modes. An hybridisation occurs between the symmetric and antisymmetric plasmon modes of the silver film and the TM mode of the Fabry–Perot cavity formed by the two silver layers, leading to four plasmon modes. The k-vector was normalised by the k-vector of the first medium, k_1. The vertical line $u = 1$ corresponds to the light line for the first medium. Propagating waves have $u < 1.0$, whereas guided waves are in the region $u > 1.0$. The cavity mode at the left not crossing the light line is the TE mode. The calculation relies on the theory of Ford and Weber [43] and Barnes [376]. (Right) H_y field profiles of the Fabry–Perot and guided plasmonic modes in the structure for $\lambda = 700$ nm. The blue curve corresponds to a Fabry–Perot excited for a plane wave of small in-plane k-vector. The other three modes are guided plasmon modes labelled with increasing normalised k-vector u_i . The field profiles were done using the program Moosh [377], based on scattering-matrix calculations.

the plasmonic resonance, and the low damage threshold due to the unavoidable optical absorption of the metal.

5. Advanced applications of plasmonic resonators

In the previous sections we reviewed the application of plasmonic resonators distinguishing their interaction with radiation and matter by the physical mechanism. In the last 5 years new applications have been presented using plasmonic resonances as building blocks for more sophisticated matter-radiation interactions, only achieved in hierarchically engineered materials. This includes, metamaterials, topological materials, interaction of electrons and plasmons and fast nanoscale switching using plasmonic systems.

5.1. Plasmonic metamaterials

A metamaterial is an engineered material presenting properties not available in bulk materials of nature. This definition is not entirely correct and been revised, because many materials have been found in nature, either layered minerals, or resulting from the organic-inorganic growth processes leading to very complex optical, thermal and mechanical properties [348]. In this category belong biominerals and periodic and quasi-periodic organic structures of many living beings, as coloured feathers of birds, fish skin, chromatic, refringent and diffractive properties in the outer surface of many insect species. Plasmonic metamaterials are indeed a subset of metamaterials, not found in nature, due to the incorporation of noble metal elementary structures, or 2D materials.

The advent of plasmonic metamaterials began with the pioneering works of Pendry [240] and Smith [232], in 2000. Their achievement was the demonstration of the negative refraction, already theoretically postulated by Veselago [231], in 1968. Negative refraction requires in first approach a composite material presenting simultaneous negative dielectric permittivity and magnetic permeability. Plasmonic materials have negative real part of the permittivity, so the magnetic negative permeability, not found in bulk had to be engineered. At the same time optical effects as invisibility cloaking and transformation optics started to be investigated very actively [38, 349–351], as well as ε near-zero materials [79, 352, 353].

In the visible spectrum the experimental realisation of negative refraction is difficult to achieve, mainly due to the optical losses and tiny size of the nanostructures, but other effects attracted both the plasmonic and the electrical engineering community. Among them the hyperbolic metamaterials [354]. Bulk materials with isotropic electric permittivity have an optical propagation with the same wavelength in all space directions. Anisotropic materials as quartz and calcite have ellipsoidal dispersion because their isofrequency surfaces have ellipsoidal shape. The dispersion relation of an uniaxial medium, where the optical axis is parallel to the z-axis and two components of the permittivity tensor are equal, $\epsilon_{xx} = \epsilon_{yy}\epsilon_{\perp}$, where $k_0 = \omega/c$ and $k_{\perp} = \sqrt{k_x^2 + k_y^2}$, reads [355]

$$\left(k_{\perp}^2 + k_z^2 - \epsilon_{\perp} k_0^2\right)\left(k_{\perp}^2/\epsilon_{zz} + k_z^2/\epsilon_{\perp} - k_0^2\right) = 0. \qquad (38)$$

The first term in the equation above corresponds to spherical surface for a fixed frequency (isofrequency surface) and the second to a ellipsoidal surface in the k-space. However, when one of the components of the permittivity tensor, either $\epsilon_{\perp}$, or ε_{zz} has a negative value the surfaces of isofrequency of the dispersion equation become hyperbolic. On of the consequences of the hyperbolic dispersion is that plane waves of very large k-vector, corresponding to evanescent waves can propagate in the uniaxial medium, whereas they cannot propagate in isotropic media. For $\epsilon_{\perp} > 0$ and $\epsilon_{zz} < 0$ the isofrequency solutions are double hyperboloid surfaces mirrored against the XY-plane and the hyperbolic material is called *dielectric*, or *type I*. In the contrary case ($\epsilon_{\perp} < 0$ and $\varepsilon_{zz} > 0$)

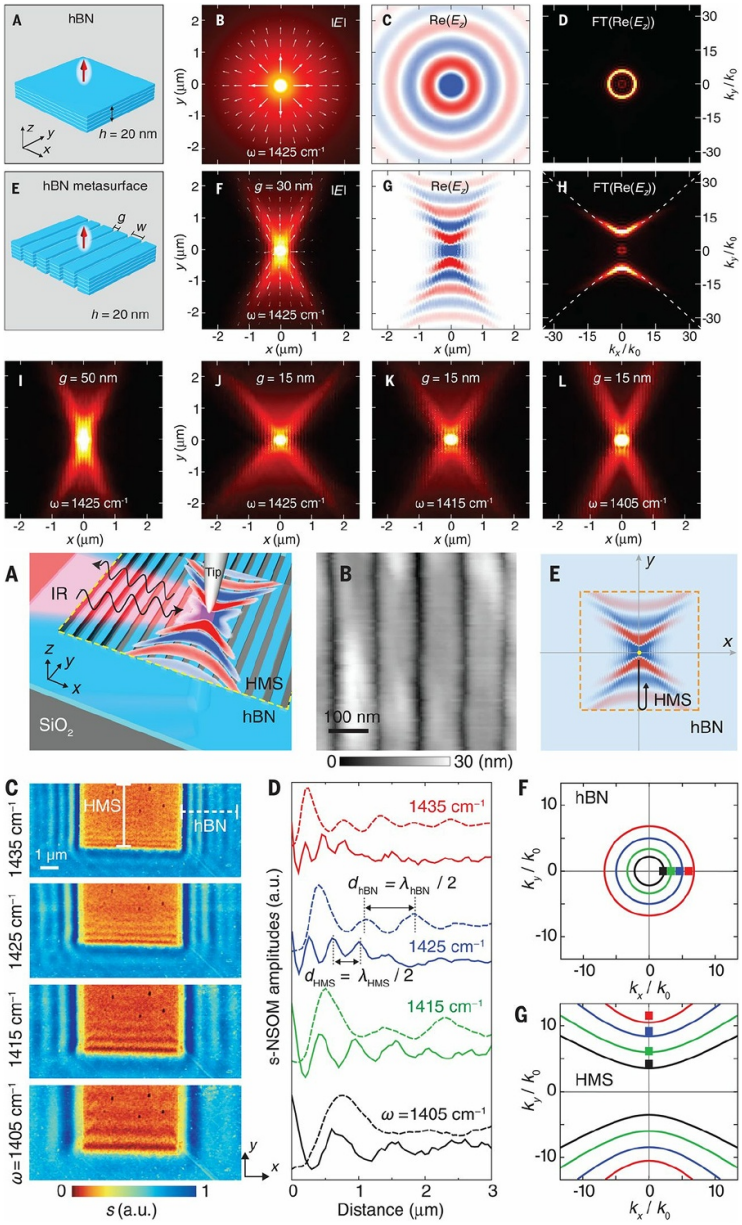

Figure 26. (Top) (A) Schematic of dipole launching of phonon polaritons on a 20 nm thick hBN flake. h, height. (B) Simulated magnitude of the near-field distribution above the hBN flake, $|E|$. (C) Simulated real part of the near-field distribution above the hBN flake, $\Re(E_z)$. (D) Absolute value of the Fourier transform (FT) of (C). k_x and k_y are normalized to the photon wave vector k_0. (E) Schematic of dipole launching of phonon polaritons on a 20 nm thick hBN HMS (ribbon width $w = 70$ nm; gap width $g = 30$ nm). (F) Simulated magnitude of the near-field distribution above the hBN HMS, $|E|$. (G) Simulated real part of the near-field distribution above the hBN HMS, $\Re(E_z)$. (H) Absolute value of the FT of (G). The features revealed by the FT of the dipole-launched polaritons can be well fitted by a hyperbolic curve (white dashed lines). (I)–(L) Simulated magnitude of the near-field distributions for HMSs with different gap sizes and operation frequencies. The grating period $w + g$ is fixed to 100 nm in all simulations. The white arrows in (B) and (F) display the simulated power flow. (Bottom) (A) Schematic of the near-field polariton interferometry experiment. IR, infrared. (B) Topography image of the hBN HMS (nominal grating parameters are $w \approx 75$ nm and $g \approx 25$ nm; see also figure S4 of the supplementary materials of [375]). (C) Near-field images (amplitude signal s) recorded at four different frequencies. a.u., arbitrary units. (D) s-NSOM amplitude profiles along the solid (vertical) and dashed (horizontal) white lines in (C). (E) Illustration of the polariton interferometry contrast mechanism. The tip launches phonon polaritons on the HMS (indicated by simulated near fields). The polaritons with wave vector parallel to the grating reflect at the lower horizontal boundary (indicated by the black arrow) and interfere with the local field underneath the tip. Tip-launched polaritons propagating in other directions cannot be probed by the tip. The orange dashed lines mark the boundaries of the HMS. (F), (G) Experimental (squares) and numerically calculated (solid lines) wave vectors of phonon polaritons on the unpatterned flake and the HMS, respectively. The line colors indicate the frequency ω according to (D). From [375]. Reprinted with permission from AAAS.

the isofrequency surfaces form hyperboloids along the k_z-axis and the hyperbolic medium is called *metallic*, or *type II*. Several artificial materials based on plasmonic elements have been proposed to achieve effective hyperbolic properties. The most common are the multilayer MIM based materials and the arrays of plasmonic rods embedded in a dielectric. In the

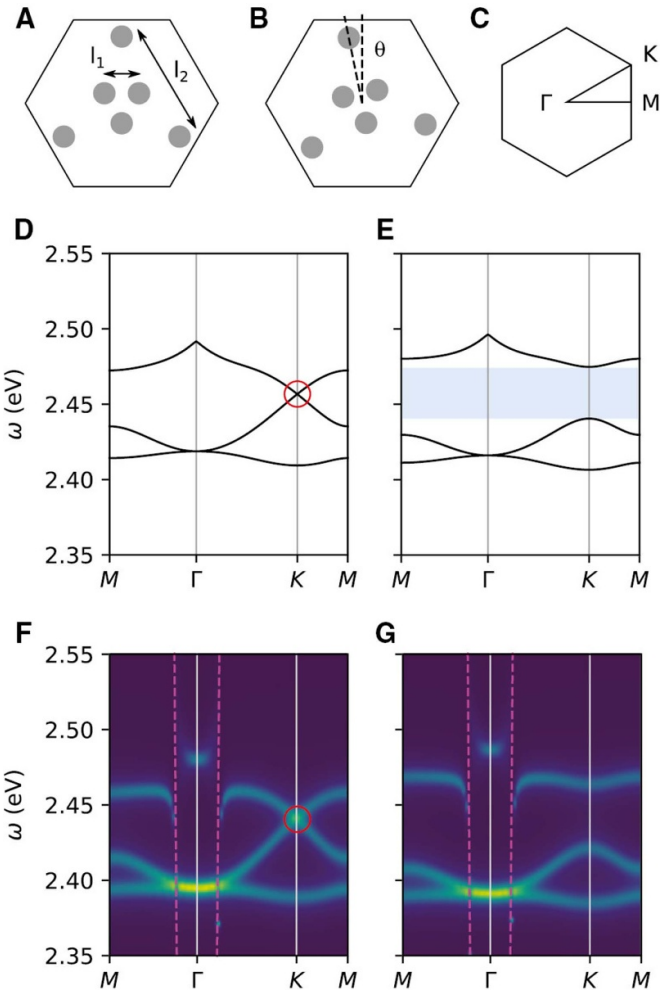

Figure 27. (A) Unit cell with NP radius $r = 5$ nm and height $h = 30$ nm, internal spacing $l_1 = 10\sqrt{3}$ nm, external spacing $l_2 = 30\sqrt{3}$ nm, and lattice constant $a_0 = 75$ nm. (B) A $\theta = 0.1$ rad rotation removes σ_v. (C) BZ. (D) Band structure, pre-perturbation. (E) Post-perturbation. (F), (G) Spectral function: higher-energy bands experience polariton-like splitting at the light line (magenta). Drude losses $\gamma = 10$ meV. Reproduced from [405]. CC BY 4.0.

limit of very high density many very narrow layers, or small rod separation and diameter comparing to the wavelength, homogenisation can be achieved leading to effective hyperbolic properties. The most common homogenisation schemes of the uniaxial dielectric function is by an effective medium theory, e.g. using the Maxwell–Garnett and Bruggeman formulas for bi-isotropic media [356, 357], or by the Rytov method [358].

Due to the propagation properties of hyperbolic materials plasmons can be excited and propagate in volume and permit a series of novel effects as, long range dipole-dipole interactions as in Förster resonance energy transfer (FRET) [359], super-Planckian thermal radiation emission in near-field [360, 361], strong coupling [362], broadband Purcell effect [363] and its application in enhanced spontaneous emission and light extraction [364].

Figure 25 presents the dispersion and the field profiles of several guided plasmonic modes along a stack of silver films of 50 nm thickness separated by a 150 nm aluminium oxide layer. The outer regions (substrate and cover) are also alumina. The number of plasmonic modes is identical to the number of dielectric-metal interfaces. By replication of the number of bi-layers aluminium oxide-silver the number of plasmon modes increases and the dispersion curves move toward higher k-wavenumber. Thus, a very large number of bi-layers of narrow thickness leads to plasmons with very large k-vavenumber, a characteristic of the hyperbolic metamaterial.

Another class of materials were plasmonic nanostructures have been widely used to manipulate the propagation properties of light beams are metasurfaces. Metasurfaces are two-dimensional arrangements or arrays of meta-atoms, as dielectric nanoparticles or plasmonic nanoantennas, which collectively can achieve a modification of the light properties, as in flat lensing [365, 366], generation, conversion and detection of the angular momentum topological charge [367–370], holography [371, 372] and polarimetry [373].

Metasurfaces can be designed to support hyperbolic propagation [374, 375]. In figure 26 an example of metasurface based on nanostructured hexagonal boron nitride (hBN) showing hyperbolic propagation at middle-IR wavelengths is presented.

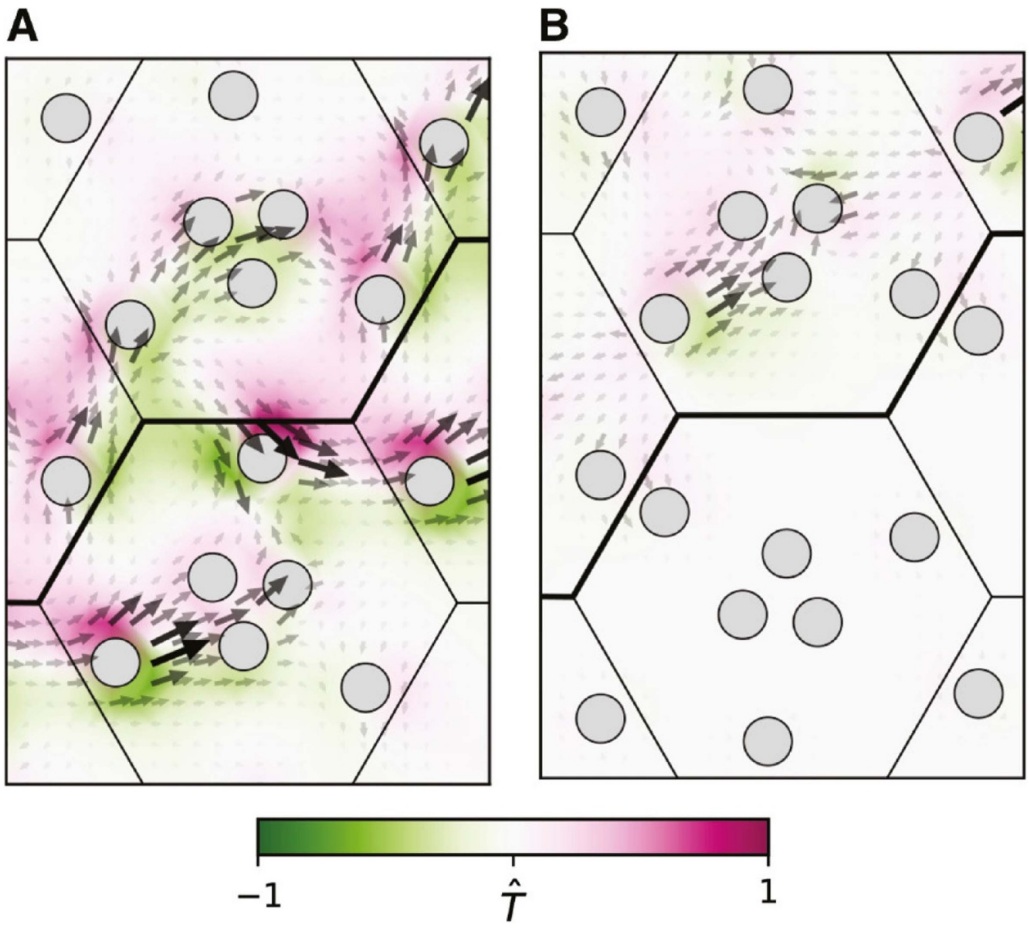

Figure 28. Chirality comparison: Poynting vector **S** (arrows) and normalized spin angular momentum (colour) $\hat{T}_z$. (A) Nontrivial edge mode on C_{3v}, type I edge. (B) Trivial edge mode on C_{3v}, type III edge: energy flow is more linear, as seen in the small spin angular momentum amplitude. Reproduced from [405]. CC BY 4.0.

5.2. Plasmonic materials with topological properties

Topological insulators are a novel and very special class of electronic materials presenting insulator behaviour in bulk and conduction at the boundaries [378]. The conduction at the boundary is however robust, as its properties remain unperturbed by defects and disorder. The bulk material has a band structure presenting a gap like between the highest occupied band and the lowest empty band. The surfaces (or edges in 2D) of the material have gapless states which are protected by time-reversal symmetry. An example of 2D topological insulator is the quantum spin Hall insulator and also related to the integer quantum Hall effect [379].

The success obtained with topological insulators in electronic materials led to a pursuit towards photonic materials presenting similar topological properties, despite the nature of photons being bosonic instead of fermionic [380–382]. Both dielectric and plasmonic materials have been found to possess topological properties due to the optics of evanescent waves. Bliokh *et al* have shown that spin and momentum of light in evanescent waves may have geometrical and topological properties completely different than in propagating waves [383]. Moreover, for certain plasmonic nanostructures in surfaces spin–orbit coupling and its unusual light propagation is achieved [384]. Indeed, the spin–orbit coupling is an essential element of the topological materials. Thus, the search for new topological photonic materials relies on optical properties as chirality and Dirac states of light, and photonic structures mimicking the band structure of topological insulators have been investigated [385, 386].

Plasmonics enters the realm of topological materials by several ways. It was found by Markel [387] and Zou *et al* [388] that arrays of nanospheres can produce remarkably sharp resonances, despite their individual extinction spectra being broad. This study was extended to different lattices of gold disks and coupled particles by Auguié, Humphrey and Barnes and others [389–392]. The near-field coupling between particles and the diffraction in the array leads to lattice plasmon modes distinct from those observed in individual particles. The lattice plasmon modes are responsible for new near-field distributions. Symmetries and a band structure that resembles that of graphene were found for the hexagonal lattice of silver nanoparticles at the Γ point [385, 393]. Several lattices and particle shape have been investigated in lasing, strong coupling, Fano resonances and sensing applications [394–398]. More recently, the use of particle arrays in the investigation of topological effects of light has been pursued [399, 400].

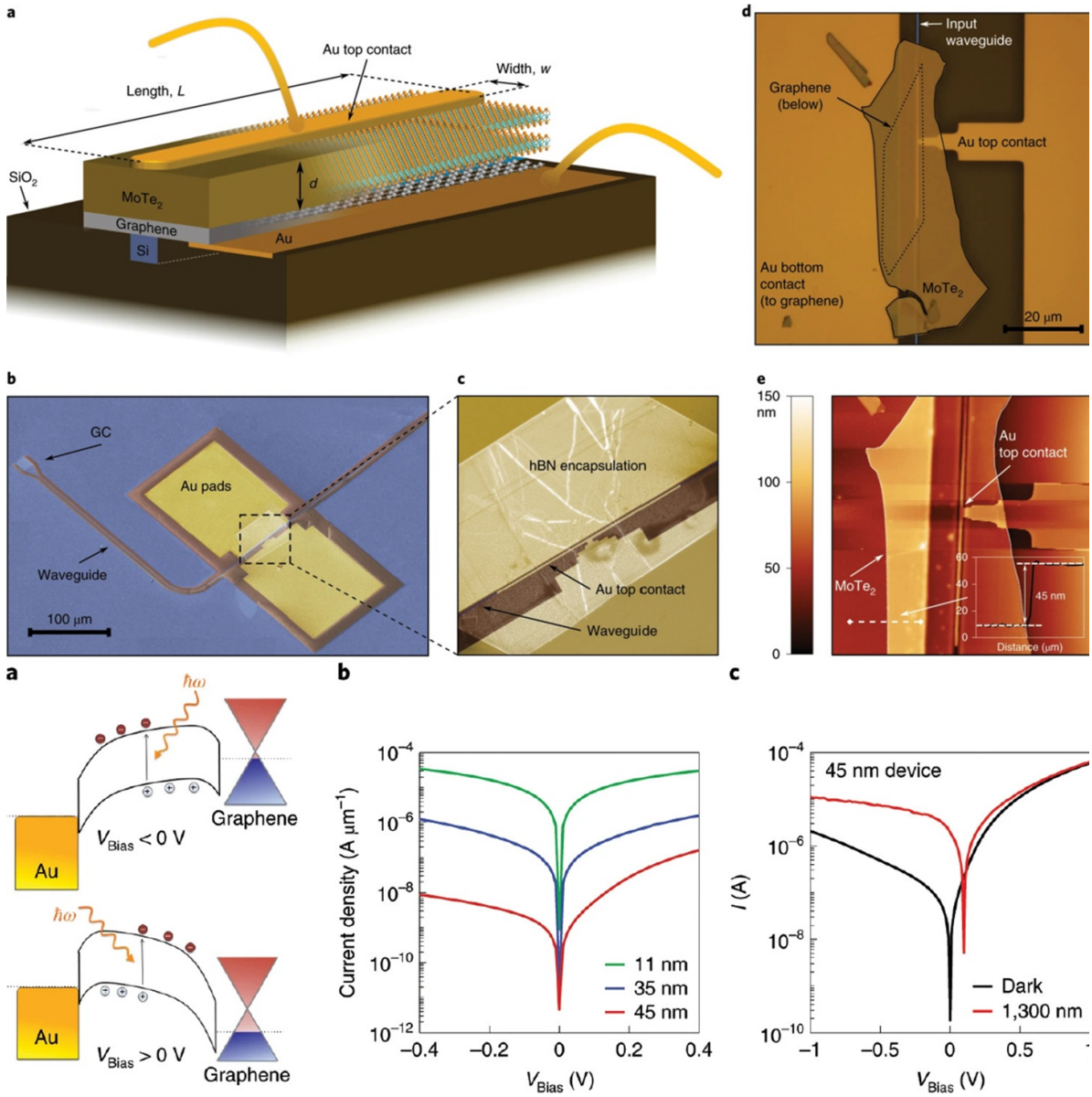

Figure 29. (Top) (a) Schematic illustration of a vertical $MoTe_2$-graphene heterostructure detector coupled to a silicon waveguide buried in SiO_2 claddings. Graphene and $MoTe_2$ are connected to gold (Au) bottom and top contacts, respectively. (b) False-colour SEM image of a fabricated device, showing the silicon waveguide and grating coupler (GC) (both in blue), the waveguide oxide lateral claddings (brown), the metallic structures (gold), and the encapsulation hBN layer (in semi-transparent white). Scale bar, 100 μm. (c) Enlarged-view SEM image of the fabricated detector. (d) Optical micrograph picture of a fabricated waveguide detector before encapsulation with hBN. It shows the graphene flake, the $MoTe_2$ flake, the optical waveguide and metallic structures, including the contact electrode on top of the $MoTe_2$, used for carrier extraction. Scale bar, 20 μm. (e) AFM image of the fabricated detector, showing the $MoTe_2$ flake and the metallic contact bar on top of the $MoTe_2$ flake and the planar waveguide. (Inset) A cross-sectional line scan indicating a $MoTe_2$ thickness of 45 nm. (Bottom) (a) Schematic illustration of the band diagrams of the vertical $MoTe_2$-graphene heterostructure under negative bias (upper diagram) and positive bias (lower diagram), respectively. (b) Dependence of the current density on bias voltage on a logarithmic scale for several devices with different $MoTe_2$ channel thicknesses (red line, 45 nm; blue line, 35 nm; green line, 11 nm). The current density is obtained by normalizing the current to the length of each device. (c) $I - V$ curves without (black curve) and with (red curve) 1,300 nm light coupled to a detector featuring a 45-nm-thick $MoTe_2$ flake. Reprinted by permission from Springer Nature Customer Service Centre GmbH: Nature Nanotechnology [424] (2012).

By other side, graphene is a Dirac material which presents not only topological properties for electrons but can also be tailored for photonic applications presenting topological properties [401, 402]. Other 2D materials as transition metal dichalcogenide monolayers were also used for investigation of the spin–orbit coupling of light and its effect on the light propagation direction [403]. It was found that arrays of metallic nanoparticles arranged in hexagonal lattice can be used for engineering edge states [404]. This lattice is the same of graphene and thus, some eatures found for edge states of graphene can be expored in arrays of plasmonic particles.

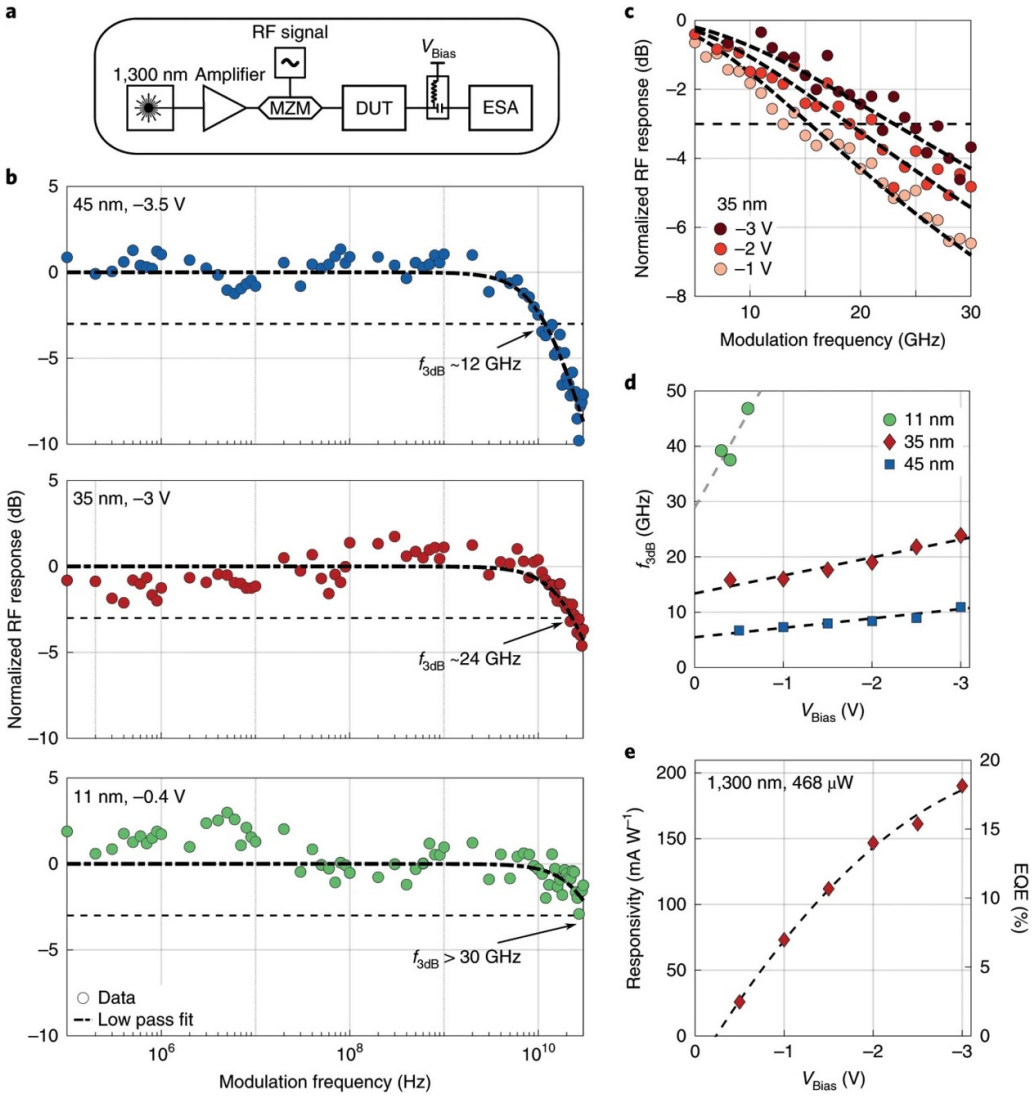

Figure 30. (a) Frequency response measurement setup. Mach-Zehnder modulator (MZM); device under test (DUT); electrical spectrum analyser (ESA). (b) Normalized radio-frequency (RF) signal response as a function of the modulation frequency of the input signal for three devices. A single pole low-pass filter is used to fit the data points and to extract the 3 dB roll-off frequency $f_{3\ \mathrm{dB}}$ for each device. The thicknesses of the $MoTe_2$ flakes and the applied bias voltages are indicated in the figures. (c) Frequency response of the 35 nm thick $MoTe_2$ device for different bias voltages. (d) Dependence of the roll-off frequency $f_{3\ \mathrm{dB}}$ on the applied bias voltage and for different $MoTe_2$ flake thicknesses (blue scatters, 45 nm; red rhombuses, 35 nm; green dots, 11 nm). The linear trend indicates that the bandwidth is transit time limited. (e) Simultaneously measured responsivity and the corresponding EQE as a function of the applied bias voltage for input light at 1300 nm with power intensity of 468 μW. Reprinted by permission from Springer Nature Customer Service Centre GmbH: Nature Nanotechnology [424] (2020).

Topological metasurfaces allow a precise control of light propagation at certain edges. The design of edge states in arrays of nanoparticles in a surface are an example of potential topological metasurface for manipulation of the spin of light along the metasurface [405]. Figure 27 presents examples of metasurfaces based on arrays of metal nanoparticles and show how their edge states in the band structure be be modified by a symmetry breaking produced by the rotation of the array in the unit cell. This change in the edge state leads to a special light propagation at the boundary between two regions with different Brillouin zones, shown in figure 28. It should be stressed that different edge types lead to the different propagation properties. The edge between two lattices shown in figure 28(A) allows momentum flow (Poynting vector) and normalised spin angular momentum ($\hat{T}_z$) in a complex way near the edge, whereas in (B), where the lower lattice is the mirror symmetry of the upper lattice, the flow is more linear.

5.3. *New materials for electron-plasmon interaction*

The discovery of surface plasmons is intimately related to electron beams [2], as it is the electron energy loss of electrons beams that produce the collective surface excitations called surface plasmons. However, it was found few years earlier in 1953, that non-relativistic electrons moving parallel to the surface and perpendicular to the grooves of a metal grating lead to emission of electromagnetic radiation at optical wavelengths,

by a mechanism similar to Cherenkov radiation, the so called Smith–Purcell effect [406]. This phenomenon was later very intensively investigated in the field of electron accelerators and free electron lasers. More recently, due to its connection with surface plasmons in metal gratings and other periodic nanostructures, it was again investigated by the plasmonics community [407–411]. On the other hand, the interaction between electrons and plasmons underlies physical mechanisms used in several microscopy and spectroscopy techniques as electron energy loss spectroscospy (EELS), photoemission electron microscopy (PEEM) and cathodeluminescence (CL) [60, 412, 413]. EELS and cathodeluminescence are based on the direct interaction of electron beams with the plasmonic material. In the first a mapping of the beam energy loss is reconstructed in the plasmonic structure. In cathodeluminescence, the light emitted from the interaction of an electron beam with a nanostructure is used to obtain the angular spectrum and the energy spectrum of the plasmonic resonance. In PEEM, a pulsed laser beam generates electron emission mediated by the plasmonic excitation.

A second connection between surface plasmons and electrons arises in the fast emission of photo-electrons and non-linear light pulses, by excitation of surface plasmons in a grating nanofabricated in a sharp metal tip [414, 415]. In order to produce a strong near-field at the tip appex, the nanostructured grating is excited by femtosecond laser pulses, which leads to highly confined light and coherent pulsed emission of photons or electrons. Sharp tips under illumination of low power fs laser pulses produce high harmonic light emission, mediated by non-linear processes of the confined plasmons [416]. In parallel to light emission, illuminated but non-nanostructured tips can also be used as fs electron sources by photoinduced field emission [417]. These effects have triggered new research, combining highly non-linear photonics, ultra dynamics using fast pulsed electron sources, coherent spectroscopy and microscopy [418–420].

The third connection between electrons and plasmons arises in light emission by inelastic electron tunneling in junctions [421]. Light emission by inelastic electron tunneling has been reanalysed from the perspective of plasmonics [422], but its applications go beyond a pure side effect of tunneling. Tunneling is a very fast phenomenon and the control of tunnel currents by excitation of surface plasmons has a very high impact in fast switching and modulation devices [220, 423] and high speed photodetection [424]. In figure 29 a high speed photodetector based on graphene and two-dimensional transition-metal dichalcogenides (TMDCs) is presented, as is an $MoTe_2$ sandwiched between gold contacts. Efficient photoresponse at frequencies up to 30 GHz were demonstrated experimentally (figure 30). Devices based either on plasmonic elements as gold, or 2D materials as graphene and two-dimensional transition-metal dichalcogenides, due to their electronic properties, allow for fast transducion mediated by tunneling [323, 425–427].

These examples demonstrate the importance of plasmonic systems in the new physics and new technological applications. Although many other applications could be listed, in sensing, energy harvesting and in nanolithography, these examples provide a perspective of the exceptional potential of plasmonic resonators.

6. Conclusions

In this review we discuss general properties of plasmonic resonators and their use in multiple applications. Two orders of interaction can be distinguished: interaction of plasmonic nanostructures with propagating electromagnetic radiation and electron beams, and near-field interaction of surface plasmons with other properties of matter. In the first level are included the Mie scatterer, the optical nanoantenna, Fano resonances, plasmonic analogue of the EIT, enhanced optical transmission and light beaming and the plasmonic metasurfaces, resonators exhibiting toroidal and anapole modes, and non-linear processes on plasmonic particles. Among the effects of the near-fields generated by plasmonic resonances on matter in the immediate neighbourhood are the surface enhanced Raman scattering, the Purcell effect affecting the spontaneous emission, the strong coupling with multiple, or single emitters, the optical forces and the photothermal heating.

Based on the elementary plasmonic resonator properties and interactions novel applications have been investigated on a higher hierarchical level, where the effects rely either on collective resonances, or in the plasmon-electron interaction. These include the metamaterials and metasurfaces, the topological plasmonic materials and the very fast switching devices based on inelastic electron tunneling coupled with plasmonic elements.

We covered the major application areas where plasmonic resonators have been employed. The number of research fields using plasmonic nanostructures has constantly increased and new effects relying on enhanced near-fields at small volumes cannot dispense the unsurpassed light confinement achieved by these resonators. This is valid either for classical sensing applications, or for the most recent quantum optical applications, as the coupling between plasmonic and optomechanical resonators.

We cite the most relevant literature of the field in the last 10 years. The reader can use this review article to compare the advantages and limitations of each type of resonator and their adequacy for a custom-made application, or for engineering new kinds of resonators.

Acknowledgments

M R G thanks M Hammer, M Müller, C Zeh, I Sfarcic, S Rappl, A Kyumbi, J Iduwe, J Tang, M Nielsen and V Rao for the collaboration over the last 10 years if the preparation and characterisation of nanoparticles and plasmonic nanostructures and technical support in the laboratory. Special thanks also deserve to go to G Neusser and C Kranz for the FIB facility and S Jenisch of the nanolithography facility of the Ulm University.

We acknowledge the Ministry of Education and Science of the Republic of Armenia (Grant 18 T-1C222) and the German

Federal Ministry of Education and Research (BMBF Grant 01DK17040) for financial support provided in the last two years.

M R G also thanks W Barnes (University of Exeter, UK) and Antoine Moreau (Université Clermont-Auvergne, France) for discussions related to the guided modes in plasmonic multilayered materials.

ORCID iD

Manuel R Gonçalves https://orcid.org/0000-0001-9050-7857

References

[1] Marti O, Bielefeldt H, Hecht B, Herminghaus S, Leiderer P and Mlynek J 1993 Near-field optical measurement of the surface plasmon field *Opt. Commun.* **96** 225–8
[2] Ritchie R H 1957 Plasma losses by fast electrons in thin films *Phys. Rev.* **106** 874–81
[3] Kretschmann E and Raether H 1968 Notizen: radiative decay of non radiative surface plasmons excited by light *Z. Nat.* A **23** 2135–6
[4] Otto A 1968 Excitation of nonradiative surface plasma waves in silver by the method of frustrated total reflection *Z. Phys. A Hadrons Nuclei* **216** 398–410
[5] Mie G 1908 Beiträge zur Optik trüber Medien, speziell kolloidaler Metallösungen *Ann. Phys. Lpz.* **330** 377–445
[6] Faraday M 1857 X. The Bakerian lecture—experimental relations of gold (and other metals) to light *Phil. Trans. R. Soc. London* **147** 145–81
[7] Johnson P B and Christy R W 1972 Optical constants of the noble metals *Phys. Rev.* B **6** 4370–9
[8] Olmon R L, Iovick S B, Johnson T W, Shelton D, Oh S-H, Boreman G D and Raschke M B 2012 Optical dielectric function of gold *Phys. Rev.* B **86** 235147
[9] Yang H U, D'Archangel J, Sundheimer M L, Tucker E, Boreman G D and Raschke M B 2015 Optical dielectric function of silver *Phys. Rev.* B **91** 235137
[10] Knight M W, King N S, Liu L, Everitt H O, Nordlander P and Halas N J 2014 Aluminum for plasmonics *ACS Nano* **8** 834–40
[11] Mauchamp V, Bugnet M, Bellido E P, Botton G A, Moreau P, Magne D, Naguib M, Cabioc'h T and Barsoum M W 2014 Enhanced and tunable surface plasmons in two-dimensional Ti_3C_2 stacks: electronic structure versus boundary effects *Phys. Rev.* B **89** 235428
[12] West P R, Ishii S, Naik G V, Emani N K, Shalaev V M and Boltasseva A 2010 Searching for better plasmonic materials *Laser Photon. Rev.* **4** 795–808
[13] Naik G V, Shalaev V M and Boltasseva A 2013 Alternative plasmonic materials: beyond gold and silver *Adv. Mater.* **25** 3264–94
[14] Economou E N 1969 Surface plasmons in thin films *Phys. Rev.* **182** 539–54
[15] Sarid D 1981 Long-range surface-plasma waves on very thin metal films *Phys. Rev. Lett.* **47** 1927–30
[16] Boardman A D 1982 *Electromagnetic Surface Modes* (New York: Wiley)
[17] Raether H 1988 *Surface Plasmons on Smooth and Rough Surfaces and on Gratings* (Berlin: Springer)
[18] Maier S A 2007 *Plasmonics: Fundamentals and Applications* (New York: Springer)
[19] Ritchie R, Arakawa E, Cowan J and Hamm R 1968 Surface-plasmon resonance effect in grating diffraction *Phys. Rev. Lett.* **21** 1530–3
[20] Gramotnev D K and Pile D F P 2004 Single-mode subwavelength waveguide with channel plasmon-polaritons in triangular grooves on a metal surface *Appl. Phys. Lett.* **85** 6323–5
[21] Chen Z, Hooper I R and Sambles J R 2007 Coupled surface plasmons on thin silver gratings *J. Opt. A: Pure Appl. Opt.* **10** 015007
[22] Wood R W 1902 XLII. On a remarkable case of uneven distribution of light in a diffraction grating spectrum *London Edinburgh Dublin Phil. Mag. J. Sci.* **4** 396–402
[23] Rayleigh L 1907 III. Note on the remarkable case of diffraction spectra described by Prof. Wood *London Edinburgh Dublin Phil. Mag. J. Sci.* **14** 60–5
[24] Fano U 1938 Zur Theorie der Intensitätsanomalien der Beugung *Ann. Phys. Lpz.* **424** 393–443
[25] Hessel A and Oliner A A 1965 A new theory of Wood's anomalies on optical gratings *Appl. Opt.* **4** 1275
[26] Ebbesen T W, Lezec H J, Ghaemi H F, Thio T and Wolff P A 1998 Extraordinary optical transmission through sub-wavelength hole arrays *Nature* **391** 667–9
[27] Bethe H A 1944 Theory of diffraction by small holes *Phys. Rev.* **66** 163–82
[28] Kitson S C, Barnes W L and Sambles J R 1996 Full photonic band gap for surface modes in the visible *Phys. Rev. Lett.* **77** 2670–3
[29] Fano U 1935 Sullo spettro di assorbimento dei gas nobili presso il limite dello spettro d'arco *Il Nuovo Cimento* **12** 154–61
[30] Fano U, Pupillo G, Zannoni A and Clark C W 2005 On the absorption spectrum of noble gases at the arc spectrum limit *J. Res. Natl Inst. Stand. Technol.* **110** 583
[31] Fano U 1961 Effects of configuration interaction on intensities and phase shifts *Phys. Rev.* **124** 1866–78
[32] Della Valle G and Longhi S 2010 Geometric potential for plasmon polaritons on curved surfaces *J. Phys. B: At. Mol. Opt. Phys.* **43** 051002
[33] Libster-Hershko A, Shiloh R and Arie A 2019 Surface plasmon polaritons on curved surfaces *Optica* **6** 115
[34] Zhang J, Jun-Yu O, Papasimakis N, Yifang C, MacDonald K F and Zheludev N I 2011 Continuous metal plasmonic frequency selective surfaces *Opt. Express* **19** 23279
[35] Zhang J, Ou J-Y, MacDonald K F and Zheludev N I 2012 Optical response of plasmonic relief meta-surfaces *J. Opt.* **14** 114002
[36] Kristensen A, Yang J K W, Bozhevolnyi S I, Link S, Nordlander P, Halas N J and Mortensen N A 2016 Plasmonic colour generation *Nat. Rev. Mater.* **2** 16088
[37] Jacob Z, Alekseyev L V and Narimanov E 2006 Optical hyperlens: far-field imaging beyond the diffraction limit *Opt. Express* **14** 8247
[38] Salandrino A and Engheta N 2006 Far-field subdiffraction optical microscopy using metamaterial crystals: theory and simulations *Phys. Rev.* B **74** 075103
[39] Belov B A and Hao Y 2006 Subwavelength imaging at optical frequencies using a transmission device formed by a periodic layered metal-dielectric structure operating in the canalization regime *Phys. Rev.* B **73** 113110
[40] Pockrand I, Brillante A and Möbius D 1980 Nonradiative decay of excited molecules near a metal surface *Chem. Phys. Lett.* **69** 499–504
[41] Barnes W L 1998 Fluorescence near interfaces: The role of photonic mode density *J. Mod. Opt.* **45** 661–99
[42] Chance R R, Prock A and Silbey R 2007 Molecular fluorescence and energy transfer near interfaces *Advances in Chemical Physics* vol 37 (New York: Wiley) pp 1–65
[43] Ford G W and Weber W H 1984 Electromagnetic interactions of molecules with metal surfaces *Phys. Rep.* **113** 195–287
[44] Bohren C F and Huffman D R 1998 *Adsorption and Scattering of Light by Small Particles* (New York: Wiley)

[45] van de Hulst H C 1981 *Light Scattering by Small Particles* (New York: Dover)
[46] Kerker M, Wang D-S and Giles C L 1983 Electromagnetic scattering by magnetic spheres *J. Opt. Soc. Am.* **73** 765
[47] Kelly K L, Coronado E, Zhao L L and Schatz G C 2003 The optical properties of metal nanoparticles: the influence of size, shape and dielectric environment *J. Phys. Chem.* B **107** 668–77
[48] Noguez C 2007 Surface plasmons on metal nanoparticles: the influence of shape and physical environment *J. Phys. Chem.* C **111** 3806–19
[49] Haynes C L and Van Duyne R P 2001 Nanosphere lithography: a versatile nanofabrication tool for studies of size-dependent nanoparticle optics *J. Phys. Chem.* B **105** 5599–5611
[50] Sun Y 2002 Shape-controlled synthesis of gold and silver nanoparticles *Science* **298** 2176–9
[51] Hohenau A, Ditlbacher H, Bernhard L, Krenn J R, Leitner A and Aussenegg F R 2006 Electron beam lithography, a helpful tool for nanooptics *Microelectron. Eng.* **83** 1464–7
[52] Huang J-S *et al* 2010 Atomically flat single-crystalline gold nanostructures for plasmonic nanocircuitry *Nat. Commun.* **1** 150
[53] Link S and El-Sayed M A 1999 Spectral properties and relaxation dynamics of surface plasmon electronic oscillations in gold and silver nanodots and nanorods *J. Phys. Chem.* B **103** 8410–26
[54] Prodan E, Radloff C, Halas N J and Nordlander P 2003 A hybridization model for the plasmon response of complex nanostructures *Science* **302** 419–22
[55] Pohl D W, Denk W and Lanz M 1984 Optical stethoscopy: image recording with resolution $\lambda/20$ *Appl. Phys. Lett.* **44** 651–3
[56] Moskovits M 1985 Surface-enhanced spectroscopy *Rev. Mod. Phys.* **57** 783–826
[57] Sönnichsen C *et al* 2000 Spectroscopy of single metallic nanoparticles using total internal reflection microscopy *Appl. Phys. Lett.* **77** 2949–51
[58] Nelayah J *et al* 2007 Mapping surface plasmons on a single metallic nanoparticle *Nat. Phys.* **3** 348–53
[59] Kuttge M, Vesseur E J R, Koenderink A F, Lezec H J, Atwater H A, García de Abajo F J and Polman A 2009 Local density of states, spectrum and far-field interference of surface plasmon polaritons probed by cathodoluminescence *Phys. Rev.* B **79** 113405
[60] Douillard L and Charra F 2013 Photoemission electron microscopy, a tool for plasmonics *J. Electron Spectrosc. Relat. Phenom.* **189** 24–9
[61] Kreibig U and Vollmer M 1995 *Optical Properties of Metal Clusters* (Berlin: Springer)
[62] David C and Javier García de Abajo F 2011 Spatial nonlocality in the optical response of metal nanoparticles *J. Phys. Chem.* C **115** 19470–5
[63] Mortensen N A, Raza S, Wubs M, Søndergaard T and Bozhevolnyi S I 2014 A generalized non-local optical response theory for plasmonic nanostructures *Nat. Commun.* **5** 3809
[64] Hwang E H and Das Sarma S 2007 Dielectric function, screening and plasmons in two-dimensional graphene *Phys. Rev.* B **75** 205418
[65] Hanson G W 2008 Dyadic Green's functions and guided surface waves for a surface conductivity model of graphene *J. Appl. Phys.* **103** 064302
[66] Koppens F H L, Chang D E and García de Abajo F J 2011 Graphene plasmonics: A platform for strong light-matter interactions *Nano Lett.* **11** 3370–7
[67] Bludov Y V, Aires F, Peres N M R and Vasilevskiy M I 2013 A primer on surface plasmon-polaritons in graphene *Int. J. Mod. Phys.* B **27** 1341001
[68] Brar V W, Seok Jang M, Sherrott M, Lopez J J and Atwater H A 2013 Highly confined tunable mid-infrared plasmonics in graphene nanoresonators *Nano Lett.* **13** 2541–7
[69] García de Abajo F J 2014 Graphene plasmonics: challenges and opportunities *ACS Photon.* **1** 135–52
[70] Gonçalves P A D and Peres N M R 2015 *An Introduction to Graphene Plasmonics* (Singapore: World Scientific)
[71] Yu R, Liz-Marzán L M and García de Abajo F J 2017 Universal analytical modeling of plasmonic nanoparticles *Chem. Soc. Rev.* **46** 6710–24
[72] Jablan M, Buljan H and Soljačić M 2009 Plasmonics in graphene at infrared frequencies *Phys. Rev.* B **80** 245435
[73] Low T and Avouris P 2014 Graphene plasmonics for terahertz to mid-infrared applications *ACS Nano* **8** 1086–101
[74] Neira A D, Olivier N, Nasir M E, Dickson W, Wurtz G A and Zayats A V 2015 Eliminating material constraints for nonlinearity with plasmonic metamaterials *Nat. Commun.* **6** 7757
[75] Lalisse A, Tessier G, Plain J and Baffou G 2015 Quantifying the efficiency of plasmonic materials for near-field enhancement and photothermal conversion *J. Phys. Chem.* C **119** 25518–28
[76] Khamh H, Sachet E, Kelly K, Maria J-P and Franzen S 2018 As good as gold and better: conducting metal oxide materials for mid-infrared plasmonic applications *J. Mater. Chem.* C **6** 8326–42
[77] Albrecht G, Ubl M, Kaiser S, Giessen H and Hentschel M 2018 Comprehensive study of plasmonic materials in the visible and near-infrared: linear, refractory and nonlinear optical properties *ACS Photonics* **5** 1058–67
[78] Panoiu N C, Sha W E I, Lei D Y and Li G-C 2018 Nonlinear optics in plasmonic nanostructures *J. Opt.* **20** 083001
[79] Kinsey N, DeVault C, Boltasseva A and Shalaev V M 2019 Near-zero-index materials for photonics *Nat. Rev. Mater.* **4** 742–60
[80] Novotny L and Hecht B 2012 *Principles of Nano-Optics* 2nd edn (Cambridge: Cambridge University Press)
[81] Kats M A, Woolf D, Blanchard R, Nanfang Y and Capasso F 2011 Spoof plasmon analogue of metal-insulator-metal waveguides *Opt. Express* **19** 14860
[82] Klar T, Perner M, Grosse S, von Plessen G, Spirkl W and Feldmann J 1998 Surface-plasmon resonances in single metallic nanoparticles *Phys. Rev. Lett.* **80** 4249–52
[83] Hodak J H, Martini I and Hartland G V 1998 Spectroscopy and dynamics of nanometer-sized noble metal particles *J. Phys. Chem.* B **102** 6958–67
[84] Sönnichsen C, Franzl T, Wilk T, von Plessen G, Feldmann J, Wilson O and Mulvaney P 2002 Drastic reduction of plasmon damping in gold nanorods *Phys. Rev. Lett.* **88** 077402
[85] Minassian H, Madoyan K and Melikyan A 2012 Strong suppression of surface plasmon radiation damping rate in noble metal nanoshells *Plasmonics* **7** 745–8
[86] Della Valle G, Søndergaard T and Bozhevolnyi S I 2009 Efficient suppression of radiation damping in resonant retardation-based plasmonic structures *Phys. Rev.* B **79** 113410
[87] Della Valle G and Bozhevolnyi S I 2012 Efficient suppression of radiation damping in individual plasmonic resonators: towards high-Q nano-volume sensing *Ann. Phys. Lpz.* **524** 253–72
[88] Kats M A, Yu N, Genevet P, Gaburro Z and Capasso F 2011 Effect of radiation damping on the spectral response of plasmonic components *Opt. Express* **19** 21748
[89] Kolwas K and Derkachova A 2013 Damping rates of surface plasmons for particles of size from nano- to micrometers;

reduction of the nonradiative decay *J. Quant. Spectrosc. Radiat. Transfer* **114** 45–55
[90] Lee K-S and El-Sayed M A 2005 Dependence of the enhanced optical scattering efficiency relative to that of absorption for gold metal nanorods on aspect ratio, size, end-cap shape and medium refractive index *J. Phys. Chem.* B **109** 20331–8
[91] Novotny L 2007 Effective wavelength scaling for optical antennas *Phys. Rev. Lett.* **98** 266802
[92] Khlebtsov B N and Khlebtsov N G 2007 Multipole plasmons in metal nanorods: scaling properties and dependence on particle size, shape, orientation and dielectric environment *J. Phys. Chem.* C **111** 11516–27
[93] Khlebtsov N G 2008 Optics and biophotonics of nanoparticles with a plasmon resonance *Quantum Electron.* **38** 504–29
[94] Joe Y S, Satanin A M and Sub Kim C 2006 Classical analogy of Fano resonances *Phys. Scr.* **74** 259–66
[95] Gallinet B and Martin O J F 2011 *Ab initio* theory of Fano resonances in plasmonic nanostructures and metamaterials *Phys. Rev.* B **83** 235427
[96] Garrido Alzar C L, Martinez M A G and Nussenzveig P 2002 Classical analog of electromagnetically induced transparency *Am. J. Phys.* **70** 37–41
[97] Hao F, Sonnefraud Y, Van Dorpe P, Maier S A, Halas N J and Nordlander P 2008 Symmetry breaking in plasmonic nanocavities: subradiant LSPR sensing and a tunable Fano resonance *Nano Lett.* **8** 3983–8
[98] Zhang S, Genov D A, Wang Y, Liu M and Zhang X 2008 Plasmon-induced transparency in metamaterials *Phys. Rev. Lett.* **101** 047401
[99] Verellen N, Sonnefraud Y, Sobhani H, Feng H, Moshchalkov V V, Van Dorpe P, Nordlander P and Maier S A 2009 Fano resonances in individual coherent plasmonic nanocavities *Nano Lett.* **9** 1663–7
[100] Miroshnichenko A E, Flach S and Kivshar Y S 2010 Fano resonances in nanoscale structures *Rev. Mod. Phys.* **82** 2257–98
[101] Luk'yanchuk B, Zheludev N I, Maier S A, Halas N J, Nordlander P, Giessen H and Chong C T 2010 The Fano resonance in plasmonic nanostructures and metamaterials *Nat. Mater.* **9** 707–15
[102] Gallinet B and Martin O J F 2011 Relation between near–field and far–field properties of plasmonic Fano resonances *Opt. Express* **19** 22167
[103] Giannini V, Francescato Y, Hemmel A, Phillips C C and Maier S A 2011 Fano resonances in nanoscale plasmonic systems: a parameter-free modeling approach *Nano Lett.* **11** 2835–40
[104] Hsing Fu Y, Bo Zhang J, Feng Yu Y and Luk'yanchuk B 2012 Generating and manipulating higher order Fano resonances in dual-disk ring plasmonic nanostructures *ACS Nano* **6** 5130–7
[105] Francescato Y, Giannini V and Maier S A 2012 Plasmonic systems unveiled by Fano resonances *ACS Nano* **6** 1830–8
[106] Grigoriev V, Varault S, Boudarham G, Stout B, Wenger J and Bonod N 2013 Singular analysis of Fano resonances in plasmonic nanostructures *Phys. Rev.* A **88** 063805
[107] Lovera A, Gallinet B, Nordlander P and Martin O J F 2013 Mechanisms of Fano Resonances in Coupled Plasmonic Systems *ACS Nano* **7** 4527–36
[108] Butet J and Martin O J F 2014 Fano resonances in the nonlinear optical response of coupled plasmonic nanostructures *Opt. Express* **22** 29693
[109] Gonçalves M R, Melikyan A, Minassian H, Makaryan T and Marti O 2014 Strong dipole-quadrupole coupling and Fano resonance in H-like metallic nanostructures *Opt. Express* **22** 24516
[110] Yan C, Yang K-Y and Martin O J F 2017 Fano-resonance-assisted metasurface for color routing *Light Sci. Appl.* **6** e17017
[111] Limonov M F, Rybin M V, Poddubny A N and Kivshar Y S 2017 Fano resonances in photonics *Nat. Photon.* **11** 543–54
[112] Purcell E M 1946 Spontaneous emission probabilities at radio frequencies *Phys. Rev.* **69** 681
[113] Rabi I I 1936 On the process of space quantization *Phys. Rev.* **49** 324
[114] Törmä P and Barnes W L 2014 Strong coupling between surface plasmon polaritons and emitters: a review *Rep. Prog. Phys.* **78** 013901
[115] Novotny L 2010 Strong coupling, energy splitting and level crossings: A classical perspective *Am. J. Phys.* **78** 1199–202
[116] Rempe G, Thompson R J and Kimble H J 1994 Cavity quantum electrodynamics with strong coupling in the optical domain *Phys. Scr.* **T51** 67–77
[117] Kimble H J 1998 Strong interactions of single atoms and photons in cavity QED *Phys. Scr.* **T76** 127
[118] Walther H, Varcoe B T H, Englert B-G and Becker T 2006 Cavity quantum electrodynamics *Rep. Prog. Phys.* **69** 1325–82
[119] Rodriguez S R-K 2016 Classical and quantum distinctions between weak and strong coupling *Eur. J. Phys.* **37** 025802
[120] Ameling R and Giessen H 2012 Microcavity plasmonics: strong coupling of photonic cavities and plasmons *Laser Photon. Rev.* **7** 141–69
[121] Chikkaraddy R *et al* 2016 Single-molecule strong coupling at room temperature in plasmonic nanocavities *Nature* **535** 127–30
[122] Harris S E, Field J E and Imamoğlu A 1990 Nonlinear optical processes using electromagnetically induced transparency *Phys. Rev. Lett.* **64** 1107–10
[123] Boller K-J, Imamoğlu A and Harris S E 1991 Observation of electromagnetically induced transparency *Phys. Rev. Lett.* **66** 2593–6
[124] Harris S E 1997 Electromagnetically induced transparency *Phys. Today* **50** 36–42
[125] Fleischhauer M, Imamoglu A and Marangos J P 2005 Electromagnetically induced transparency: optics in coherent media *Rev. Mod. Phys.* **77** 633–73
[126] Hau L V, Harris S E, Dutton Z and Behroozi C H 1999 Light speed reduction to 17 metres per second in an ultracold atomic gas *Nature* **397** 594–8
[127] Liu N, Langguth L, Weiss T, Kästel J, Fleischhauer M, Pfau T and Giessen H 2009 Plasmonic analogue of electromagnetically induced transparency at the Drude damping limit *Nat. Mater.* **8** 758–62
[128] Taubert R, Hentschel M, Kästel J and Giessen H 2012 Classical analog of electromagnetically induced absorption in plasmonics *Nano Lett.* **12** 1367–71
[129] Taubert R, Hentschel M and Giessen H 2013 Plasmonic analog of electromagnetically induced absorption: simulations, experiments and coupled oscillator analysis *J. Opt. Soc. Am.* B **30** 3123
[130] Case W B and Swanson M A 1990 The pumping of a swing from the seated position *Am. J. Phys.* **58** 463–7
[131] Case W B 1996 The pumping of a swing from the standing position *Am. J. Phys.* **64** 215–20
[132] Roura P and González J A 2010 Towards a more realistic description of swing pumping due to the exchange of angular momentum *Eur. J. Phys.* **31** 1195–207
[133] Rayleigh L 1887 On the maintenance of vibrations by forces of double frequency, and on the propagation of waves

through a medium endowed with a periodic structure *London Edinburgh Dublin Phil. Mag. J. Sci.* **24** 145–59
[134] Dmitriev A V and Mitrofanov V P 2014 Enhanced interaction between a mechanical oscillator and two coupled resonant electrical circuits *Rev. Sci. Instrum.* **85** 085005
[135] Hill G W 1886 On the part of the motion of the lunar perigee which is a function of the mean motions of the sun and moon *Acta Math.* **8** 1–36
[136] Mclachlan N W 1964 *Theory and Application of Mathieu Functions* (New York: Dover)
[137] Louisell W H, Yariv A and Siegman A E 1961 Quantum fluctuations and noise in parametric processes. I. *Phys. Rev.* **124** 1646–54
[138] Kroll N M 1962 Parametric amplification in spatially extended media and application to the design of tuneable oscillators at optical frequencies *Phys. Rev.* **127** 1207–11
[139] Grigor'ev Y V, Rudenko V K and Khokhlov R V 1966 Theory of the parametric light generator *Sov. Radiophys.* **9** 545–9
[140] Giordmaine J A and Miller R C 1965 Tunable coherent parametric oscillation in $LiNbO_3$ *Phys. Rev. Lett.* **14** 973–6
[141] Salandrino A 2018 Plasmonic parametric resonance *Phys. Rev.* B **97**
[142] Fardad S and Salandrino A 2018 Plasmonic parametric absorbers *Opt. Lett.* **43** 6013
[143] Schwartz T 2018 Plasmonic mirrorless optical parametric oscillator *ACS Photonics* **5** 4265–9
[144] Thijssen R, Kippenberg T J, Polman A and Verhagen E 2014 Parallel transduction of nanomechanical motion using plasmonic resonators *ACS Photonics* **1** 1181–8
[145] Fleischmann M, Hendra P J and McQuillan A J 1974 Raman spectra of pyridine adsorbed at a silver electrode *Chem. Phys. Lett.* **26** 163–6
[146] Otto A 1983 Surface enhanced Raman scattering *Vacuum* **33** 797–802
[147] Campion A and Kambhampati P 1998 Surface-enhanced Raman scattering *Chem. Soc. Rev.* **27** 241
[148] Le Ru E C, Blackie E, Meyer M and Etchegoin P G 2007 Surface enhanced Raman scattering enhancement factors: a comprehensive study *J. Phys. Chem.* C **111** 13794–803
[149] Stiles P L, Dieringer J A, Shah N C and Van Duyne R P 2008 Surface-enhanced Raman spectroscopy *Ann. Rev. Anal. Chem.* **1** 601–26
[150] Pieczonka N P W and Aroca R F 2008 Single molecule analysis by surfaced-enhanced Raman scattering *Chem. Soc. Rev.* **37** 946
[151] Etchegoin P G and Le Ru E C 2008 A perspective on single molecule SERS: current status and future challenges *Phys. Chem. Chem. Phys.* **10** 6079
[152] Le Ru E C and Etchegoin P G 2012 Single-molecule surface-enhanced Raman spectroscopy *Ann. Rev. Phys. Chem.* **63** 65–87
[153] Kleppner D 1981 Inhibited spontaneous emission *Phys. Rev. Lett.* **47** 233–6
[154] Ruppin R 1982 Decay of an excited molecule near a small metal sphere *J. Chem. Phys.* **76** 1681–4
[155] Maier S A 2006 Plasmonic field enhancement and SERS in the effective mode volume picture *Opt. Express* **14** 1957
[156] Koenderink A F 2010 On the use of Purcell factors for plasmon antennas *Opt. Lett.* **35** 4208
[157] Kristensen P T, Van Vlack C and Hughes S 2012 Generalized effective mode volume for leaky optical cavities *Opt. Lett.* **37** 1649
[158] Kristensen P T and Hughes S 2013 Modes and mode volumes of leaky optical cavities and plasmonic nanoresonators *ACS Photonics* **1** 2–10
[159] Vesseur E J R, García de Abajo F J and Polman A 2010 Broadband Purcell enhancement in plasmonic ring cavities *Phys. Rev.* B **82** 165419
[160] Kuttge M, García de Abajo F J and Polman A 2010 Ultrasmall mode volume plasmonic nanodisk resonators *Nano Lett.* **10** 1537–41
[161] Hümmer T, García-Vidal F J, Martín-Moreno L and Zueco D 2013 Weak and strong coupling regimes in plasmonic QED *Phys. Rev.* B **87** 115419
[162] Dezfouli M K, Gordon R and Hughes S 2017 Modal theory of modified spontaneous emission of a quantum emitter in a hybrid plasmonic photonic-crystal cavity system *Phys. Rev.* A **95** 013846
[163] Hughes S, Franke S, Gustin C, Dezfouli M K, Knorr A and Richter M 2019 Theory and limits of on-demand single-photon sources using plasmonic resonators: a quantized quasinormal mode approach *ACS Photonics* **6** 2168–80
[164] Bogdanov S I *et al* 2018 Ultrabright room-temperature sub-nanosecond emission from single nitrogen-vacancy centers coupled to nanopatch antennas *Nano Lett.* **18** 4837–44
[165] Bouwkamp C J 1950 On Bethe's theory of diffraction by small holes *Philips Res. Rep.* **5** 321–32
[166] Yi J-M *et al* 2012 Diffraction regimes of single holes *Phys. Rev. Lett.* **109** 023901
[167] Martín-Moreno L, García-Vidal F J, Lezec H J, Pellerin K M, Thio T, Pendry J B and Ebbesen T W 2001 Theory of extraordinary optical transmission through subwavelength hole arrays *Phys. Rev. Lett.* **86** 1114–7
[168] Genet C, van Exter M P and Woerdman J P 2003 Fano-type interpretation of red shifts and red tails in hole array transmission spectra *Opt. Commun.* **225** 331–6
[169] Mary A, Rodrigo S G, Garcia-Vidal F J and Martin-Moreno L 2008 Theory of negative-refractive-index response of double-fishnet structures *Phys. Rev. Lett.* **101** 103902
[170] Liu N, Liwei F, Kaiser S, Schweizer H and Giessen H 2008 Plasmonic building blocks for magnetic molecules in three-dimensional optical metamaterials *Adv. Mater.* **20** 3859–65
[171] Lezec H J 2002 Beaming light from a subwavelength aperture *Science* **297** 820–2
[172] García de Abajo F J 2007 *Colloquium*: light scattering by particle and hole arrays *Rev. Mod. Phys.* **79** 1267–90
[173] Garcia-Vidal F J, Martin-Moreno L, Ebbesen T W and Kuipers L 2010 Light passing through subwavelength apertures *Rev. Mod. Phys.* **82** 729–87
[174] Collin S 2014 Nanostructure arrays in free-space: optical properties and applications *Rep. Prog. Phys.* **77** 126402
[175] Coronado E A and Schatz G C 2003 Surface plasmon broadening for arbitrary shape nanoparticles: a geometrical probability approach *J. Chem. Phys.* **119** 3926–34
[176] Norton S J and Vo-Dinh T 2007 Plasmon resonances of nanoshells of spheroidal shape *IEEE Trans. Nanotechnology* **6** 627–38
[177] Myroshnychenko V, Rodríguez-Fernández J, Pastoriza-Santos I, Funston A M, Novo C, Mulvaney P, Liz-Marzán L M and García de Abajo F J 2008 Modelling the optical response of gold nanoparticles *Chem. Soc. Rev.* **37** 1792
[178] Myroshnychenko V, Carbó-Argibay E, Pastoriza-Santos I, Pérez-Juste J, Liz-Marzán L M and García de Abajo F J 2008 Modeling the optical response of highly faceted metal nanoparticles with a fully 3D boundary element method *Adv. Mater.* **20** 4288–93
[179] Curto A G, Volpe G, Taminiau T H, Kreuzer M P, Quidant R and van Hulst N F 2010 Unidirectional emission of a quantum dot coupled to a nanoantenna *Science* **329** 930–3

[180] Taminiau T H, Stefani F D and van Hulst N F 2011 Optical nanorod antennas modeled as cavities for dipolar emitters: evolution of sub- and super-radiant modes *Nano Lett.* **11** 1020–4
[181] Novotny L and van Hulst N 2011 Antennas for light *Nat. Photon.* **5** 83–90
[182] Coenen T, Vesseur E J R, Polman A and Koenderink A F 2011 Directional emission from plasmonic yagi-uda antennas probed by angle-resolved cathodoluminescence spectroscopy *Nano Lett.* **11** 3779–84
[183] Giannini V, Fernández-Domínguez A I, Heck S C and Maier S A 2011 Plasmonic nanoantennas: fundamentals and their use in controlling the radiative properties of nanoemitters *Chem. Rev.* **111** 3888–912
[184] Zhu W, Wang D and Crozier K B 2012 Direct observation of beamed Raman scattering *Nano Lett.* **12** 6235–43
[185] Biagioni P, Huang J-S and Hecht B 2012 Nanoantennas for visible and infrared radiation *Rep. Prog. Phys.* **75** 024402
[186] Curto A G, Taminiau T H, Volpe G, Kreuzer M P, Quidant R and van Hulst N F 2013 Multipolar radiation of quantum emitters with nanowire optical antennas *Nat. Commun.* **4** 1750
[187] Schuck P J, Fromm D P, Sundaramurthy A, Kino G S and Moerner W E 2005 Improving the mismatch between light and nanoscale objects with gold bowtie nanoantennas *Phys. Rev. Lett.* **94** 017402
[188] Muskens O L, Giannini V, Sánchez-Gil J A and Gómez Rivas J and 2007 Strong enhancement of the radiative decay rate of emitters by single plasmonic nanoantennas *Nano Lett.* **7** 2871–5
[189] Vesseur E J R and Polman A 2011 Plasmonic whispering gallery cavities as optical nanoantennas *Nano Lett.* **11** 5524–30
[190] Thijssen R, Kippenberg T J, Polman A and Verhagen E 2015 Plasmomechanical resonators based on dimer nanoantennas *Nano Lett.* **15** 3971–6
[191] Zambrana-Puyalto X and Bonod N 2015 Purcell factor of spherical Mie resonators *Phys. Rev.* B **91** 195422
[192] Muljarov E A and Langbein W 2016 Exact mode volume and Purcell factor of open optical systems *Phys. Rev.* B **94** 235438
[193] Doeleman H M, Verhagen E and Koenderink A F 2016 Antenna-cavity hybrids: matching polar opposites for Purcell enhancements at any linewidth *ACS Photon.* **3** 1943–51
[194] Ruesink F, Doeleman H M, Verhagen E and Koenderink A F 2018 Controlling nanoantenna polarizability through backaction via a single cavity mode *Phys. Rev. Lett.* **120** 206101
[195] Ditlbacher H, Hohenau A, Wagner D, Kreibig U, Rogers M, Hofer F, Aussenegg F R and Krenn J R 2005 Silver nanowires as surface plasmon resonators *Phys. Rev. Lett.* **95** 257403
[196] Kuttge M, Vesseur E J R, Verhoeven J, Lezec H J, Atwater H A and Polman A 2008 Loss mechanisms of surface plasmon polaritons on gold probed by cathodoluminescence imaging spectroscopy *Appl. Phys. Lett.* **93** 113110
[197] Nagpal P, Lindquist N C, Oh S-H and Norris D J 2009 Ultrasmooth patterned metals for plasmonics and metamaterials *Science* **325** 594–7
[198] Wild B, Cao L, Sun Y, Khanal B P, Zubarev E R, Gray S K, Scherer N F and Pelton M 2012 Propagation lengths and group velocities of plasmons in chemically synthesized gold and silver nanowires *ACS Nano* **6** 472–82
[199] Méjard R *et al* 2017 Advanced engineering of single-crystal gold nanoantennas *Opt. Mater. Express* **7** 1157
[200] Chen K-P, Drachev V P, Borneman J D, Kildishev A V and Shalaev V M 2010 Drude relaxation rate in grained gold nanoantennas *Nano Lett.* **10** 916–22
[201] Habteyes T G, Dhuey S, Wood E, Gargas D, Cabrini S, Schuck P J, Alivisatos A P and Leone S R 2012 Metallic adhesion layer induced plasmon damping and molecular linker as a nondamping alternative *ACS Nano* **6** 5702–9
[202] Lieb M A, Zavislan J M and Novotny L 2004 Single-molecule orientations determined by direct emission pattern imaging *J. Opt. Soc. Am.* B **21** 1210
[203] Drezet A, Hohenau A, Koller D, Stepanov A, Ditlbacher H, Steinberger B, Aussenegg F R, Leitner A and Krenn J R 2008 Leakage radiation microscopy of surface plasmon polaritons *Mater. Sci. Eng.* B **149** 220–9
[204] Shegai T, Miljkovicć V D, Bao K, Xu H, Nordlander P, Johansson P and Käll M 2011 Unidirectional broadband light emission from supported plasmonic nanowires *Nano Lett.* **11** 706–11
[205] Sersic I, Tuambilangana C and Koenderink A F 2011 Fourier microscopy of single plasmonic scatterers *New J. Phys.* **13** 083019
[206] Backer A S and Moerner W E 2014 Extending single-molecule microscopy using optical Fourier processing *J. Phys. Chem.* B **118** 8313–29
[207] Dominguez D, Alharbi N, Alhusain M, Bernussi A A and Grave de Peralta L 2014 Fourier plane imaging microscopy *J. Appl. Phys.* **116** 103102
[208] Kurvits J A, Jiang M and Zia R 2015 Comparative analysis of imaging configurations and objectives for Fourier microscopy *J. Opt. Soc. Am.* A **32** 2082
[209] Böhmer M and Enderlein Jorg 2003 Orientation imaging of single molecules by wide-field epifluorescence microscopy *J. Opt. Soc. Am.* B **20** 554
[210] Taminiau T H, Karaveli S, van Hulst N F and Zia R 2012 Quantifying the magnetic nature of light emission *Nat. Commun.* **3** 979
[211] Vesseur E J R, de Waele Re, Kuttge M and Polman A 2007 Direct observation of plasmonic modes in au nanowires using high-resolution cathodoluminescence spectroscopy *Nano Lett.* **7** 2843–6
[212] Coenen T, Vesseur E J R and Polman A 2012 Deep subwavelength spatial characterization of angular emission from single-crystal au plasmonic ridge nanoantennas *ACS Nano* **6** 1742–50
[213] Coenen T and Haegel N M 2017 Cathodoluminescence for the 21st century: learning more from light *App. Phys. Rev.* **4** 031103
[214] Armani D K, Kippenberg T J, Spillane S M and Vahala K J 2003 Ultra-high-Q toroid microcavity on a chip *Nature* **421** 925–8
[215] Min B, Ostby E, Sorger V, Ulin-Avila E, Yang L, Zhang X and Vahala K 2009 High-Q surface-plasmon-polariton whispering-gallery microcavity *Nature* **457** 455–8
[216] Kippenberg T J and Vahala K J 2007 Cavity opto-mechanics *Opt. Express* **15** 17172
[217] Aspelmeyer M, Kippenberg T J and Marquardt F 2014 Cavity optomechanics *Rev. Mod. Phys.* **86** 1391–452
[218] Thijssen R, Verhagen E, Kippenberg T J and Polman A 2013 Plasmon nanomechanical coupling for nanoscale transduction *Nano Lett.* **13** 3293–7
[219] Roelli P, Galland C, Piro N and Kippenberg T J 2015 Molecular cavity optomechanics as a theory of plasmon-enhanced Raman scattering *Nat. Nanotechnol.* **11** 164–9
[220] Haffner C *et al* 2019 Nano–opto-electro-mechanical switches operated at CMOS-level voltages *Science* **366** 860–4
[221] Landau L D and Lifshitz E M 1960 *Electrodynamics Continuous Media* (Oxford: Pergamon)

[222] Merlin R 2009 Metamaterials and the Landau–Lifshitz permeability argument: large permittivity begets high-frequency magnetism *Proc. Natl Acad. Sci.* **106** 1693–8
[223] Engheta N and Jaggard D 1988 Electromagnetic chirality and its applications *IEEE Antennas Propag. Soc. Newsletter* **30** 6–12
[224] Gay-Balmaz P and Martin O J F 2002 Electromagnetic resonances in individual and coupled split-ring resonators *J. Appl. Phys.* **92** 2929–36
[225] Enkrich C, Wegener M, Linden S, Burger S, Zschiedrich L, Schmidt F, Zhou J F, Koschny T and Soukoulis C M 2005 Magnetic metamaterials at telecommunication and visible frequencies *Phys. Rev. Lett.* **95** 203901
[226] Linden S *et al* 2006 Photonic metamaterials: magnetism at optical frequencies *IEEE J. Sel. Top. Quantum Electron.* **12** 1097–105
[227] Klein M W, Enkrich C, Wegener M, Soukoulis C M and Linden S 2006 Single-slit split-ring resonators at optical frequencies: limits of size scaling *Opt. Lett.* **31** 1259
[228] Liu N, Kaiser S and Giessen H 2008 Magnetoinductive and electroinductive coupling in plasmonic metamaterial molecules *Adv. Mater.* **20** 4521–5
[229] Shafiei F, Monticone F, Le K Q, Liu X-X, Hartsfield T, Alù A and Li X 2013 A subwavelength plasmonic metamolecule exhibiting magnetic-based optical Fano resonance *Nat. Nanotechnol.* **8** 95–9
[230] Sheikholeslami S N, García-Etxarri A and Dionne J A 2011 Controlling the interplay of electric and magnetic modes via Fano-like plasmon resonances *Nano Lett.* **11** 3927–34
[231] Veselago V G 1968 The electrodynamics of substances with simultaneously negative values of ε and μ *Sov. Phys. Uspekhi* **10** 509–14
[232] Smith D R, Padilla W J, Vier D C, Nemat-Nasser S C and Schultz S 2000 Composite medium with simultaneously negative permeability and permittivity *Phys. Rev. Lett.* **84** 4184–7
[233] Shelby R A 2001 Experimental verification of a negative index of refraction *Science* **292** 77–9
[234] Dolling G, Wegener M, Soukoulis C M and Linden S 2006 Negative-index metamaterial at 780 nm wavelength *Opt. Lett.* **32** 53
[235] Burgos S P, de Waele R, Polman A and Atwater H A 2010 A single-layer wide-angle negative-index metamaterial at visible frequencies *Nat. Mater.* **9** 407–12
[236] Xiao S, Chettiar U K, Kildishev A V, Drachev V, Khoo I C and Shalaev V M 2009 Tunable magnetic response of metamaterials *Appl. Phys. Lett.* **95** 033115
[237] Chen X, Grzegorczyk T M, Wu B I, Pacheco J and Au Kong J 2004 Robust method to retrieve the constitutive effective parameters of metamaterials *Phys. Rev.* E **70** 016608
[238] Zhang S, Fan W, Panoiu N C, Malloy K J, Osgood R M and Brueck S R J 2005 Experimental demonstration of near-infrared negative-index metamaterials *Phys. Rev. Lett.* **95** 137404
[239] Zhang S, Fan W, Malloy K J, Brueck S R J, Panoiu N C and Osgood R M 2005 Near-infrared double negative metamaterials *Opt. Express* **13** 4922
[240] Pendry J B 2000 Negative refraction makes a perfect lens *Phys. Rev. Lett.* **85** 3966–9
[241] Fang N, Lee H, Sun C and Zhang X 2005 Sub-diffraction-limited optical imaging with a silver superlens *Science* **308** 534–7
[242] Smith D R 2005 How to build a superlens *Science* **308** 502–3
[243] Garcia N and Nieto-Vesperinas M 2002 Left-handed materials do not make a perfect lens *Phys. Rev. Lett.* **88** 207403
[244] Decker M, Klein M W, Wegener M and Linden S 2007 Circular dichroism of planar chiral magnetic metamaterials *Opt. Lett.* **32** 856
[245] Govorov A O, Fan Z, Hernandez P, Slocik J M and Naik R R 2010 Theory of circular dichroism of nanomaterials comprising chiral molecules and nanocrystals: plasmon enhancement, dipole interactions and dielectric effects *Nano Lett.* **10** 1374–82
[246] García-Etxarri A and Dionne J A 2013 Surface-enhanced circular dichroism spectroscopy mediated by nonchiral nanoantennas *Phys. Rev.* B **87** 235409
[247] Papakostas A, Potts A, Bagnall D M, Prosvirnin S L, Coles H J and Zheludev N I 2003 Optical manifestations of planar chirality *Phys. Rev. Lett.* **90** 107404
[248] Rogacheva A V, Fedotov V A, Schwanecke A S and Zheludev N I 2006 Giant gyrotropy due to electromagnetic-field coupling in a bilayered chiral structure *Phys. Rev. Lett.* **97** 177401
[249] Liu N, Liu H, Zhu S and Giessen H 2009 Stereometamaterials *Nat. Photon.* **3** 157–62
[250] Gansel J K, Wegener M, Burger S and Linden S 2010 Gold helix photonic metamaterials: a numerical parameter study *Opt. Express* **18** 1059
[251] Guerrero-Martínez A, Alonso-Gómez J L, Auguié B, Magdalena Cid M and Liz-Marzán L M 2011 From individual to collective chirality in metal nanoparticles *Nano Today* **6** 381–400
[252] Kuzyk A, Schreiber R, Fan Z, Pardatscher G, Roller E-M, Högele A, Simmel F C, Govorov A O and Liedl T 2012 DNA-based self-assembly of chiral plasmonic nanostructures with tailored optical response *Nature* **483** 311–4
[253] Frank B, Yin X, Schäferling M, Zhao J, Hein S M, Braun P V and Giessen H 2013 Large-area 3D chiral plasmonic structures *ACS Nano* **7** 6321–9
[254] Yin X, Schäferling M, Metzger B and Giessen H 2013 Interpreting chiral nanophotonic spectra: the plasmonic Born-Kuhn model *Nano Lett.* **13** 6238–43
[255] Hentschel M, Schäferling M, Duan X, Giessen H and Liu N 2017 Chiral plasmonics *Sci. Adv.* **3** e1602735
[256] Valev V K, Baumberg J J, Sibilia C and Verbiest T 2013 Chirality and chiroptical effects in plasmonic nanostructures: fundamentals, recent progress and outlook *Adv. Mater.* **25** 2517–34
[257] Collins J T, Kuppe C, Hooper D C, Collins C, Centini M and Valev V K 2017 Chirality and chiroptical effects in metal nanostructures: fundamentals and current trends *Adv. Opt. Mater.* **5** 1700182
[258] Cameron R P, Barnett S M and Yao A M 2012 Optical helicity, optical spin and related quantities in electromagnetic theory *New J. Phys.* **14** 053050
[259] Nieto-Vesperinas M 2015 Optical torque: electromagnetic spin and orbital-angular-momentum conservation laws and their significance *Phys. Rev.* A **92** 043843
[260] Liu N, Weiss T, Mesch M, Langguth L, Eigenthaler U, Hirscher M, Sönnichsen C and Giessen H 2010 Planar metamaterial analogue for electromagnetically induced transparency for plasmonic sensing *Nano Lett.* **10** 1103–7
[261] Zhao Q, Zhou J, Zhang F and Lippens D 2009 Mie resonance-based dielectric metamaterials *Mater. Today* **12** 60–9
[262] Evlyukhin A B, Reinhardt C, Seidel A, Luk'yanchuk B S and Chichkov B N 2010 Optical response features of Si-nanoparticle arrays *Phys. Rev.* B **82** 045404
[263] Kuznetsov A I, Miroshnichenko A E, Hsing Fu Y, Zhang J and Luk'yanchuk B 2012 Magnetic light *Sci. Rep.* **2** 492
[264] Miroshnichenko A E, Evlyukhin A B, Feng Yu Y, Bakker R M, Chipouline A, Kuznetsov A I, Luk'yanchuk B,

Chichkov B N and Kivshar Y S 2015 Nonradiating anapole modes in dielectric nanoparticles *Nat. Commun.* **6** 8069
[265] Decker M, Staude I, Falkner M, Dominguez J, Neshev D N, Brener I, Pertsch T and Kivshar Y S 2015 High-efficiency dielectric Huygens' surfaces *Adv. Opt. Mater.* **3** 813–20
[266] Kuznetsov A I, Miroshnichenko A E, Brongersma M L, Kivshar Y S and Luk'yanchuk B 2016 Optically resonant dielectric nanostructures *Science* **354** aag2472
[267] Chen H-T, Taylor A J and Yu N 2016 A review of metasurfaces: physics and applications *Rep. Prog. Phys.* **79** 076401
[268] Dubovik V M and Tugushev V V 1990 Toroid moments in electrodynamics and solid-state physics *Phys. Rep.* **187** 145–202
[269] Radescu E E and Vaman G 2002 Exact calculation of the angular momentum loss, recoil force and radiation intensity for an arbitrary source in terms of electric, magnetic and toroid multipoles *Phys. Rev.* E **65** 046609
[270] Zel'dovich I B 1957 Electromagnetic interaction with parity violation *J. Exptl. Theoret. Phys. (U.S.S.R.)* **33** 1531–3
[271] Marinov K, Boardman A D, Fedotov V A and Zheludev N 2007 Toroidal metamaterial *New J. Phys.* **9** 324–324
[272] Ögüt B, Talebi N, Vogelgesang R, Sigle W and van Aken P A 2012 Toroidal plasmonic eigenmodes in oligomer nanocavities for the visible *Nano Lett.* **12** 5239–44
[273] Jiaqi Li, Zhang Y, Jin R, Wang Q, Chen Q and Dong Z 2014 Excitation of plasmon toroidal mode at optical frequencies by angle-resolved reflection *Opt. Lett.* **39** 6683
[274] Papasimakis N, Fedotov V A, Savinov V, Raybould T A and Zheludev N I 2016 Electromagnetic toroidal excitations in matter and free space *Nat. Mater.* **15** 263–71
[275] Talebi N, Guo S and van Aken P A 2018 Theory and applications of toroidal moments in electrodynamics: their emergence, characteristics and technological relevance *Nanophotonics* **7** 93–110
[276] Savinov V, Papasimakis N, Tsai D P and Zheludev N I 2019 Optical anapoles *Commun. Phys.* **2** 69
[277] Evlyukhin A B, Fischer T, Reinhardt C and Chichkov B N 2016 Optical theorem and multipole scattering of light by arbitrarily shaped nanoparticles *Phys. Rev.* B **94** 205434
[278] Raybould T, Fedotov V A, Papasimakis N, Youngs I and Zheludev N I 2017 Exciting dynamic anapoles with electromagnetic doughnut pulses *Appl. Phys. Lett.* **111** 081104
[279] Yang Y and Bozhevolnyi S I 2019 Nonradiating anapole states in nanophotonics: from fundamentals to applications *Nanotechnology* **30** 204001
[280] Fedotov V A, Rogacheva A V, Savinov V, Tsai D P and Zheludev N I 2013 Resonant transparency and non-trivial non-radiating excitations in toroidal metamaterials *Sci. Rep.* **3** 2967
[281] Kaelberer T, Fedotov V A, Papasimakis N, Tsai D P and Zheludev N I 2010 Toroidal dipolar response in a metamaterial *Science* **330** 1510–2
[282] Jackson J D 1998 *Classical Electrodynamics* 3rd edn (New York: Wiley)
[283] Zangwill A 2013 *Modern Electrodynamics* (Cambridge: Cambridge University Press)
[284] Ye Q and Lin H 2017 On deriving the Maxwell stress tensor method for calculating the optical force and torque on an object in harmonic electromagnetic fields *Eur. J. Phys.* **38** 045202
[285] Nieminen T A, du Preez-Wilkinson N, Stilgoe A B, Loke V L Y, Bui A A M and Rubinsztein-Dunlop H 2014 Optical tweezers: theory and modelling *J. Quant. Spectrosc. Radiat. Transf.* **146** 59–80
[286] Ashkin A, Dziedzic J M, Bjorkholm J E and Chu S 1986 Observation of a single-beam gradient force optical trap for dielectric particles *Opt. Lett.* **11** 288
[287] Lebedew P 1901 Untersuchungen über die Druckkräfte des Lichtes *Ann. Phys., Lpz.* **311** 433–58
[288] Nichols E F and Hull G F 1901 A preliminary communication on the pressure of heat and light radiation *Phys. Rev. Ser. I* **13** 307–20
[289] Ashkin A 1970 Acceleration and trapping of particles by radiation pressure *Phys. Rev. Lett.* **24** 156–9
[290] Novotny L, Bian R X and Xie X S 1997 Theory of nanometric optical tweezers *Phys. Rev. Lett.* **79** 645–8
[291] Arias-González J R and Nieto-Vesperinas M 2003 Optical forces on small particles: attractive and repulsive nature and plasmon-resonance conditions *J. Opt. Soc. Am.* A **20** 1201
[292] Nieto-Vesperinas M, Chaumet P C and Rahmani A 2004 Near-field photonic forces *Phil. Trans. R. Soc. London* A **362** 719–37
[293] Liu L, Kheifets S, Ginis V, Di Donato A and Capasso F 2017 Elliptical orbits of microspheres in an evanescent field *Proc. Natl Acad. Sci.* **114** 11087–91
[294] Volpe G, Quidant R, Badenes G and Petrov D 2006 Surface plasmon radiation forces *Phys. Rev. Lett.* **96** 238101
[295] Righini M, Zelenina A S, Girard C and Quidant R 2007 Parallel and selective trapping in a patterned plasmonic landscape *Nat. Phys.* **3** 477–80
[296] Grigorenko A N, Roberts N W, Dickinson M R and Zhang Y 2008 Nanometric optical tweezers based on nanostructured substrates *Nat. Photon.* **2** 365–70
[297] Quidant R and Girard C 2008 Surface-plasmon-based optical manipulation *Laser Photonics Rev.* **2** 47–57
[298] Tong L, Miljkovicć V D and Käll M 2010 Alignment, rotation and spinning of single plasmonic nanoparticles and nanowires using polarization dependent optical forces *Nano Lett.* **10** 268–73
[299] Maragò O M, Jones P H, Gucciardi P G, Volpe G and Ferrari A C 2013 Optical trapping and manipulation of nanostructures *Nat. Nanotechnol.* **8** 807–19
[300] Lehmuskero A, Johansson P, Rubinsztein-Dunlop H, Tong L and Käll M 2015 Laser trapping of colloidal metal nanoparticles *ACS Nano* **9** 3453–69
[301] Link S, Wang Z L and El-Sayed M A 2000 How does a gold nanorod melt? *J. Phys. Chem.* B **104** 7867–70
[302] Govorov A O and Richardson H H 2007 Generating heat with metal nanoparticles *Nano Today* **2** 30–8
[303] Baffou G, Quidant R and García de Abajo F J 2010 Nanoscale control of optical heating in complex plasmonic systems *ACS Nano* **4** 709–16
[304] Baffou G and Quidant R 2012 Thermo-plasmonics: using metallic nanostructures as nano-sources of heat *Laser Photonics Rev.* **7** 171–87
[305] Cole J R, Mirin N A, Knight M W, Goodrich G P and Halas N J 2009 Photothermal efficiencies of nanoshells and nanorods for clinical therapeutic applications *J. Phys. Chem.* C **113** 12090–4
[306] Jain P K, Huang X, El-Sayed I H and El-Sayed M A 2008 Noble metals on the nanoscale: optical and photothermal properties and some applications in imaging, sensing, biology and medicine *Acc. Chem. Res.* **41** 1578–86
[307] Kim M, Lee J-H and Nam J-M 2019 Plasmonic photothermal nanoparticles for biomedical applications *Adv. Sci.* **6** 1900471
[308] Govorov A O, Zhang W, Skeini T, Richardson H, Lee J and Kotov N A 2006 Gold nanoparticle ensembles as heaters and actuators: melting and collective plasmon resonances *Nanoscale Res. Lett.* **1** 84–90

[309] Baffou G, Berto P, Bermúdez Ureña E, Quidant R, Monneret S, Polleux J and Rigneault H 2013 Photoinduced heating of nanoparticle arrays *ACS Nano* **7** 6478–88
[310] Wang J, Yu K, Yang Y, Hartland G V, Sader J E and Wang G P 2019 Strong vibrational coupling in room temperature plasmonic resonators *Nat. Commun.* **10** 1527
[311] Devkota T, Yu K and Hartland G V 2019 Mass loading effects in the acoustic vibrations of gold nanoplates *Nanoscale* **11** 16208–13
[312] Hartland G V 2011 Optical studies of dynamics in noble metal nanostructures *Chem. Rev.* **111** 3858–87
[313] Marinica D C, Kazansky A K, Nordlander P, Aizpurua J and Borisov A G 2012 Quantum plasmonics: nonlinear effects in the field enhancement of a plasmonic nanoparticle dimer *Nano Lett.* **12** 1333–9
[314] Zhu W, Esteban R, Borisov A G, Baumberg J J, Nordlander P, Lezec H J, Aizpurua J and Crozier K B 2016 Quantum mechanical effects in plasmonic structures with subnanometre gaps *Nat. Commun.* **7** 11495
[315] Schmidt M K, Esteban R, González-Tudela A, Giedke G and Aizpurua J 2016 Quantum mechanical description of raman scattering from molecules in plasmonic cavities *ACS Nano* **10** 6291–8
[316] Esteban R, Borisov A G, Nordlander P and Aizpurua J 2012 Bridging quantum and classical plasmonics with a quantum-corrected model *Nat. Commun.* **3** 825
[317] Moreau A, Ciracì C and Smith D R 2013 Impact of nonlocal response on metallodielectric multilayers and optical patch antennascharma *Phys. Rev.* B **87** 045401
[318] Luo Y, Fernandez-Dominguez A I, Wiener A, Maier S A and Pendry J B 2013 Surface plasmons and nonlocality: a simple model *Phys. Rev. Lett.* **111** 093901
[319] Akimov A V, Mukherjee A, Yu C L, Chang D E, Zibrov A S, Hemmer P R, Park H and Lukin M D 2007 Generation of single optical plasmons in metallic nanowires coupled to quantum dots *Nature* **450** 402–6
[320] Kolesov R, Grotz B, Balasubramanian G, Stöhr R J, Nicolet A A L, Hemmer P R, Jelezko F and Wrachtrup J 2009 Wave-particle duality of single surface plasmon-polaritons *Nat. Phys.* **5** 470–4
[321] Kress S J P *et al* 2015 Wedge waveguides and resonators for quantum plasmonics *Nano Lett.* **15** 6267–75
[322] Marquier F, Sauvan C and Greffet J-J 2017 Revisiting quantum optics with surface plasmons and plasmonic resonators *ACS Photon.* **4** 2091–101
[323] Parzefall M, Szabó Á, Taniguchi T, Watanabe K, Luisier M and Novotny L 2019 Light from van der Waals quantum tunneling devices *Nat. Commun.* **10** 292
[324] Altewischer E, van Exter M P and Woerdman J P 2002 Plasmon-assisted transmission of entangled photons *Nature* **418** 304–6
[325] Tame M S, McEnery K R, Özdemir Ş K, Lee J, Maier S A and Kim M S 2013 Quantum plasmonics *Nat. Phys.* **9** 329–40
[326] Dowran M, Kumar A, Lawrie B J, Pooser R C and Marino A M 2018 Quantum-enhanced plasmonic sensing *Optica* **5** 628
[327] Cox J D, Silveiro Ivan and García de Abajo F J 2016 Quantum effects in the nonlinear response of graphene plasmons *ACS Nano* **10** 1995–2003
[328] Lee C, Dieleman F, Lee J, Rockstuhl C, Maier S A and Tame M 2016 Quantum plasmonic sensing: beyond the shot-noise and diffraction limit *ACS Photonics* **3** 992–9
[329] Boyd R 2008 *Nonlinear Optics* 3rd edn (New York: Academic)
[330] Liebsch A and Schaich W L 1989 Second-harmonic generation at simple metal surfaces *Phys. Rev.* B **40** 5401–10
[331] Wang F X, Rodríguez F J, Albers W M, Ahorinta R, Sipe J E and Kauranen M 2009 Surface and bulk contributions to the second-order nonlinear optical response of a gold film *Phys. Rev.* B **80** 233402
[332] Bouhelier A, Beversluis M, Hartschuh A and Novotny L 2003 Near-field second-harmonic generation induced by local field enhancement *Phys. Rev. Lett.* **90** 013903
[333] Verhagen E, Kuipers L and Polman A 2007 Enhanced nonlinear optical effects with a tapered plasmonic waveguide *Nano Lett.* **7** 334–7
[334] Palomba S, Danckwerts M and Novotny L 2009 Nonlinear plasmonics with gold nanoparticle antennas *J. Opt. A: Pure Appl. Opt.* **11** 114030
[335] Hentschel M, Utikal T, Giessen H and Lippitz M 2012 Quantitative modeling of the third harmonic emission spectrum of plasmonic nanoantennas *Nano Lett.* **12** 3778–82
[336] Bernasconi G D, Butet J and Martin O J F 2018 Dynamics of second-harmonic generation in a plasmonic silver nanorod *ACS Photonics* **5** 3246–54
[337] Autere A, Jussila H, Dai Y, Wang Y, Lipsanen H and Sun Z 2018 Nonlinear optics with 2D layered materials *Adv. Mater.* **30** 1705963
[338] Cox J D and García de Abajo F J 2019 Nonlinear graphene nanoplasmonics *Acc. Chem. Res.* **52** 2536–47
[339] Genevet P, Tetienne J-P, Gatzogiannis E, Blanchard R, Kats M A, Scully M O and Capasso F 2010 Large enhancement of nonlinear optical phenomena by plasmonic nanocavity gratings *Nano Lett.* **10** 4880–3
[340] Chen S *et al* 2016 Giant nonlinear optical activity of achiral origin in planar metasurfaces with quadratic and cubic nonlinearities *Adv. Mater.* **28** 2992–9
[341] Kauranen M and Zayats A V 2012 Nonlinear plasmonics *Nat. Photon.* **6** 737–48
[342] Butet J, Brevet P-F and Martin O J F 2015 Optical second harmonic generation in plasmonic nanostructures: from fundamental principles to advanced applications *ACS Nano* **9** 10545–62
[343] Mesch M, Metzger B, Hentschel M and Giessen H 2016 Nonlinear plasmonic Sensing *Nano Lett.* **16** 3155–9
[344] Lapine M, Shadrivov I V and Kivshar Y S 2014 *Colloqium*: nonlinear metamaterials *Rev. Mod. Phys.* **86** 1093–123
[345] Krasnok A, Tymchenko M and Alù A 2018 Nonlinear metasurfaces: a paradigm shift in nonlinear optics *Mater. Today* **21** 8–21
[346] Rahimi E and Gordon R 2018 Nonlinear plasmonic metasurfaces *Adv. Opt. Mater.* **6** 1800274
[347] Czaplicki R *et al* 2018 Less is more: enhancement of second-harmonic generation from metasurfaces by reduced nanoparticle density *Nano Lett.* **18** 7709–14
[348] Kadic M, Bückmann T, Schittny R and Wegener M 2013 Metamaterials beyond electromagnetism *Rep. Prog. Phys.* **76** 126501
[349] Leonhardt U 2006 Optical conformal mapping *Science* **312** 1777–80
[350] Schurig D, Mock J J, Justice B J, Cummer S A, Pendry J B, Starr A F and Smith D R 2006 Metamaterial electromagnetic cloak at microwave frequencies *Science* **314** 977–80
[351] Shalaev V M 2008 Transforming light *Science* **322** 384–6
[352] Ziolkowski R W 2004 Propagation in and scattering from a matched metamaterial having a zero index of refraction *Phys. Rev.* E **70** 046608
[353] Silveirinha M and Engheta N 2006 Tunneling of electromagnetic energy through subwavelength channels

and bends using ε-near-zero materials *Phys. Rev. Lett.* **97** 157403
[354] Poddubny A, Iorsh I, Belov P and Kivshar Y 2013 Hyperbolic metamaterials *Nat. Photon.* **7** 948–57
[355] Ferrari L, Wu C, Lepage D, Zhang X and Liu Z 2015 Hyperbolic metamaterials and their applications *Prog. Quantum Electron.* **40** 1–40
[356] Maxwell Garnett J C 1904 XII. Colours in metal glasses and in metallic films *Phil. Trans. R. Soc. London* A **203** 385–420
[357] Bruggeman D A G 1935 Berechnung verschiedener physikalischer Konstanten von heterogenen Substanzen. I. Dielektrizitätskonstanten und Leitfähigkeiten der Mischkörper aus isotropen Substanzen *Ann. Phys. Lpz.* **416** 636–64
[358] Rytov S M 1956 Electromagnetic properties of a finely stratified medium *JETP* **2** 466
[359] Newman W D, Cortes C L, Afshar A, Cadien K, Meldrum A, Fedosejevs R and Jacob Z 2018 Observation of long-range dipole-dipole interactions in hyperbolic metamaterials *Sci. Adv.* **4** eaar5278
[360] Guo Y, Cortes C L, Molesky S and Jacob Z 2012 Broadband super-Planckian thermal emission from hyperbolic metamaterials *Appl. Phys. Lett.* **101** 131106
[361] Dyachenko P N, Molesky S, Yu Petrov A, Störmer M, Krekeler T, Lang S, Ritter M, Jacob Z and Eich M 2016 Controlling thermal emission with refractory epsilon-near-zero metamaterials via topological transitions *Nat. Commun.* **7** 11809
[362] Shekhar P and Jacob Z 2014 Strong coupling in hyperbolic metamaterials *Phys. Rev.* B **90** 045313
[363] Jacob Z, Smolyaninov I I and Narimanov E E 2012 Broadband Purcell effect: radiative decay engineering with metamaterials *Appl. Phys. Lett.* **100** 181105
[364] Galfsky T, Krishnamoorthy H N S, Newman W, Narimanov E E, Jacob Z and Menon V M 2015 Active hyperbolic metamaterials: enhanced spontaneous emission and light extraction *Optica* **2** 62
[365] Chen J *et al* 2012 Optical nano-imaging of gate-tunable graphene plasmons *Nature* **487** 77–81
[366] Khorasaninejad M, Chen W T, Zhu A Y, Oh J, Devlin R C, Rousso D and Capasso F 2016 Multispectral chiral imaging with a metalens *Nano Lett.* **16** 4595–600
[367] Karimi E, Schulz S A, De Leon I, Qassim H, Upham J and Boyd R W 2014 Generating optical orbital angular momentum at visible wavelengths using a plasmonic metasurface *Light: Sci. Appl.* **3** e167
[368] Bouchard Fedéric, De Leon I, Schulz S A, Upham J, Karimi E and Boyd R W 2014 Optical spin-to-orbital angular momentum conversion in ultra-thin metasurfaces with arbitrary topological charges *Appl. Phys. Lett.* **105** 101905
[369] Jin J, Luo J, Zhang X, Gao H, Li X, Mingbo P, Gao P, Zhao Z and Luo X 2016 Generation and detection of orbital angular momentum via metasurface *Sci. Rep.* **6** 24286
[370] Ren H *et al* 2019 Metasurface orbital angular momentum holography *Nat. Commun.* **10** 2986
[371] Ni X, Kildishev A V and Shalaev V M 2013 Metasurface holograms for visible light *Nat. Commun.* **4** 2807
[372] Deng Z-L and Li G 2017 Metasurface optical holography *Mater. Today Phys.* **3** 16–32
[373] Zhang X *et al* 2019 Direct polarization measurement using a multiplexed Pancharatnam–Berry metahologram *Optica* **6** 1190
[374] High A A, Devlin R C, Dibos A, Polking M, Wild D S, Perczel J, de Leon N P, Lukin M D and Park H 2015 Visible-frequency hyperbolic metasurface *Nature* **522** 192–6
[375] Li P *et al* 2018 Infrared hyperbolic metasurface based on nanostructured van der Waals materials *Science* **359** 892–6
[376] Barnes W L 1999 Electromagnetic crystals for surface plasmon polaritons and the extraction of light from emissive devices *J. Lightwave Technol.* **17** 2170–82
[377] Defrance J *et al* 2016 Moosh: A numerical swiss army knife for the optics of multilayers in octave/matlab *J. Open Res. Software* **4** e13
[378] Hasan M Z and Kane C L 2010 *Colloqium*: topological insulators *Rev. Mod. Phys.* **82** 3045–67
[379] Kane C L and Mele E J 2005 Quantum spin Hall effect in graphene *Phys. Rev. Lett.* **95** 226801
[380] Lu L, Joannopoulos J D and Soljačić M 2014 Topological photonics *Nat. Photon.* **8** 821–9
[381] Rider M S, Palmer S J, Pocock S R, Xiao X, Huidobro P A and Giannini V 2019 A perspective on topological nanophotonics: current status and future challenges *J. Appl. Phys.* **125** 120901
[382] Ozawa T *et al* 2019 Topological photonics *Rev. Mod. Phys.* **91** 015006
[383] Bliokh K Y, Bekshaev A Y and Nori F 2014 Extraordinary momentum and spin in evanescent waves *Nat. Commun.* **5** 3300
[384] Bliokh K Y and Rodríguez-Fortuño F J, Nori F, and Zayats A V 2015 Spin–orbit interactions of light. *Nat. Photon.* **9** 796–808
[385] Weick G, Woollacott C, Barnes W L, Hess O and Mariani E 2013 Dirac-like plasmons in honeycomb lattices of metallic nanoparticles *Phys. Rev. Lett.* **110** 106801
[386] Lu J, Qiu C, Xu S, Ye Y, Ke M and Liu Z 2014 Dirac cones in two-dimensional artificial crystals for classical waves *Phys. Rev.* B **89** 134302
[387] Markel V A 1993 Coupled-dipole approach to scattering of light from a one-dimensional periodic dipole structure *J. Mod. Opt.* **40** 2281–91
[388] Zou S, Janel N and Schatz G C 2004 Silver nanoparticle array structures that produce remarkably narrow plasmon lineshapes *J. Chem. Phys.* **120** 10871–5
[389] Auguié B and Barnes W L 2008 Collective resonances in gold nanoparticle arrays *Phys. Rev. Lett.* **101** 143902
[390] Humphrey A D and Barnes W L 2014 Plasmonic surface lattice resonances on arrays of different lattice symmetry *Phys. Rev.* B **90** 075404
[391] Humphrey A D, Meinzer N, Starkey T A and Barnes W L 2016 Surface lattice resonances in plasmonic arrays of asymmetric disc dimers *ACS Photonics* **3** 634–9
[392] Wang W, Ramezani M, Väkeväinen A I, Törmä P, Gómez Rivas J and Odom T W 2018 The rich photonic world of plasmonic nanoparticle arrays *Mater. Today* **21** 303–14
[393] Li R, Bourgeois M R, Cherqui C, Guan J, Wang D, Hu J, Schaller R D, Schatz G C and Odom T W 2019 Hierarchical hybridization in plasmonic honeycomb lattices *Nano Lett.* **19** 6435–41
[394] Kuznetsov A I *et al* 2011 Laser fabrication of large-scale nanoparticle arrays for sensing applications *ACS Nano* **5** 4843–9
[395] Moilanen A J, Hakala T K and Törmä P 2017 Active control of surface plasmon–emitter strong coupling *ACS Photon.* **5** 54–64
[396] Hakala T K, Rekola H T, Väkeväinen A I, Martikainen J-P, Nečada M, Moilanen A J and Törmä P 2017 Lasing in dark and bright modes of a finite-sized plasmonic lattice *Nat. Commun.* **8** 13687
[397] Wang N, Zeisberger M, Huebner U, Giannini V and Schmidt M A 2019 Symmetry-breaking induced magnetic Fano resonances in densely packed arrays of symmetric nanotrimers *Sci. Rep.* **9** 2873

[398] Wang D, Bourgeois M R, Guan J, Fumani A K, Schatz G C and Odom T W 2020 Lasing from finite plasmonic nanoparticle lattices *ACS Photonics* **7** 630–6
[399] Pocock S R, Xiao X, Huidobro P A and Giannini V 2018 Topological plasmonic chain with retardation and radiative effects *ACS* Photonics **5** 2271–9
[400] Proctor M, Craster R V, Maier S A, Giannini V and Huidobro P A 2019 Exciting pseudospin-dependent edge states in plasmonic metasurfaces *ACS Photonics* **6** 2985–95
[401] Jin D, Christensen T, Soljačić M, Fang N X, Lu L and Zhang X 2017 Infrared topological plasmons in graphene *Phys. Rev. Lett.* **118** 245301
[402] Pan D, Yu R, Xu H and García de Abajo F J 2017 Topologically protected Dirac plasmons in a graphene superlattice *Nat. Commun.* **8** 1243
[403] Chervy T, Azzini S, Lorchat E, Wang S, Gorodetski Y, Hutchison J A, Berciaud S, Ebbesen T W and Genet C 2018 Room temperature chiral coupling of valley excitons with spin-momentum locked surface plasmons *ACS Photon.* **5** 1281–7
[404] Wang Li, Zhang R-Y, Xiao M, Han D, Chan C T and Wen W 2016 The existence of topological edge states in honeycomb plasmonic lattices *New J. Phys.* **18** 103029
[405] Proctor M, Huidobro P A, Maier S A, Craster R V and Makwana M P 2020 Manipulating topological valley modes in plasmonic metasurfaces *Nanophotonics* **9** 657–65
[406] Smith S J and Purcell E M 1953 Visible light from localized surface charges moving across a grating *Phys. Rev.* **92** 1069
[407] Haeberlé O, Rullhusen P, Salomé J-M and Maene N 1997 Smith–Purcell radiation from electrons moving parallel to a gratingat oblique incidence to the rulings *Phys. Rev.* E **55** 4675–83
[408] García de Abajo F J 2000 Smith–Purcell radiation emission in aligned nanoparticles *Phys. Rev.* E **61** 5743–52
[409] Yamamoto N, Araya K and García de Abajo F J 2001 Photon emission from silver particles induced by a high-energy electron beam *Phys. Rev.* B **64** 205419
[410] Talebi N 2014 A directional, ultrafast and integrated few-photon source utilizing the interaction of electron beams and plasmonic nanoantennas *New J. Phys.* **16** 053021
[411] Kaminer I *et al* 2017 Spectrally and spatially resolved Smith–Purcell radiation in plasmonic crystals with short-range disorder *Phys. Rev.* **7** 011003
[412] García de Abajo F J 2010 Optical excitations in electron microscopy *Rev. Mod. Phys.* **82** 209–75
[413] Polman A, Kociak M, and García de Abajo F J 2019 Electron-beam spectroscopy for nanophotonics *Nat. Mater.* **18** 1158–71
[414] Ropers C, Neacsu C C, Elsaesser T, Albrecht M, Raschke M B and Lienau C 2007 Grating-coupling of surface plasmons onto metallic tips: a nanoconfined light source *Nano Lett.* **7** 2784–8
[415] Ropers C, Elsaesser T, Cerullo G, Zavelani-Rossi M and Lienau C 2007 Ultrafast optical excitations of metallic nanostructures: from light confinement to a novel electron source *New J. Phys.* **9** 397
[416] Ropers C, Solli D R, Schulz C P, Lienau C and Elsaesser T 2007 Localized multiphoton emission of femtosecond electron pulses from metal nanotips *Phys. Rev. Lett.* **98** 043907
[417] Hommelhoff P, Sortais Y, Aghajani-Talesh A and Kasevich M A 2006 Field emission tip as a nanometer source of free electron femtosecond pulses *Phys. Rev. Lett.* **96** 077401
[418] Echternkamp K E, Feist A, Schäfer S and Ropers C 2016 Ramsey-type phase control of free-electron beams *Nat. Phys.* **12** 1000–4
[419] Priebe K E, Rathje C, Yalunin S V, Hohage T, Feist A, Schäfer S and Ropers C 2017 Attosecond electron pulse trains and quantum state reconstruction in ultrafast transmission electron microscopy *Nat. Photon.* **11** 793–7
[420] Kurtz F, Ropers C and Herink G 2019 Resonant excitation and all-optical switching of femtosecond soliton molecules *Nat. Photon.* **14** 9–13
[421] Lambe J and McCarthy S L 1976 Light emission from inelastic electron tunneling *Phys. Rev. Lett.* **37** 923–5
[422] Uskov A V, Khurgin J B, Protsenko I E, Smetanin I V and Bouhelier A 2016 Excitation of plasmonic nanoantennas by nonresonant and resonant electron tunnelling *Nanoscale* **8** 14573–9
[423] Haffner C *et al* 2018 Low-loss plasmon-assisted electro-optic modulator *Nature* **556** 483–6
[424] Flöry N, Ma P, Salamin Y, Emboras A, Taniguchi T, Watanabe K, Leuthold J and Novotny L 2020 Waveguide-integrated van der Waals heterostructure photodetector at telecom wavelengths with high speed and high responsivity *Nat. Nanotechnol.* **15** 118–24
[425] Du W, Wang T, Chu H-S and Nijhuis C A 2017 Highly efficient on-chip direct electronic–plasmonic transducers *Nat. Photon.* **11** 623–7
[426] Parzefall M and Novotny L 2018 Light at the end of the tunnel *ACS Photon.* **5** 4195–202
[427] Makarenko K S, Xuan Hoang T, Duffin T J, Radulescu A, Kalathingal V, Lezec H K, Chu H-S and Nijhuis C A 2020 Efficient surface plasmon polariton excitation and control over outcoupling mechanisms in metal–insulator–metal tunneling junctions *Advanced Science* **7** 1900291